University of Calabria

Faculty of Engineering

Department of Mechanical Engineering

Investigating The Interaction Between The Cardiovascular System And An Axial Flow Ventricular Assist Device: Mathematical Model And An Acute Animal Study

Coordinator

Prof. Maria Laura Luchi

Candidate

Francesco Moscato

Supervisors

Prof. Guido A. Danieli

Prof. Heinrich Schima

Dissertation submitted to obtain the degree of Doctor in Mechanical Engineering (ING-IND 34)

Academic Year 2006/2007

Dissertation submitted to obtain the degree of Doctor in Mechanical Engineering (ING-IND 34, Industrial Bioengineering) – Academic Year 2006/2007 – XX cycle

Department of Mechanical Engineering
University of Calabria
Via Ponte P. Bucci, Cubo 44/C
97036 Arcavacata di Rende (CS)
ITALY

Correspondence to:
francesco.moscato@unical.it
moscato_francesco@libero.it

To my family.

To everybody and
to every emotion, passion and experience
that you can only find and read
in the white space
between the lines of this manuscript.

Table of Contents

Chapter 3 59

A hydrodynamic numerical model of the MicroMed-DeBakey VAD® : software and hardware tools used for identification.

Chapter 4 101

In-vivo investigation of VAD-cardiovascular system interaction: left ventricular pressure volume loop analysis during continuous cardiac assist in acute animal trials.

Symbols used in text

a, b = fluid resitance parameters for the VAD model

Cap = arterial pulmonary compliance

Cas = arterial systemic compliance

Cas* = reduced arterial systemic compliance

Ccp = characteristic pulmonary compliance

Ccs = characteristic systemic compliance

Cvp = venous pulmonary compliance

Cvs = venous systemic compliance

dP/dt_{max} = peak of ventricular pressure derivative

E(t) = time-varying elastance

E_a = arterial elastance

E_{max} = maximum elastance

E_{min} = minimum elastance

F_c = Coulomb friction force

$F_{iso}(t)$ = ventricular/atrial elastance normalized with respect to T and E_{max}.

F_s = static friction force

F_v = viscous friction force

$\hat{G}_N\left(e^{j\omega}\right)$ = Empirical Transfer Function Estimate

H(t) = axial VAD pump head

i = coil current

k = spring constant

Kf = force/speed coefficient

kSAT = spring stiffening coefficient

L = inertance parameter for the VAD model

Lcp = characteristic pulmonary inertance

Lcs = characteristic sytemic inertance

L_e = coil inductance

L_v = valve inertance

M = piston (and moving element) mass

P_0 = external ventricular/atrial pressure

P_{ao} = aortic pressure

P_{ap} = pulmonary arterial pressure

P_{as} = arterial systemic pressure

P_d = pressure at minimum ventricular volume V_d

P_{lv} = left ventricular pressure

P_{rv} = right ventricular pressure

P_{la} = left atrial pressure

P_m = φ_p parameter

P_{ra} = right atrial pressure

P_{vp} = venous pulmonary pressure

P_{vs} = venous systemic pressure

P* = pressure coordinate of the φ_a vertex

Q_{ilv} = left ventricular inflow

Q_{irv} = right ventricular inflow

Q_{olv} = left ventricular outflow

Q_{orv} = right ventricular outflow

Q_{VAD} = axial VAD pump flow

Q* = flow through the Ras* (reference flow for the VAD)

Rap = arterial pulmonary resistance

Ras = arterial systemic resistance

Ras* = reduced arterial systemic resistance

Rcp = characteristic pulmonary resistance

Rcs = characteristic sytemic resistance

Rcs* = reduced characteristic sytemic resistance

Rvp = venous pulmonary pressure

Rvs = venous systemic pressure

R_{dir} = direct valve resistance

R_{inv} = inverse valve resistance

R_i = internal ventricular resistance

R_e = coil resistance

S = piston surface

Str = piston stroke

T = heart period

U_i = voltage fed to the amplifier

U_{amp} = voltage fed by the amplifier into the coil

V_0 = ventricular/atrial volume at zero transmural pressure

V_d = minimum ventricular volume (also called dead volume)

V_{lv} = left ventricular volume

V_m = φ_p parameter

V_{rv} = right ventricular volume

Vvpo = unstretched volume of the Cvp

Vvso = unstretched volume of the Cvs

V* = volume coordinate of the φ_a vertex

x = piston position

α_ω = speed-related parmeter for the VAD model

α = φ_p parameter

β = φ_p parameter

Δv = zero velocity interval

$\varphi[V(t),t]$ = non-linear time-varying elastance

φ_a = active characteristic of the ventricular/atrial muscle

φ_p = passive characteristic of the ventricular/atrial muscle

$\hat{\kappa}_{yu}^{N}$ = coherency spectrum

$\hat{\theta}_N$ = parameter vector

Abbreviations and acronyms

AoP: Aortic Pressure
BSA: Body Surface Area
CO: Cardiac Output (CO=HR*SV)
COI: Cardiac Output Index
CVP: Central Venous Pressure
DC: Direct Current
EDP: End Diastolic Pressure
EDPVR: End Diastolic Pressure Volume Relationship
EDV: End Diastolic Volume
EDVI: End Diastolic Volume Index
EF: Ejection Fraction (EF=SV/EDV)
EKF: Extended Kalman Filter
ESP: End Systolic Pressure
ESPVR: End Systolic Pressure Volume Relationship
ESV: End Systolic Volume
ESVI: End Systolic Volume Index
ETFE: Empirical Transfer Function Estimate
EV = Extra Volume
EW: External Work
GUI: Graphic User Interface
HR: Heart Rate
LAP: Left Atrial Pressure
LVP: Left Ventricular Pressure
LV: Left Ventricle
LVM: Left Ventricular Mass
NYHA: New York Heart Association
PE: Potential Energy
PV: Pressure-Volume
PVA: Pressure Volume Area
PAP: Pulmonary Arterial Pressure
Pmc: Mean Circulatory Pressure
Pmp: Mean Pulmonary Pressure
Pms: Mean Systemic Pressure
RAP: Right Atrial Pressure
RMSE: Root Mean Square Error
RVP: Right Ventricular Pressure
RV: Right Ventricle
SV: Stroke Volume
SVI: Stroke Volume Index
SVR: Systemic Vascular Resistance
VAD: Ventricular Assist Device
%VAF: Percent Variance Accounted For

Introduction

Mechanical circulatory support is evolved substantially since its inception in the late 1960s and in 2001 it was demonstrated a 48% reduction in the risk of death in patient group treated with ventricular assist devices (VADs) compared with medically treated group. Although the majority of VADs are nowadays used as bridge to heart transplantation, permanent use and bridge to ventricular recovery represent a source of intense research and development.

Aim of this work was to investigate the interaction between an axial flow VAD and the assisted cardiovascular system, by means both of mathematical modeling and an acute animal study. This interaction is a crucial aspect in the development of mechanical circulatory support intended for long-term use.

A numerical model of the whole cardiovascular system was implemented and validated using literature data. It joins accurate single compartments (like ventricles and atria, arterial loads and venous returns, both for systemic and pulmonary circulation) and the of the overall cardiac-output regulation mechanisms.

This model was completed with a hydrodynamic numerical model of an axial flow VAD (MicroMed-DeBakey VAD$^{\circledR}$). Advanced signal processing techniques were used for the VAD characterization (stochastic spectral analysis, nonlinear recursive estimation). In order to built the necessary experimental setup for VAD identification, mathematical methods for identification and control (full-state feedback digital control) of components in a mock circuit were used.

The interaction of the VAD and the cardiovascular system during in-vivo experiments was then investigated: in particular statistical methods were applied to analyze left ventricular pressure volume loop during MicroMed-DeBakey VAD$^{\circledR}$ assistance in an acute animal study. Results from this study show that autoregulatory mechanisms play an important role in cardiac output regulation. This result brings new and original insight in the interaction between the cardiovascular system and an axial flow VAD. Therefore a new VAD control strategy, which accounts for these phenomena, must be sought.

Using the previously derived cardiovascular and VAD models, an innovative VAD control strategy was designed and tested on a numerical basis. The main point in this strategy is that neither pressure head or flow across the VAD are controlled, but the LV afterload impedance seen by the failing ventricle ejecting through the VAD. The pump is controlled so that it represents a hydraulic afterload impedance for the ejecting ventricle. That makes the device a cardiovascular system-integrated component. The interaction between the so controlled VAD and the assisted cardiovascular system was evaluated with the mathematical model.

The investigation of this interaction shows that a more physiological VAD control, like to one proposed in this work, restores normal patient perfusion and hemodynamics and, probably more important, can help ventricular recovery.

Introduzione

L'assistenza meccanica alla circolazione ha subito una sostanziale evoluzione da quando è stata introdotta alla fine degli anni sessanta. Nel 2001 uno studio ha dimostrato una riduzione del 48% del rischio di morte in pazienti trattati con sistemi di assistenza ventricolare (*ventricular assist devices*, VADs) rispetto a quelli trattati con convenzionali cure mediche. Sebbene la maggioranza dei dispositivi di assistenza ventricolare sono usati oggigiorno per supportare i pazienti fino al loro trapianto di cuore, l'uso permanente oppure quello orientato al recupero del muscolo cardiaco rappresentano un intenso campo di ricerca e sviluppo.

Obiettivo di questo lavoro è stato quello di investigare l'interazione tra un sistema di assistenza ventricolare, di tipo pompa a flusso assiale, ed il sistema cardiovascolare assistito. Tale interazione è un aspetto cruciale nello sviluppo dei dispositivi meccanici di assistenza cardiovascolare per il supporto a lungo termine, permanente od orientato al recupero. Tale studio è stato condotto per mezzo sia di modelli matematici che di uno studio *in-vivo* con impianto di VAD in animale.

Un modello numerico dell'intero sistema cardiovascolare è stato implementato nel linguaggio Matlab®-Simulink® usando dati provenienti dalla letteratura. Tale modello unisce ai singoli compartimenti accuratamente modellizzati (come i ventricoli e gli atri, i carichi arteriosi ed i ritorni venosi sia per il circolo sistemico che per quello polmonare) gli importanti meccanismi di regolazione della portata cardiaca.

Il modello del sistema cardiovascolare è stato completato con un modello numerico idrodinamico di un VAD a flusso assiale (MicroMed-DeBakey VAD®). Per la caratterizzazione e relativa modellizzazione del VAD sono state usate tecniche numeriche avanzate per l'analisi dei segnali (analisi stocastica spettrale, stima non-lineare ricorsiva). Inoltre, per poter costruire il necessario setup sperimentale per l'identificazione del VAD, sono stati usati metodi matematici per l'identificazione ed il controllo (controllo digitale in *full-state feedback*) dei componenti del banco-prova utilizzato.

L'interazione del VAD con il sistema cardiovascolare durante esperimenti *in-vivo* è stata poi investigata: in particolare sono stati applicati metodi statistici per l'analisi dei *loop* pressione-volume del ventricolo sinistro durante l'assistenza fornita dal MicroMed-DeBakey VAD® in uno studio acuto su animale. I risultati di questo studio mostrano che i meccanismi di autoregolazione del sistema cardiovascolare giocano un ruolo importante nel controllo della portata cardiaca durante l'assistenza meccanica. Tali risultati portano nuova luce nello studio dell'interazione tra il sistema cardiovascolare ed un VAD a flusso assiale. Per tali motivi è necessaria una strategia innovativa per il controllo tali VAD che tenga in considerazione questi aspetti.

Usando i modelli del sistema cardiovascolare e del VAD precedentemente sviluppati, un'innovativa strategia di controllo è stata progettata e successivamente testata su base numerica. L'aspetto principale di questa strategia è che né la prevalenza né il flusso attraverso il VAD sono controllati, bensì l'impedenza idraulica vista dal ventricolo patologico che eietta verso il sistema di assistenza ventricolare. La pompa a flusso assiale è, pertanto, controllata in maniera tale da rappresentare un carico idraulico opportunamente scelto per il ventricolo. Tale strategia rende il sistema di assistenza un componente "integrato" nel sistema cardiovascolare. L'interazione tra il VAD così controllato ed il sistema cardiovascolare assistito è stata valutata per mezzo di modelli matematici considerando i comuni indicatori clinici per determinare la salute dei pazienti.

Concludendo, lo studio dell'interazione tra il sistema cardiovascolare ed il VAD preso in esame ci mostra che una strategia di controllo per tali dispositivi di assistenza come quella presentata, che rispetta maggiormente la fisiologia del sistema assistito, ripristina la naturale perfusione e l'emodinamica del paziente e, cosa forse più importante, può favorire il recupero del ventricolo patologico.

Chapter 1

Introduction to cardiovascular physiology and mechanical circulatory assist devices.

In the first part of the chapter concepts of cardiovascular physiology will be presented: in particular notions of anatomy, heart mechanics, vascular system and cardiac output regulation are exposed. Pathologies involved in mechanical support are also described. In the second part indication and uses of mechanical circulatory assist devices are presented. Finally an overview of different ventricular assist devices and their working principles is given.

1. Physiology and Pathology of Heart and Circulation

1.1.   Anatomy of heart and circulation

The heart and blood vessels are essentially a transportation system that supplies all the cells of the body, delivering essential materials and carrying away the waste products of metabolism. The circulatory system consists of the heart, arteries, capillaries and veins, each with distinctive architecture and function.

The heart comprises two conjoined pulsatile pumps in series connection: the right and the left ventricles (Figure 1.1), one sending the blood through the lungs and the other to the rest of the body. Each ventricle is made up of a variable volume chamber, equipped with two one-way valves, one for the filling and the other for the ejection of the ventricle. Each ventricle is preceded by an atrium, which functions as a weak primer pump for the ventricle, helping to move the blood into the ventricle.
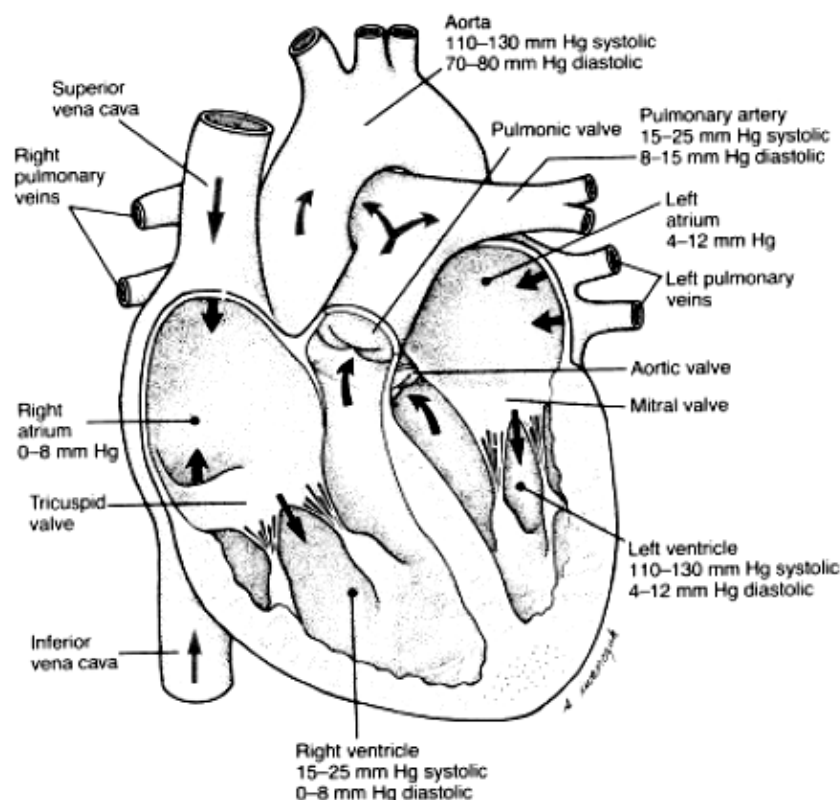
Figure 1.1 – structure of the heart; pressures inside atria and ventricles as well as at their inlet and outlet are shown (Darovic, 1995).

The two ventricles supply the main energy to the blood for its circulation into the vascular system which is a closed hydraulic loop made up of two circuits in series connection: the systemic circulation and the pulmonary circulation (Figure 1.2).

2
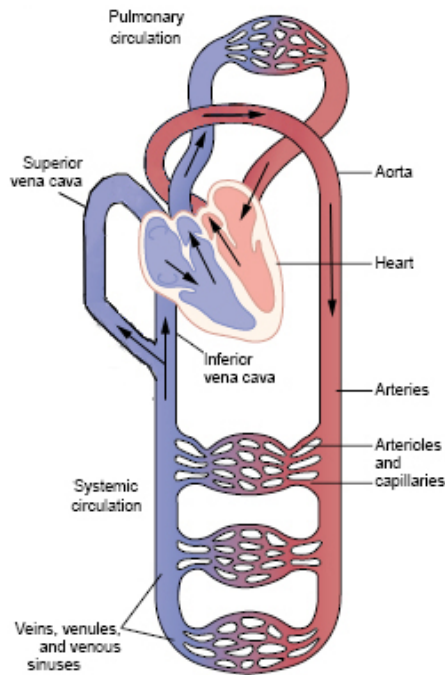
Figure 1.2 – human systemic and pulmonary circulations.

Blood ejected from the left and right ventricle enters the aorta and the main pulmonary artery, respectively, and the subsequent branching of these primary vessels is tree-like. The large arteries gradually split into muscular arteries, arterioles and capillaries. In the capillaries the blood exchanges substances with the surrounding tissues. The capillaries will eventually converge again in venules and further into veins (Figure 1.3). In general, the role of arteries is the transport of blood away from the heart, while veins transport it towards the heart. Several pathways are in parallel connection between outlets and inlets of the two ventricles and realize their hydraulic load. Every pathway contains at least one organ. At the inlet of each receiver there exists higher pressure than at its outlet.
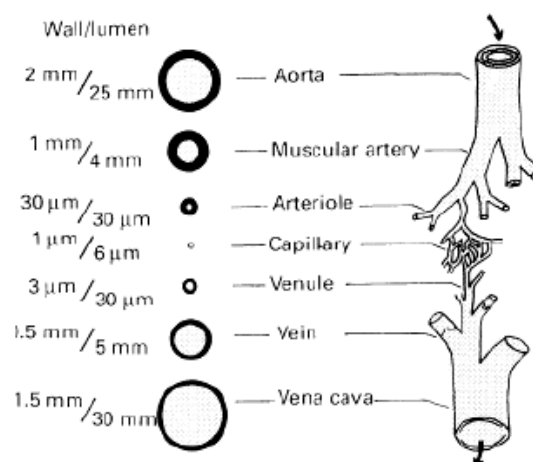
Figure 1.3 – branching of blood vessels and pathway through which blood flows (Levick, 1995).

The elastic properties of arteries differ as arterial vessels become smaller. While aorta and pulmonary artery have a certain degree of compliance (they are sometimes called *elastic* arteries), arterioles and most distal branches represent the components responsible for the regulation of the actual total vascular resistance (they are sometimes labeled *muscular* arteries).

Veins constitute a second vascular tree, beginning with venules and converging to from larger and larger trunks. The veins act as a variable volume reservoir because their innervations allow for active control of the stored volume and contain about two-thirds of the circulating blood.

1.2.   Cardiac mechanics

The mechanics of ventricular contraction and therefore the ventricle pump can be modeled using a "variable stiffness spring" element. In fact since the mid-nineteenth century, it was recognized that the tension-length relationship of skeletal muscle resembles that of a spring coil that obeys Hook's law and the stiffness of the skeletal muscle is altered by stimulation.

In the 1920s this concept was somewhat formalized and given the name "a new elastic body theory" (Hill 1922). When a resting muscle is stretched an amount of energy is actively generated that stiffens the muscle (see Figure 1.4). The contracting muscle could then be modeled as a spring that varies periodically its stiffness. In the 1960s, those biomedical engineers who were interested in simulation analyses of the dynamics of arterial pressure and flow began to model the cardiac chamber contraction by periodic changes in the myocardial elastic property. In (Suga, 1969) the concept of time-varying ventricular elastance was introduced and linked to the instantaneous pressure and volume measurements into the ventricle.
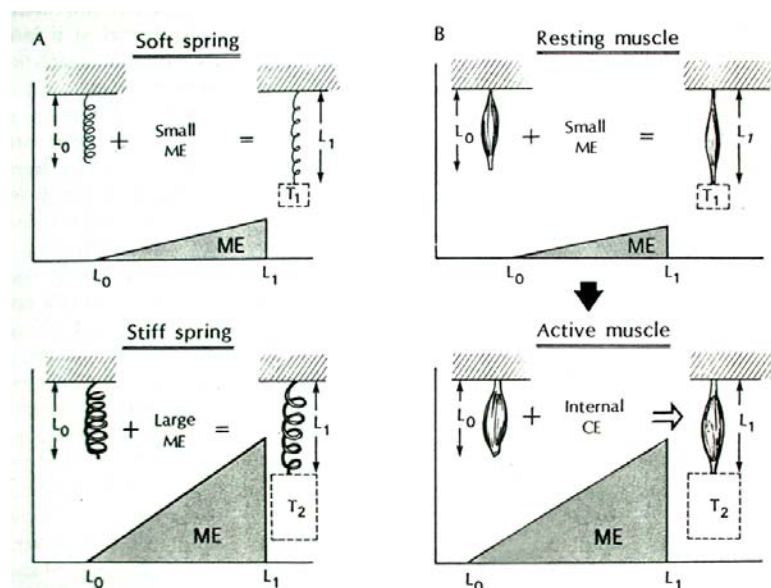
Figure 1.4 – schematic diagrams to explain elastic body theory by analogy of spring coil (A) to muscle (B) (Sagawa et al., 1988, p. 43).

A powerful tool for studying cardiac mechanics and the interactions between ventricle and circulatory system is the pressure-volume (PV) loop. Cardiac contractions can be viewed "through the window of the pressure-volume diagram" (Sagawa et al., 1988, p. 3). It is possible to link the instantaneous pressure $P_{lv}(t)$ and the instantaneous blood volume $V_{lv}(t)$ inside the ventricle by means of the following pressure-volume relationship:

$$P_{lv}(t) = P_0 + E(t) \cdot \left[V_{lv}(t) - V_0\right] \tag{1.1}$$

where P_0 is the external ventricular pressure, V_0 is the ventricular volume at zero transmural pressure, $P_{lv}(t)-P_0=0$, and $E(t)$ is the time-varying ventricular elastance.

Ventricular elastance is defined as in equation (1.2), by neglecting the term P_0. Equation (1.2) states that in one cardiac cycle the relationship between the instantaneous pressure $P_{lv}(t)$ and the instantaneous volume $V_{lv}(t)$ inside the ventricle is a time-dependent parameter, the so called the time-varying elastance $E(t)$.

$$E(t) = \frac{P_{lv}(t)}{\left[V_{lv}(t) - V_0\right]} \tag{1.2}$$

By connecting isochronous sets of instantaneous pressure-volume data points at different ventricular volumes (Sagawa et al., 1977), a family of curves whose slope rise and fall can be plotted. This results, during the cardiac cycle, in an increase and decrease of the ventricular elastance (Figure 1.5B).
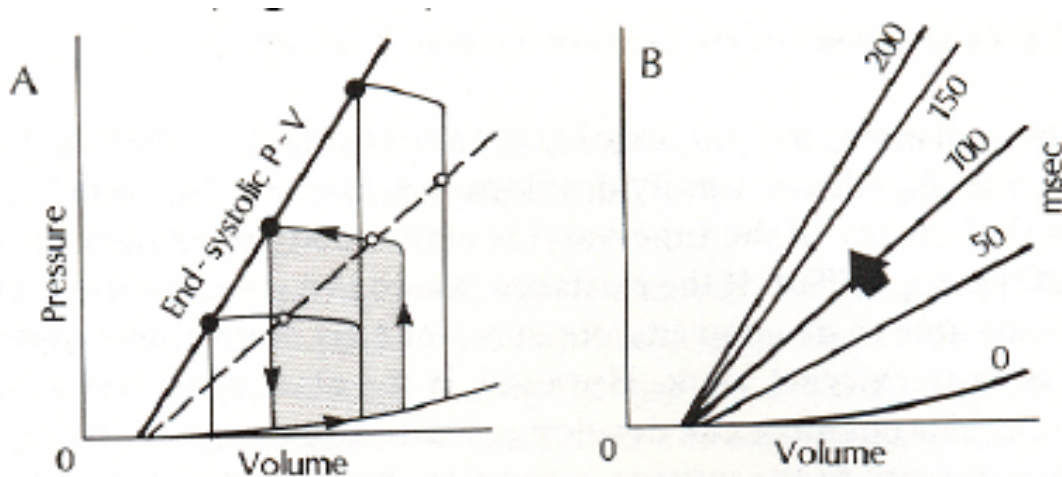
Figure 1.5 – pressure-volume relations of ventricles (Sagawa et al., 1977).

The elastance curves have a pivot point with coordinates V_0 and P_0 Equation (1.2) represents the first and simplest elastance theory formulated by Sagawa und Suga. The simplifications adopted in this model concern: the term V_0, considered constant throughout the cardiac cycle, that is, in fact, a time-varying parameter because it slightly varies during the filling

phase (Maughan et al., 1979); the absence of the y-coordinate P_0 of the pivot point, which would be slightly negative (Suga et al., 1988).

In (Suga et al., 1980) the pressure-volume relationship is completed by means of three more terms which result in extra ventricular pressure drop: the instantaneous ejection rate, $a*(dV/dt)$, the peak ejection rate, $b*(dV/dt)_{max}$, and the amount of blood ejected, $c*\int dV$. The first term is due to the visco-elastic behavior of the myocardium and gives the biggest contribution. As a consequence, the last two terms are usually neglected. This leads to the same relationship elaborated by (Campbell et al., 1982a):

$$P_{lv}(t) = P_0 + E(t) \cdot [V_{lv}(t) - V_0] - R_i \cdot Q(t) \tag{1.3}$$

with R_i representing the ventricular internal resistance, whose pressure drop occurs only during the ejection phase.

All the elastance curves $E(t)$, if normalized with respect to the peak value E_{max} and the time to peak T_{max} would reduce a single curve which has the same shape for any heart, loading conditions, contractile state, or heart rate (Sagawa et al., 1988, p. 63) (Figure 1.6)
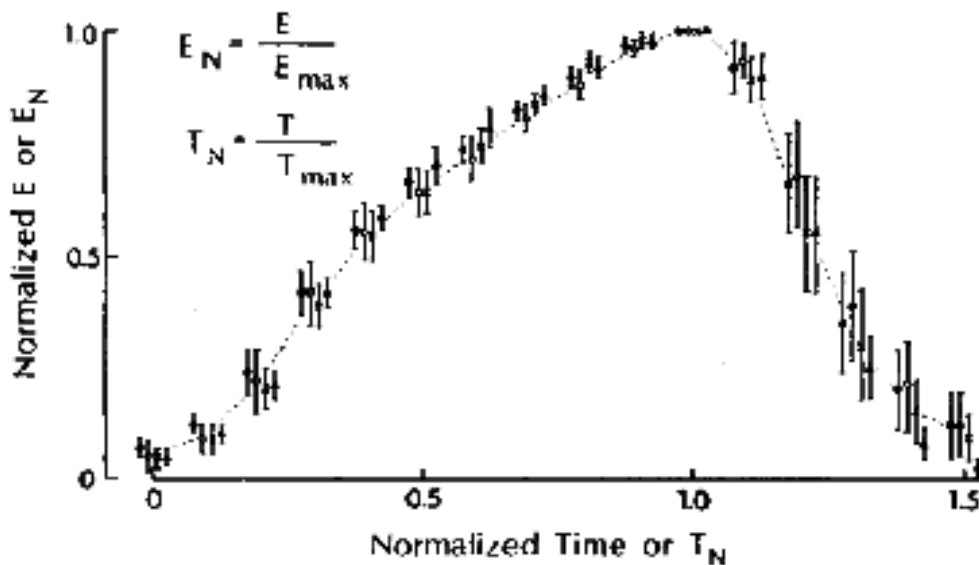
Figure 1.6 – superimposed plot of many normalized pressure-volume ratio curves, E_N, against normalized time, T_N (Sagawa et al., 1988, p. 63).

As a consequence, E_{max} and T_{max} can serve as a reliable index of ventricular contractility and are independent of ventricle pump working conditions (Suga et al., 1973).

By plotting the instantaneous left ventricular (LV) pressure versus the instantaneous LV volume the pressure-volume loop diagram in Figure 1.7a is obtained, and relating it to the Figure 1.7b, its four phases can be commented as follows.

(a)   (b)
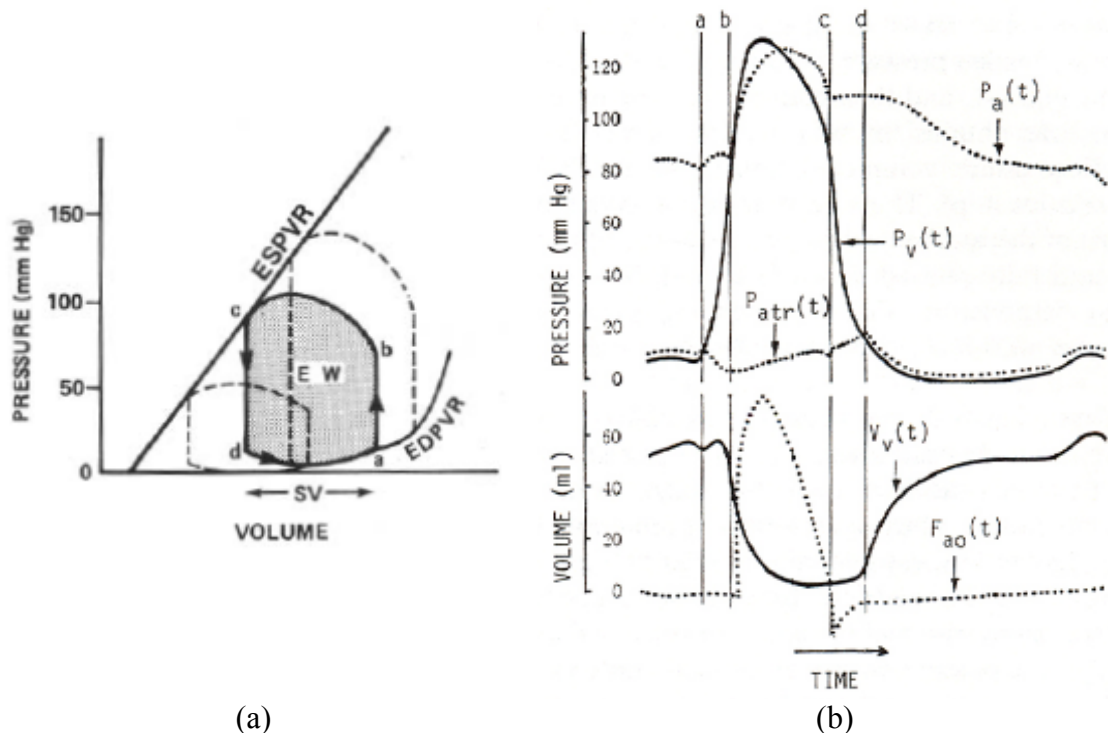
Figure 1.7 – (a) pressure-volume loop diagram of left ventricular contraction; (b) time function curves of ventricular pressure, $P_v(t)$, aortic pressure, $P_{ao}(t)$, atrial pressure, $P_{atr}(t)$, ventricular volume, $V_v(t)$, and aortic flow, $F_{ao}(t)$ (Sagawa et al., 1988, pp. 4-5).

Point *a* in Figure 1.7a indicates the ventricular cavity pressure and volume at which the ventricle begins its contraction. The volume at this point is called end diastolic volume (EDV) while the pressure is called end diastolic pressure (EDP). Point *a* represents the end of diastole and the beginning of systole, the letter being further divided in an isovolumic contraction phase and an ejection phase.

During the subsequent period, with the closing of the mitral valve (i.e. the left ventricle inlet valve), the ventricle rapidly builds up pressure without changing its volume. This isovolumic period is represented by the vertical segment of line *a-b*.

When the ventricular pressure exceeds the aortic blood pressure, the pressure difference pushes open the aortic valve (i.e. the left ventricle outlet valve). Point *b* represents this situation. The ventricle then ejects its contents in the face of mildly changing ventricular (and aortic) pressure. The segment of curve *b-c* in the pressure volume diagram represents this ejection process.

The ventriculoaortic pressure difference reverses its direction as the active contractile process of myocardium reaches and passes the peak, and the aortic valve closes shortly afterward. The end of ejection is represented by point *c*.

Subsequently, the ventricular diastole starts, that can be divided in two phases: isovolumic relaxation and filling. First, the ventricle undergoes the isovolumic relaxation process, which is represented by the line segment *c-*

7

d. As the ventricular pressure falls below the atrial pressure at point *d*, the mitral valve opens and the relaxing ventricle fills along the curve segment *d-a*.

The volume of ejected blood, or stroke volume (SV) is represented by the horizontal distance *b* to *c* in the pressure-volume diagram and the vertical distance *b* to *c* in the volume time function curve.

Ventricular Preload and Afterload

The ventricle working conditions are represented by the concepts of preload and afterload. Preload and afterload definitions usually vary with the purpose of the given study. There is therefore no unique definition of these terms (Sagawa et al., 1988, p. 28).

Common definitions of ventricular preload are the end diastolic ventricular pressure or volume, or alternatively the atrial pressure. The preload represents the load seen during ventricle filling at the moment before contraction (point *a* in Figure 1.7a).

The afterload is a measure of the opposition to the ventricular ejection. Common definitions of ventricular afterload are the mean arterial pressure, the end systolic ventricular pressure (point *c* in Figure 1.7a) or the arterial input impedance. The arterial input impedance is an expression of the dynamic property of the arterial system as it opposes pulsatile flow injected by the ventricle into the arterial system. This is the ratio of arterial pressure to arterial flow and it is expressed as a complex variable in the frequency domain.

In (Sagawa et al., 1988, p. 111) preload and afterload effects on the ventricular PV loop are commonly recognized and tested as shown in Figure 1.8.
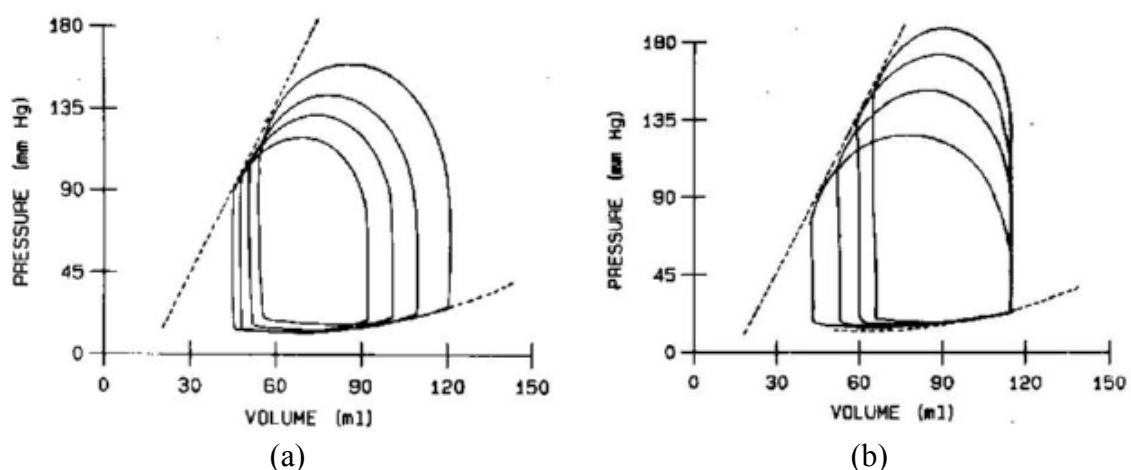

Figure 1.8 – (a) effect of changing end diastolic pressure (preload) with afterload impedance kept constant; (b) effect of combinations of a constant end-diastolic volume and varying resistive term of the arterial impedance (afterload), which leads to varying arterial pressure (Sagawa et al., 1988, p. 113).

The end systolic pressure volume relationship (ESPVR) is defined by the line drawn tangentially to the upper left shoulders of the loops. If the ESPVR is linear in the PV plane, its slope is the E_{max} previously introduced. The end diastolic pressure volume relationship (EDPVR) is the curve that connects all the end diastolic points of different loops. As it can be noticed by the Figure 1.8 both the ESPVR and the EDPVR are independent on the ventricle working conditions.

The following can be stated for preload and afterload effects on the ventricle mechanics.

For an decrease of preload (decreased atrial pressure), the flow rate delivered by the ventricle increases (Q); both end-systolic and end-diastolic volumes, ESV and EDV, decrease, but the latter more. As a consequence, stroke volume (SV) and mean ventricular volume (Vmean) decrease; mean arterial systemic pressure (Pas-mean) decreases as well. By using the same symbols as above, for an increase of the resistive component of the arterial impedance (afterload), keeping the preload constant, the flow rate decreases; the end-systolic volume increases. The stroke volume decreases, while mean ventricular volume increases; mean arterial systemic pressure increases.

Summarizing we have schematically:

Preload↓ → Q↓↓, ESV↓, EDV↓↓, SV↓↓, Vmean↓, Pas-mean↓
Afterload↑ → Q↓, ESV↑, EDV=, SV↓, Vmean↑, Pas-mean↑↑

where upward arrows are for increased quantities, while downward arrows are for decreased quantities; double arrows mean a more relevant increase/decrease.

This mechanism, by means of which the stroke volume depends on both the preload and afterload, constitutes the so-called "Starling control" or "heterometric control" (Sarnoff et al., 1960).

An atrium-ventricle unit, considered as a pump, can be functionally characterized by means of a relationship that links the mean value of the cardiac output during the cycle with the mean atrial pressure (preload) and the mean arterial pressure (afterload). The mean output increases with increasing preload and decreasing afterload and, in normal physiological conditions, is extremely sensitive to preload variations and less affected by changes in the afterload. Figure 1.9 shows the surface enveloping different cardiac functions of the left ventricle of a dog (Sagawa et al., 1988, p. 161), generated by the heart's fundamental control mechanism.

This "Starling/heterometric control" mechanism is present and active even in a denervated and isolated myocardium. The other control mechanism, called "homeometric control" (Sarnoff et al., 1960) and actuated at a higher hierarchic level with respect to the Starling's control, produces a shift of the surface shown in Figure 1.9 and thus generates a "family" of output/preload/afterload functional surfaces.
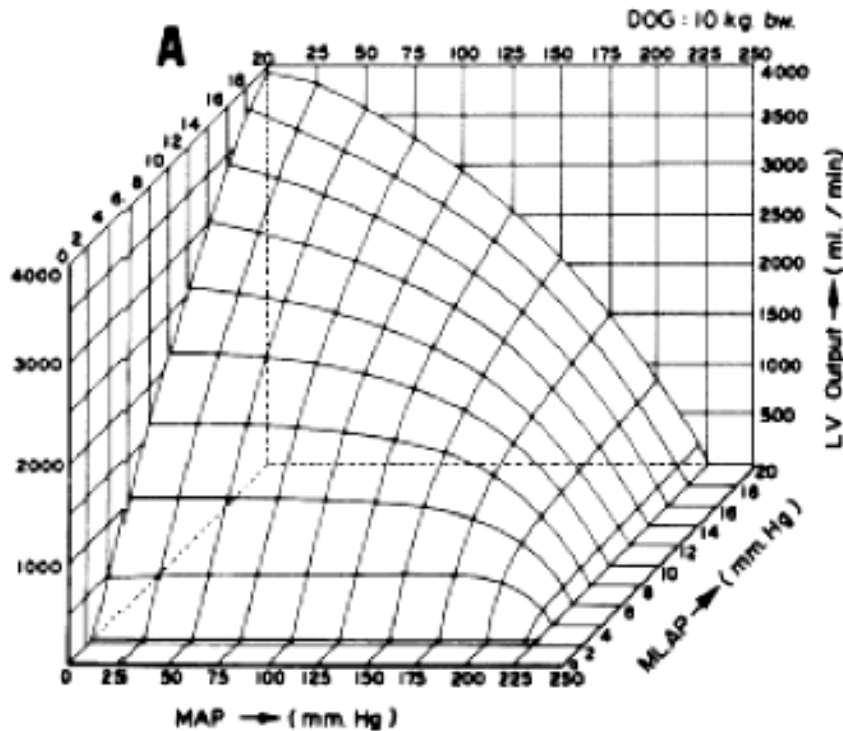
Figure 1.9 – surface enveloping the cardiac function curves of the left ventricle in a dog (Sagawa et al., 1988, p. 161). MLAP = mean left atrial pressure; MAP = mean arterial pressure.

From a pressure-volume relationship standpoint, this is equivalent to the change in slope of the ventricular end systolic pressure volume relationship. If the contractility of the ventricle is augmented, for example by using positive inotropic agents, the slope of the ESPVR increases without any change of the volume axis intercept V_0. On the contrary, the slope decreases if ventricular contractility diminishes (due to a pathology or pharmacological injection). Therefore cardiac output increases, through a stroke volume increase, in the first case, while decreases in the second case through a stroke volume decrease.

Stroke work, mechanical efficiency, wall stress

The total energy generated by each contraction is represented by the total area under the ESPVR and above the EDPVR. This area is called systolic pressure-volume area, denoted by PVA (Suga, 1990). As it is shown in Figure 1.10, PVA consists of external mechanical work performed during systole to propel the blood into the circulation, called stroke work (SW), and elastic potential energy (PE) presumed to be stored in the myocardium at end systole. The potential energy degrades into heat when it is not used as for external work during the isovolumic relaxation.

Mechanical efficiency is defined as the ratio between the SW and the total oxygen consumption. The latter is linearly related to the PVA. Therefore the mechanical efficiency of the ventricle pump can be re-defined as the ratio between SW and PVA.
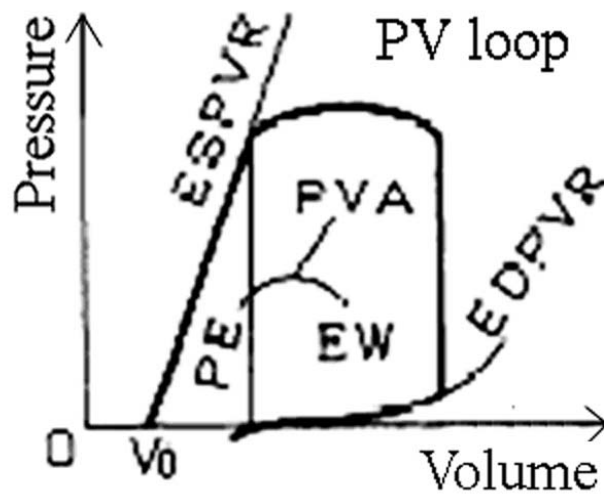
Figure 1.10 – pressure-volume area (PVA) in contractions; EW is the external work, PE the potential energy; partially modified from (Suga, 1990).

In (Sarnoff et al., 1958) it was demonstrated that one of the primary determinants of myocardial oxygen consumption is the stress in the myocardium. The ventricular wall is a non-homogeneous, anisotropic material with nonlinear elasticity that is composed of layers of fibers with different orientations embedded in connective tissue. A complex stress distribution can thus be expected. However, it has been demonstrated experimentally that LV wall stress is distributed homogeneously and that a single value can be used to indicate the wall stress for the whole wall (Arts et al., 1991). In the simplest model for wall stress calculation, the ventricle is approximated as a spherical shell Figure 1.11.
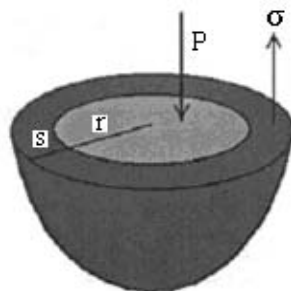
Figure 1.11 – spherical shell ventricle approximation.

Laplace's law can then be applied to relate ventricular wall stress σ to the ventricular pressure P, the inner radius r, and the wall thickness s.

$$\sigma = \frac{P}{\dfrac{s}{r} \cdot \left(2 + \dfrac{s}{r}\right)} \qquad (1.4)$$

1.3. *Vascular system*

The circulation, as previously stated, is divided into systemic and pulmonary circulation. The first supplying all the tissues of the body except the lungs, the second supplying the lungs.

There are several ways to describe the vascular system. All these representation of the vascular system take into account its resistance to blood flow, vascular distensibility/compliance and reservoir properties.

Table 1.1 shows the percentage of the total blood volume in major segments of the circulation (Guyton and Hall, 2000, p. 145). For instance, about 84% of the entire blood volume of the body is in the systemic circulation, and 16% in heart and lungs. Of the 84% in the systemic circulation, 64% is in the veins, 13% in the arteries, and 7% in the systemic arterioles and capillaries. The heart contains 7% of the blood, and the pulmonary vessels, 9%.

Table 1.1: distribution of blood (in percentage of total blood) in the different parts of the circulatory system.

heart	7%
pulmonary circulation	9%
arteries	13%
arterioles and capillares	7%
veins, venules and venous sinuses	64%

Pressures in various portions of the circulation are displayed in Figure 1.12. Because the pumping by the heart is pulsatile, the arterial pressure fluctuates between a systolic and diastolic pressure levels: in the systemic circulation between 120 mmHg and 90 mmHg (mean 100 mmHg) and in the pulmonary between 25 mmHg and 8 mmHg (mean 16 mmHg). Pressure is about 0 mmHg in the systemic veins and 7 mmHg in the pulmonary veins; 0 mmHg in the right atrium and 2 mmHg in the left atrium.
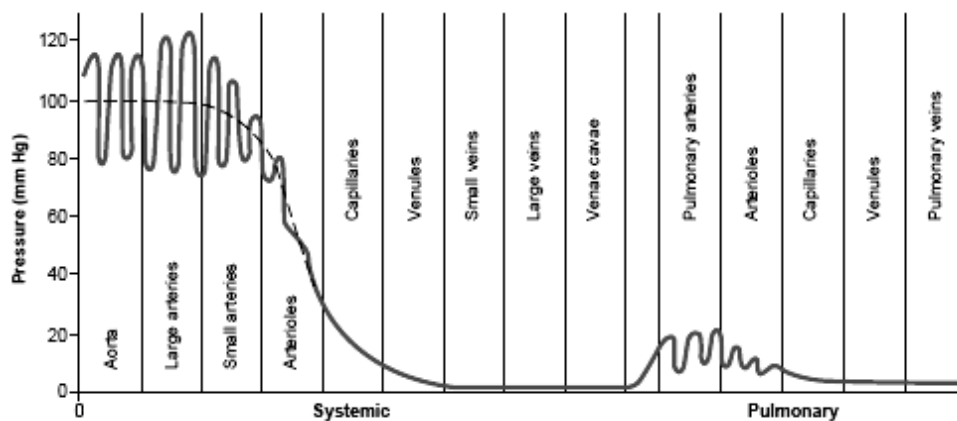
Figure 1.12 – normal blood pressures in the different portions of the circulatory system when a person is lying in the horizontal position (Guyton and Hall, 2000, p. 145).

The normal cardiac output in the adult male is about 100 mL/sec (i.e. 6 L/min), the pressure drop between the systemic arteries and systemic veins is about 100 mmHg. Therefore the flow resistance of the entire systemic circulation is 1 mmHg*s/mL. The pressure drop in the pulmonary circulation is about 14 mmHg, and the flow resistance of the entire pulmonary circulation is 0.14 mmHg*s/mL.

Distensibility and compliance relate pressure and volume in the vessels. A convenient method for expressing the relation between these two quantities is the use of the so-called pressure-volume curve (Figure 1.13).
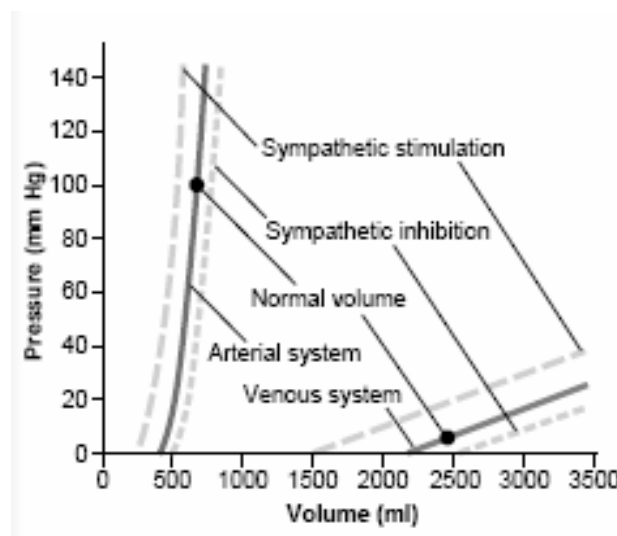
Figure 1.13 – volume-pressure curves of the systemic arterial and venous systems, showing also the effects of sympathetic stimulation and inhibition (Guyton and Hall, 2000, p. 153).

When the systemic arterial system of the average adult person is filled with about 660 mL of blood, the mean arterial pressure is 100 mmHg, but when filled with only 500 mL the pressure fall to zero. The ratio between the increase in volume and the increase in pressure ($\Delta V/\Delta P$) is the compliance. For the arterial system this ratio is about 1.6 mL/mmHg.

In the entire systemic venous system the volume of blood normally averages from 2000 to 3000 mL, and tremendous changes in this volume are required to change the venous pressure. The venous compliance is much higher then the arterial one and equals circa 50 mL/mmHg. Curves intercept of the volume axis are the unstressed volumes.

Input vascular impedance

To describe the arterial system a representation that is particular powerful uses the concept of vascular input impedance. Input impedance expresses the "opposition" of the vessels to pulsatile flow in the same way that vascular resistance expresses their opposition to steady flow. Input impedance can be calculated by frequency analysis of pressure and flow

pulsation, both of which are measured at the root of the ascending aorta or pulmonary artery, and it is expressed as a complex variable in the frequency domain. Impedance at these sites, the origin of systemic and pulmonary circulations, has a fundamental importance: the impedance represents the afterload for the ventricles and determines how much work must be done by the ventricles to produce a given pulsatile flow.

Systemic arterial load

Input impedance in the ascending aorta has been measured by many investigators, in man as well as in the dog and a few other mammals. A typical spectrum in the dog (O'Rourke and Taylor, 1967) is shown in Figure 1.14, together with results averaged from five normal human subjects (Nichols et al., 1977).

(a)   (b)
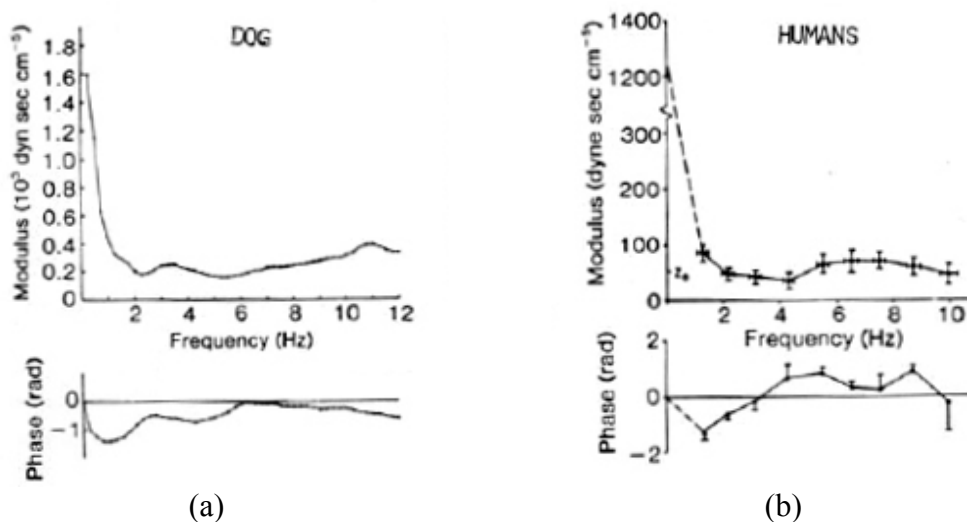
Figure 1.14 – (a) input impedance in the ascending aorta as a function of frequency in the dog, calculated by spectral analysis (O'Rourke and Taylor, 1967); (b) average measurements in five normal adult human subjects, calculated by Fourier series; vertical and horizontal bars indicates standard errors of means (Nichols et al., 1977).

The ratio of mean arterial pressure to mean flow is plotted at $f = 0$. This term can be regarded as the impedance at frequency of zero, usually referred to as the input resistance, and it is considerably higher than the impedance to pulsatile waves. The amplitude falls sharply from 0 to 2 Hz. Phase angles are negative between 0 and about 3 Hz, indicating that flow leads pressure. At higher frequencies swings of impedance amplitude and phase are the result of reflected waves that are always present in the arterial system. Reflected waves are present because consecutive segments of the vascular tree differ in their dimensions and elasticity causing impedance "mismatching". Usually an early minimum in the magnitude is observed around 2-3 Hz and another at 5-8 Hz. These two minima can be related to the existence of two discrete major reflecting sites (Milnor, 1989, p. 182).

The extent to which the input impedance rises and falls with frequency depends on the size of waves reflected from the periphery; the greater the reflection factor, the larger the oscillation. Peripheral vasoconstriction increases oscillations and dilatation reduces them. With increasing age the oscillation increases as well. Oscillations occur about a value called characteristic impedance (Z_0 in Figure 1.14b). This value is a function of the number of arterial tree branches, of their radius and, most important of their elasticity.

Pulmonary arterial load

The input spectrum in the main pulmonary artery is similar to that of the aorta but lower in amplitude. The spectrum is shown in Figure 1.15 (Milnor, 1990, p. 370).
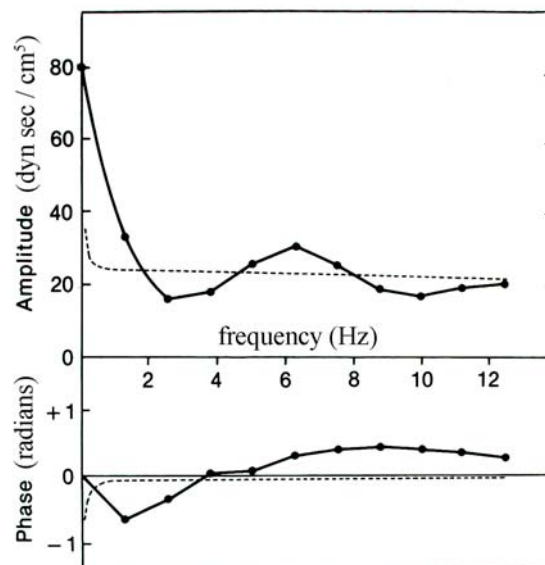
Figure 1.15 – input impedance (solid line) in main pulmonary artery of a human subject; characteristic impedance (dashed line) (Milnor, 1990, p. 370).

The pulmonary and systemic circulation carry the same average volume flow per unit time, but pulmonary resistance is lower than that of the systemic bed (impedance at zero frequency). Furthermore because of relatively higher compliance of the pulmonary artery the characteristic impedance is also lower than that of the systemic circulation, approximately 20 dyne*sec/cm^5 compared to about 50 dyne*sec/cm^5 in the ascending aorta. The pulmonary arterial input impedance spectrum, like that of ascending aorta, falls steeply from a relatively high value at zero frequency to a minimum at 2-4 Hz, followed by a maximum at 6-8 Hz and smaller fluctuation at higher frequency. The early minimum is easily recognized in most individuals, perhaps because the relative symmetry of the pulmonary vascular tree creates a fairly uniform distribution of reflecting sites.

1.4. Cardiac output regulation

The ability of the heart to pump blood can be expressed in terms of "cardiac output curves", and the tendency for blood to flow through the systemic circulation back to the heart can be expressed in terms of "venous return curves" (Guyton et al., 1973, p. 237).

A cardiac output (CO) curve or a venous return (VR) curve relates the same two variables: flow and right atrial pressure. The point at which the two curves cross is called *equilibrium point* Figure 1.16.
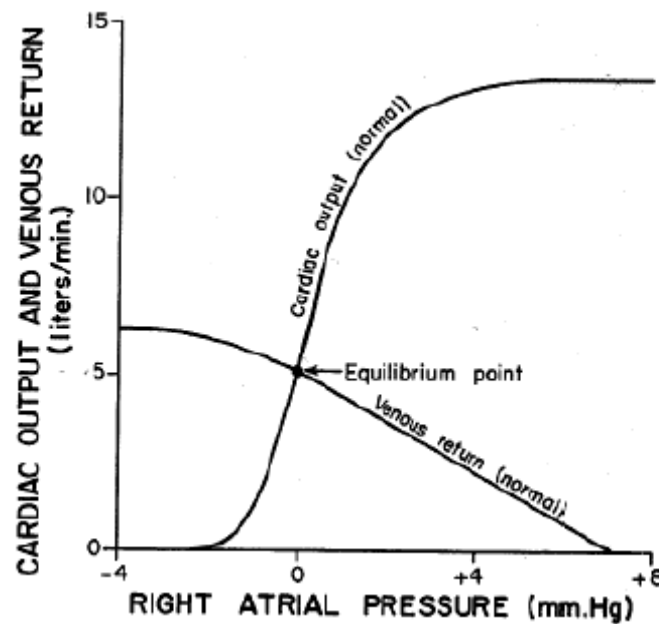
Figure 1.16 – cardiac output curve and venous return curves (Guyton et al., 1973, p. 238).

The cardiac output curve shows that the ventricle is able to pump more blood when its filling pressure (atrial pressure) is increasing (Guyton et al., 1973, p. 148). Whether the venous return curve shows that increasing atrial pressure will reduce venous return flow because of a decrease of the venous pressure gradient (Guyton et al., 1973, p. 138).

Flow in the whole circuit is equal to both cardiac output and venous return, except during transient states for only a few seconds at a time. Experimental studies have shown that when venous return and cardiac output are temporarily out of equilibrium, the equilibrium is re-established in approximately six heart beats (Buckley et al., 1955).

In general, only two mayor patterns of cardiac output curves occur: a pattern of curves that depicts the effects of increased and decreased effectiveness of the heart as a pump, and a pattern that depicts the effects of increased or decreased extra-cardiac pressure. There are also two major patterns of venous return curves: a family of curves that results from alterations in the mean systemic pressure and a family resulting from

alterations in resistance to venous return. Both patterns, together with the definitions of mean circulatory, mean systemic, mean pulmonary pressures, and resistance to venous return will be described in detail in the following paragraphs.

An important note must precede the following sections on cardiac output regulation. What is presented here is a just framework that must be always compared with the daily clinical practice, which is, in fact, much more complex than every mathematical model. This framework represents a method to analyze of cardiac output complex regulation. Another point must be borne in mind: the mathematical representations of venous return, cardiac function and their interaction do not take into direct account the regulation mechanisms due to reflexes, blood volume changes or stress relaxation of the circulation, and still others. These mechanisms must be included into the analysis because they are present in the clinical practice. They act on the parameters of cardiac and venous functions and work together with the basic regulation mechanisms to make them even more effective (Guyton et al., 1973, p. 494).

Circulatory, systemic and pulmonary mean pressures (Guyton et al., 1973, p. 205)

The mean circulatory pressure (*Pmc*) is the pressure that would be measured at all points in the entire circulatory system (systemic and pulmonary circulations) if the heart were stopped suddenly and the blood were redistributed in the whole circulation in such a manner that all pressures were equal.

The mean systemic pressure (*Pms*) is the pressure that would be measured at any given instant anywhere in the systemic circulation if all inflow and all outflow from the systemic circulation were to cease suddenly and the blood were redistributed in such a manner that the pressure would be the same in each part of the systemic circulation.

The mean pulmonary pressure (*Pmp*) is the same measurement in the pulmonary circulation.

The mean circulatory pressure is a measure of the degree of filling of the whole circulation with blood. If the holding capacity of the circulatory system is very great but the blood volume is very low, the mean circulatory pressure will be very low. On the other hand, if the holding capacity of the circulation is low but the blood volume is great, the mean circulatory pressure will be high. Likewise, the mean systemic pressure is a measure of the degree of filling of only the systemic circulation, and the mean pulmonary pressure is a measure of the degree of filling of only the pulmonary circulation. If a circulatory system is filled only slightly with blood, not enough to stretch the vessels at all, no pressure will develop in the peripheral vessels, and without pressure there will be no force to move

blood toward the heart. As a consequence, the cardiac output will be zero however actively the heart might pump.

All the pressures throughout the different parts of the circulation are quantitatively dependent upon these mean pressures. Indeed, the quantitative value of the mean circulatory pressure is the weighted average of the pressures in all segments of the circulation when each of these pressures is weighted in proportion to the capacitance of each segment. Likewise, the mean systemic and mean pulmonary pressures are weighted averages for the systemic and pulmonary circulations, respectively.

The capacitance of the systemic circulation is about seven times as great as that of the pulmonary circulation. This lead to a relationship between mean circulatory pressure, mean systemic pressure, and mean pulmonary pressure that can be represented as in Figure 1.17.
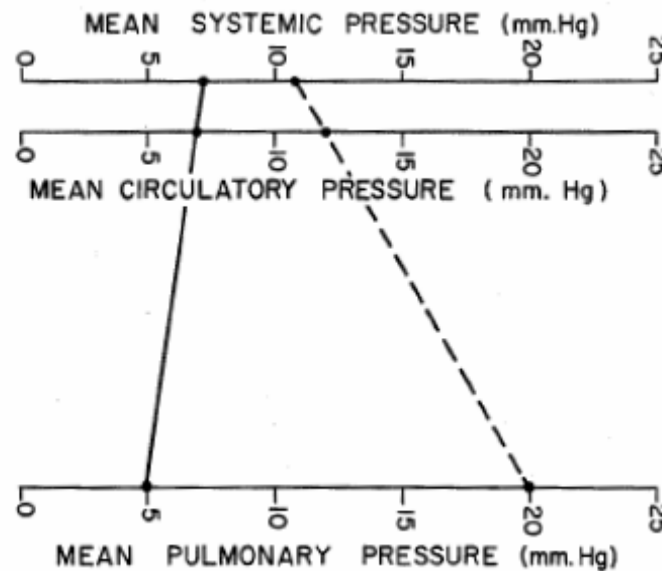
Figure 1.17 – nomogram showing the interrelationships between the mean circulatory pressure, mean systemic pressure, and mean pulmonary pressure; the solid line across the graph shows the normal values; the dashed line shows representative values in serious left heart failure (Guyton et al., 1973, p. 211).

Also, the following equation can be written according to (Guyton et al., 1973, p. 211):

$$Pmc = \frac{7 \cdot Pms + Pmp}{8} \qquad (1.5)$$

this equation states that Pmc is determined 7/8 by the Pms and only 1/8 by the Pmp, furthermore when blood shifts from the systemic circulation into the pulmonary circulation or in the opposite direction, the Pmc stays constant.

Patterns of cardiac output curves

Figure 1.18 illustrates a "family" of cardiac output curves which depict the ability of the heart to pump blood at all degrees of cardiac

effectiveness. Any factor that increases the effectiveness of the heart as a pump elevates the cardiac output curve and shifts it slightly to the left, whereas almost all factors that decrease the effectiveness of the heart as a pump depress the curve and shift it slightly to the right.
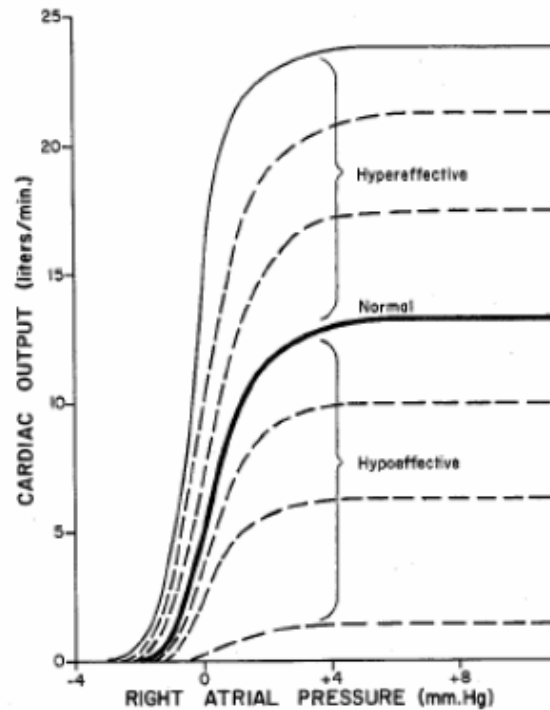
Figure 1.18 – family of cardiac output curves for hypo-and hypereffective hearts (Guyton et al., 1973, p. 240).

The upper solid curve represents approximately the maximum ability of the normal heart to pump blood when it is operating in its almost effective state. Obviously, the curve which would depict the minimal ability of the heart to pump blood would be a curve along the zero cardiac output axis. Between these two extremes are an infinite number of cardiac output curves which can depict the pumping ability of hearts with any degree of effectiveness of the heart from zero up to an effectiveness approximately two-thirds above normal.

The following is a list of the factors that can cause the heart to become a more effective pump than usual:

1. sympathetic stimulation;
2. cardiac hypertrophy;
3. decreased load on the heart;
4. inhibition of the parasympathetics to the heart.

The different factors which can cause a hypoeffective heart are numerous, but some of them can be listed as follows:

5. myocardial infarction;
6. valvular heart disease;
7. vagal stimulation of the heart;

8. inhibition of the sympathetics to the heart;
9. congenital heart disease;
10. myocarditis;
11. cardiac anoxia;
12. diphtheritic or other types of myocardial damage or toxicity.

Figure 1.19 shows the different patterns of curves which occur when the extracardiac pressure is altered. The solid line curves represent the effects of changes in intrapleural pressure. The dashed curves illustrate the effect of cardiac tamponade on the curves.
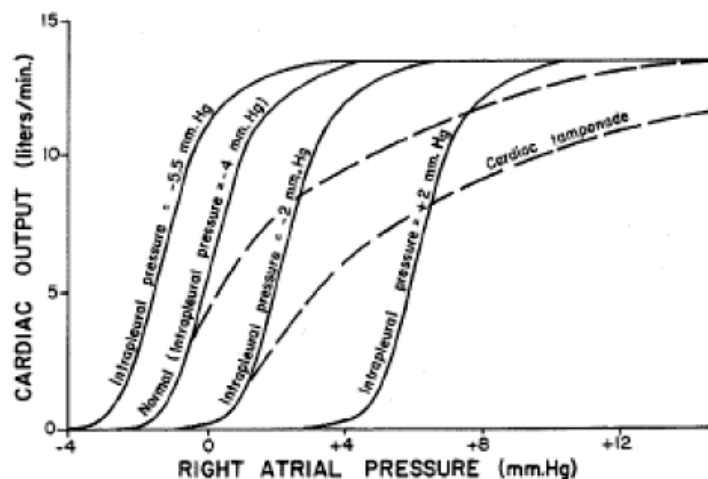
Figure 1.19 – family of cardiac output curves caused by changes in intrapleural pressure and by cardiac tamponade (Guyton et al., 1973, p. 242).

Change in cardiac output curves due to intrapleural pressure are important when considering the opened chest setting, where this pressure equals the atmospheric pressure, 0 mmHg, instead of the normal negative value of –4 mmHg.

Patterns of venous return curves

Figure 1.20 illustrates a family of venous return curves that occurs when the mean systemic pressure is altered. The normal curve is shown when the mean systemic pressure is 7 mmHg. The lowest solid curve shows the venous return curve when the mean systemic pressure is one-half normal, or 3.5 mmHg, and the solid curve to the far right shows the effect of elevating the mean systemic pressure to 14 mmHg. The dashed curves illustrate that there is an infinite number of other curves, all of which parallel each other and each one of which is determined by the level of the mean systemic pressure.

The different factors that can change the mean systemic pressure and that therefore can alter the venous return curve as illustrated in Figure 1.20 are the following:

1. changes in vasomotor tone;
2. changes in blood volume;

3. changes in interstitial fluid volume;
4. changes in intra-abdominal pressure;
5. changes in muscular compression of the vascular system.
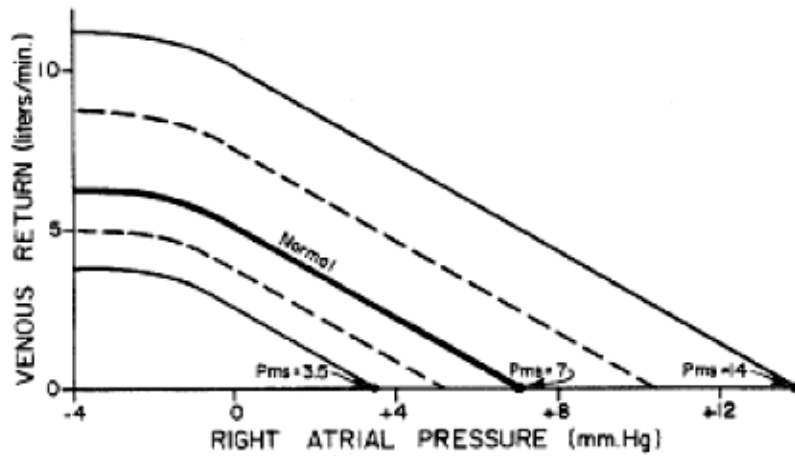
Figure 1.20 – family of venous return curves that occurs when the mean systemic pressure is altered (Guyton et al., 1973, p. 243).

Figure 1.21 illustrates the family of venous return curves resulting from alterations in resistances to venous return. The solid curves represent normal resistance, one-half the normal resistance, and two times the normal resistance. The dashed curves indicate that there is an infinite series of such curves. All these curves reach zero venous return axis at a right atrial pressure of 7 mmHg. In other words, the mean systemic pressure is 7 mmHg for each of these curves.
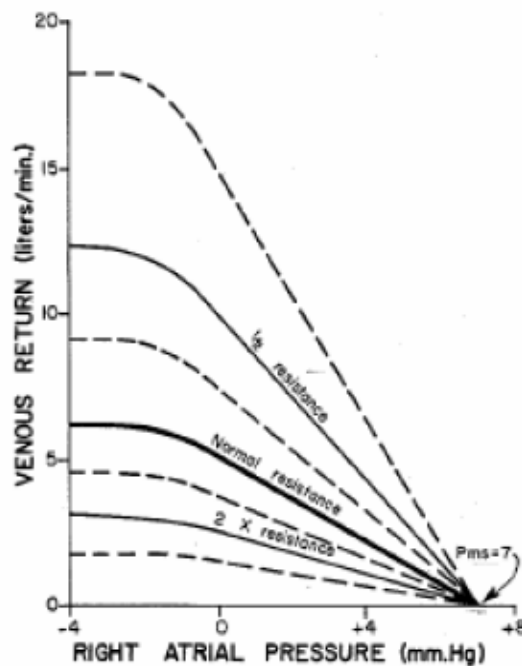
Figure 1.21 – family of venous return curves depicting the effect of altering the resistance to venous return (Guyton et al., 1973, p. 244).

21

The different factors that can affect the resistance to venous return, and that thereby affect the venous return curve, are:

1. change in the total peripheral resistance resulting from dilatation or constriction of the blood vessels or from increase or decrease in blood viscosity;
2. A-V fistulae or other types of shunts;
3. change in the ratio of arterial resistance to venous return;
4. alteration in the relative capacitances of the arterial and vascular trees.

Mathematical equations for the venous return curve

To understand the regulation of cardiac output, Guyton and his colleagues developed an expression, equation (1.6)0F in (Guyton et al., 1973, p. 255), which describes the venous return curve of Figure 1.16 and its dependence on mean systemic pressure (Figure 1.20) and resistance to venous return (Figure 1.21). The derivation of the following equation will borne in mindbe presented in the following.

$$CO = \frac{Pms - Pra}{\dfrac{Cv_s \cdot Rv_s + Ca_s \cdot (Rv_s + Ra_s)}{Cv_s + Ca_s}} \qquad (1.6)^1$$

The denominator of equation (1.6) is actually a resistance, because in a dimensional analysis of this denominator one finds that the capacitances cancel out. Therefore, the entire denominator can be called the *resistance to venous return*. It represents an algebraic average of all the resistances from the different areas of the systemic circulation back to the right atrium when each of these resistances is weighted in proportion to the capacitance of the individual area.

The determinants of cardiac output in this formula are basically the mean systemic pressure (*Pms*), the right atrial pressure (*Pra*), the systemic venous resistance (Rv_s), the systemic arterial resistance (Ra_s), the systemic venous capacitance (Cv_s), and the systemic arterial capacitance (Ca_s). The resistances and capacitances are functions of the dimensions and physical characteristics of the vessels, and the mean systemic pressure is mainly a function of blood volume in the systemic circulation in relation to the capacitances. The right atrial pressure is mostly determined by the pumping ability of the heart. All this variables are modified by reflexes, blood volume changes and other factors, and whose results produce the family of curves of Figure 1.20 and Figure 1.21

By referring to Figure 1.22, which illustrates a simplified schema of the circulation that considers the heart and lungs to be a single segment, and

---

[1] Equations (1.6)0F to (1.13) are taken form pp. 255-260 of Guyton AC, Jones CE, Coleman TG. 1973. Circulatory Physiology: Cardiac Output and its Regulation. 2nd ed: W.B. Saunders Company. 556 p.

the arterial and the venous vascular trees to be two other major segments of the circulation, equation (1.6) can be explained. The resistance Ra_s is the resistance from the mid-point of the arterial vascular tree to the mid-point of the venous tree to the right atrium. The capacitance Ca_s is the capacitance of the arterial tree, and the capacitance Cv_s is the capacitance of the venous tree. The pressure Pa_s is the systemic arterial pressure and the pressure Pv_s is the pressure at the midpoint of the venous tree. The volume EV_a is the extra volume in the arterial tree over and above that amount which is required to fill the arterial tree without any pressure. The volume EV_v is the extra volume in the venous tree in addition to that amount which barely fills the vessels without any pressure.
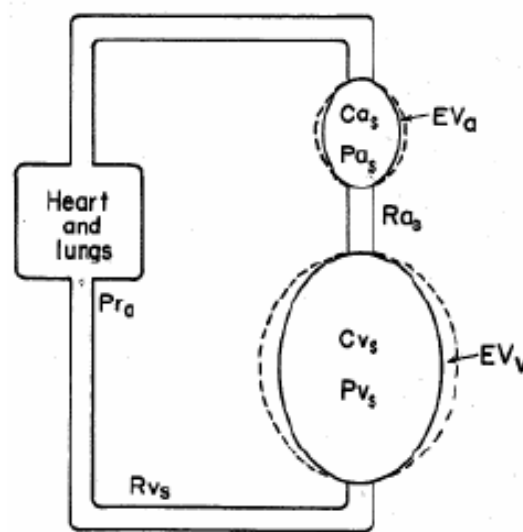
Figure 1.22 – schematized circulatory system used as the basis for deriving equation (1.6) (Guyton et al., 1973, p. 256).

When the venous tree is inadequately filled with blood, the blood obviously will not flow the rest of the way into the heart. If, on the other hand, the capacitance vessels become well filled, their pressure will rise high, and blood will flow into the heart with great ease. Clearly, therefore, the degree of filling of the vessels is one of the major factors affecting blood flow from the peripheral circulation into the heart. To express this another way, it's the ratio of the blood extra-volume to the capacitance of the systemic circulation that determines how high the average peripheral pressures (mainly the venous pressure) will be and, therefore, that also determines the ease with which blood can flow around the circulation. This ratio of blood extra-volume to the capacitance of the systemic circulation has been unified in the concept of mean systemic pressure.

However, briefly, the mean systemic pressure rises (a) when the blood volume increases, (b) when the vascular tone increases, or (c) when the vasculature is compressed externally, such as during muscular contraction or abdominal compression. Conversely, this pressure decrease (a) when the

vasculature tone decreases or (b) when the blood volume decreases. Changes in the mean systemic pressure clearly affects the venous return (see equation (1.6) and Figure 1.20)

The venous return is inversely proportional to the quantitative value of the resistance to venous return. The slope of the venous return curve is proportional to the quantitative value of the denominator of equation (1.6), which means that one can calculate the resistance to venous return from the slope of the venous return curve (Figure 1.16). A decrease in resistance to venous return rotates the venous return curve in a clockwise direction, the curve approaching the vertical as the resistance approaches zero. An increase in resistance to venous return rotates the curve in the counterclockwise direction, the curve approaching the horizontal as the resistance approaches infinity (Figure 1.21).

By looking at Figure 1.22, equation (1.6) can be derived as follows. The pressures in the arteries and veins are equal respectively to the right atrial pressure plus the pressure drop from the arteries to the right atrium of from the veins to the right atrium. Thus,

$$Pv_s = CO \cdot Rv_s + Pra \tag{1.7}$$

$$Pa_s = CO \cdot (Rv_s + Ra_s) + Pra \tag{1.8}$$

The extra volume in each of the two major vascular trees is equal to the pressure times the capacitances. Thus, utilizing the pressures from equation (1.7) and (1.8), the following expressions are derived:

$$EVv_s = \left(CO \cdot Rv_s + Pra \right) \cdot Cv_s \tag{1.9}$$

$$EVa_s = \left[CO \cdot (Rv_s + Ra_s) + Pra \right] \cdot Ca_s \tag{1.10}$$

The mean systemic pressure is equal to the total extra volume (EV_s) of blood in the systemic circulation above that required to fill the system with no pressure (unstressed volume) divided by the total capacitance of the systemic circulation (C_s). Therefore, for the mean systemic pressure, the following expression can be written:

$$Pms = \frac{EV_s}{C_s} = \frac{EVv_s + EVa_s}{Cv_s + Ca_s} \tag{1.11}$$

It will be noted from this expression that the total extra volume in the systemic circulation (EV_s) is equal to the sum of the extra volumes in the veins and arteries, and the total capacitance (C_s) of the systemic circulation is equal to the sum of the capacitances of the veins and arteries.

Now by substituting the expressions for the extra volumes in the veins and arteries derived in equations (1.9), (1.10) and (1.11) and by solving for CO, equation (1.6) is obtained:

In essence, equation (1.6) states the following relationships in the circulation:

1. the cardiac output is proportional to the mean systemic pressure minus the right atrial pressure;
2. when the heart fails, which causes the right atrial pressure to rise, the upper limit to which the right atrial pressure can rise is equal to the mean systemic pressure;
3. however high the right atrial pressure rises, the cardiac output falls proportionately as the right atrial pressure approaches the mean systemic pressure.

In other words these first three statements emphasize that the difference between the mean systemic pressure and the right atrial pressure is the major determinant of cardiac output;

4. if all the resistances in the systemic circulation are increased proportionately, including the venous resistance as well as the arteriolar resistance, the cardiac output will decrease in proportion to the increase in systemic resistances (e.g.: extreme reduction of cardiac output even with inadvertently compression of inferior vena cava);
5. if all capacitances of the systemic circulation are altered proportionately without affecting the mean systemic pressure, when for example a decreased vessels compliance and contemporary depletion of blood occurs, the cardiac output will be unchanged;
6. a given change in venous resistance will cause a far greater effect on cardiac output than a similar change in arterial resistance (e.g.: difference in reduction of cardiac output after aortic banding or vena cava occlusion). The venous capacitance, Cv_s, is approximately 18 times as great as the arterial capacitance, Ca_s. By substituting into equation (1.6) the relative ratios of the venous and arterial capacitances, the following relationship is obtained.

$$CO \propto \frac{Pms - Pra}{\dfrac{18 \cdot Rv_s + 1 \cdot (Rv_s + Ra_s)}{19}} \propto \frac{Pms - Pra}{Rv_s + \dfrac{Ra_s}{19}} \qquad (1.12)$$

Equation (1.12) states that a given change in venous resistance could cause as much as 19 times as great an effect in cardiac output as the same change in arterial resistance.

A formula analogous to equation (1.6) can be derived for the pulmonary circulation.

$$CO = \frac{Pmp - Pla}{\dfrac{Cv_p \cdot Rv_p + Ca_p \cdot (Rv_p + Ra_p)}{Cv_p + Ca_p}} \qquad (1.13)$$

Equation (1.13) gives one an analysis of the interrelationships between cardiac output, mean pulmonary pressure, left atrial pressure, pulmonary capacitances, and pulmonary resistances.

Mathematical equations for the cardiac output curve

While equations (1.6) and (1.13) can be used to draw the venous return curves, two hyperbola equations, which fit almost exactly the cardiac output curves for the right and left heart, can be written according to (Guyton et al., 1963, p. 268), respectively :

$$F = Kr - \frac{5.3}{Pra - Pec - 3.3} \tag{1.14}$$

$$F = Kl - \frac{55}{Pla - Pec - 3} \tag{1.15}$$

where which F is the total flow in the circulation (equal to cardiac output and to venous return), Kr is a constant representing the pumping strength of the right heart, Kl is a similar constant for the left heart, Pra is the right atrial pressure, Pla is the left atrial pressure, and Pec is the extracardiac pressure (the pressure in the pericardium surrounding the heart), which is approximately equal to the intrapleural pressure under normal conditions. The constant Kr for the normal right heart is about 14, and Kl for the normal left heart is about 16 when F is expressed in L/min and the pressure are expressed in mmHg. Kr can increase to as high as 25 for the hyper effective right heart, and Kl can increase to 27 for the hyper effective left heart. Either constant can decrease to as low as zero for the hypoeffective heart.

1.5. Heart failure

Both the words "heart" and "failure" are quite explicit; therefore the term "heart failure" should mean very simply failure of the heart to pump blood as well as it does normally.

The New York Heart Association (NYHA) Functional Classification (Hunt et al., 2001) provides a simple way of classifying the extent of heart failure. It places patients in one of four categories (classes) based on how much they are limited during physical activity:

   I. no symptoms and no limitation in ordinary physical activity.

  II. mild symptoms and slight limitation during ordinary activity. Comfortable at rest.

 III. marked limitation in activity due to symptoms, even during less-than-ordinary activity. Comfortable only at rest.

 IV. severe limitations. Experiences symptoms even while at rest.

Heart failure is a complex clinical syndrome that can result from any structural or functional cardiac disorder that impairs the ability of the ventricle to fill with or eject blood. Among the numerous causes and types

of heart failure, those who are treated with mechanical circulatory support, and in particular ventricular assist devices (VADs) will be presented. They usually involve the heart failure NYHA class III and IV.

Postsurgical myocardial dysfunction (Zipes et al., 2004, p. 628)

Patients undergoing cardiac surgical procedures are at risk for myocardial injury owing to myocardial stunning and ischemia, insufficient myocardial protection, reperfusion injury, and cardiac arrhythmias. These patients my be categorized into two groups: those who had persistent or significant dysfunction prior to surgery and those who had adequate myocardial reserve prior to surgery. In general, for patient who cannot be weaned from cardiopulmonary bypass who maintain otherwise reasonable end-organ function, the best strategy is often the placement of a temporary VAD that may stabilize the patient long enough for transfer to a center with more experience and more choices of long term devices should the patient be deemed unweanable.

Cardiogenic shock resulting from acute myocardial infarction

Cardiogenic shock is the most severe clinical expression of left ventricular failure and it is associated with extensive damage of the left ventricular myocardium. The cardiac output is insufficient to supply the tissues of the body with their normal nutritive needs, therefore tissues on widespread areas of the body are being damaged by nutritive insufficiency.

Cardiogenic shock is characterized by marked and persistent (> 30 min) hypotension with systolic pressure less than 80 mmHg and marked reduction of cardiac index (generally < 1.8 l/min/m^2) in the face of elevated left ventricular filling pressure (pulmonary capillary wedge pressure > 18 mmHg) (Zipes et al., 2004, p. 1200). Mechanical complications should be suspected in any patient with acute myocardial infarction in whom circulatory collapse occurs.

Almost all myocardial infarctions result from coronary artherosclerosis, generally with superimposed coronary thrombosis (Zipes et al., 2004, p. 1141). When an artherosclerotic plaque disruption occurs, a sufficient quantity of thrombogenic substances is exposed, and the coronary artery lumen may become obstructed by a combination of platelet aggregates, fibrin, and red blood cells. Characteristically, such completely occlusive thrombi lead to a large zone of necrosis involving the full or nearly full thickness of the ventricular wall in the myocardial bed subtended by the affected coronary artery and typically produce the ST elevation on the electrocardiogram. If a sufficient quantity of the myocardium undergoes ischemic injury, left ventricular pump function becomes depressed; cardiac output, stroke volume, blood pressure and peak *dP/dt* are reduced; and end-systolic volume is increased.

Cardiogenic shock occurs when more than 40 percent of ventricular mass is lost to infarction; without some form of cardiac assistance, this condition is associated with 80% mortality (Chen et al., 1999).

Decompensated chronic heart failure

When the heart pumping effectiveness decreases, compensatory reflexes develop immediately increasing the heart contraction power and the vasomotor tone. Later on chronic adaptation occurs, by depression of urinary output below normal and by accumulation of fluid in the body with blood volume increase. All this factors cause overall increase of cardiac output together with higher mean systemic and pulmonary pressures.

However when the heart is severely damaged, compensation mechanisms are not able to reestablish a cardiac output compatible with survival. In this case fluid retention cause increase of cardiac output up to a value where any further retention in fluid will cause no beneficial effects but causing increasingly severe edema (Guyton et al., 1973, p. 459). Thus this is a state of decompensation, in which the cardiac output is too low to meet the requirements of the body and in which the fluid volume of the body never reaches a steady compensated level. This is a situation from which the circulatory system usually does not recover without complete body rest or other therapy.

In the absence of immediately available donor organ, VAD support for this indication allows establishment of hemodynamic stability, improvement of end-organ function, and the opportunity for nutritional support and rehabilitation before transplantation. For patients that are not candidates for transplantation (because of cancer, incurable infections or severe diabetes) permanent use of VAD is the only chance of survival.

Acute myocarditis (Zipes et al., 2004, p. 1697)

Myocarditis is one of the most challenging diagnoses in cardiology. The entity is rarely recognized, the pathopysiology is poorly understood, there is no commonly accepted diagnostic gold standard, and all current treatment is controversial.

Primary myocarditis is presumed to be due to either an acute viral infection or a postviral autoimmune response. Secondary myocarditis is myocardial inflammantion caused by a specific pathogen. These pathogens include bacteria, spirochetes, rickettisa, fungi, protozoa, drugs, chemicals, physical agents and other inflammatory diseases such as systemic lupus erythematosus (Zipes et al., 2004, p. 1697).

Patients with myocarditis can develop more spherical left ventricle, which is less efficient in myocardial contraction and mitral valve leaflet malcoaptation, causing additional functional deterioration. Patients with acute myocarditis have an indistinct onset of the disease with no clearly defined initial viral illness. They present with moderate severe left

ventricular dysfunction but usually mild dilatation. These patients have incomplete recovery or go on to develop progressive dilated cardiomyopathy.

LVAD implantation for acute myocarditis, particularly in young patients, may sometimes be used as a bridge to recovery rather than to transplantation.

2. Mechanical Circulatory Assist Devices

Mechanical circulatory assist devices evolved substantially since their inception in the late 1960s from an investigation strategy for the moribund to a standard therapy supporting patients with end-stage heart disease. Although medical therapy has advanced significantly during this time and had considerable effects on moderate heart failure, its influence on severe heart failure has been less substantial (Stevenson et al., 2001). Cardiac transplantation has traditionally represented the only treatment in end-stage heart disease, however, with donor availability limited to only 3000 annually worldwide, the impact of heart transplantation on heart failure has been described as "epidemiologically trivial" (Rose et al., 2001). Mechanical circulatory assist devices have as main goal to improve the survival and quality of life of such patients, bridging them to transplantation, to ventricular recovery or eventually being used for long-term and permanent support.

At present, together with widespread availability of intraaortic balloon pumps (IABPs) even in small hospitals, a broad array of sophisticated ventricular assist devices (VADs) both for univentricular, biventricular, short, long-term and permanent assist are accessible. The majority of VADs are nowadays used as bridge to transplantation, however because of shortage of donor organs permanent use and bridge to recovery represent a source of intense research and development. A multicenter trial was conducted to evaluate the use of left ventricle assist devices (LVAD) as permanent devices in the treatment of patient with heart failure .and contraindications to transplantation (Rose et al., 2001). This study, called REMATCH – Randomized Evaluation of Mechanical Assistance for the Treatment of Congestive Heart Failure, started in 1998 and included 129 patients in 20 centers using the HeartMate vented electric left ventricular assist device (VE LVAD) as the study device. The patients were randomly assigned to receive either an LVAD or maximal medical therapy, with death as primary endpoint. The study ended in 2001 and demonstrated a 48% reduction in the risk of death in patient group treated with LVADs compared with medically treated group (Figure 1.23).

Newer results with better pumps show even more preferable results with further decreased mortality (Lietz et al., 2007).
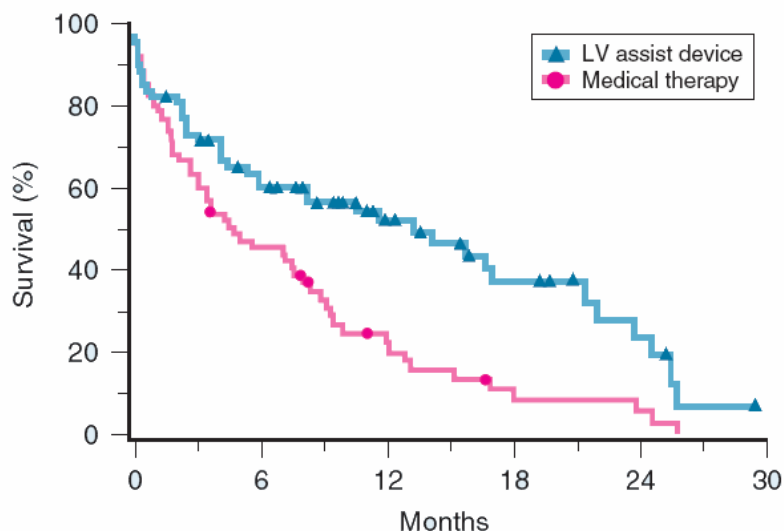
Figure 1.23 – comparison of actuarial survival curves from the Randomized Evaluation of Mechanical Assistance for the Treatment of Congestive Heart Failure (REMATCH). LV = left ventricular (Rose et al., 2001).

2.1. Indications for Ventricular Assist Devices support

Patients requiring mechanical support generally fall into four categories (Delgado et al., 2002):

1. postsurgical myocardial dysfunction;
2. cardiogenic shock resulting from acute myocardial infarction;
3. decompensated chronic heart failure (both transplant elegible and ineligible);
4. acute myocarditis and ventricular arrhythmias when pharmacological therapies and defibrillators have failed.

Hemodynamic eligibility criteria for mechanical cardiac assistance are substantially a cardiac index less than 2.0 liter/min/m^2, a systolic blood pressure less than 90 mmHg, left or right atrial pressures greater than 20 mmHg and a systemic vascular resistance greater than 2100 dyne*sec/cm^5 (Normal et al., 1977).

There are essentially four groups of patients for whom support with different types of VADs is appropriate. The first group consists of those in whom reversibility of ventricular damage is anticipated, the so called *bridge-to-recovery* group (Mueller and Wallukat, 2007, Mueller et al., 2002). The second, the *bridge-to-bridge* group, consists of patients who experience acute cardiogenic shock at a center that does not offer transplantation or long-term assist devices. In these cases the efficacious use of a short-term assistance and the rapid transfer to a center specialized in mechanical circulatory support are warranted (Helman et al., 1999). The

third is the traditional *bridge-to-transplantation* group, who meet criteria for transplantation and undergo VAD insertion to improve their overall candidacy for transplantation (Copeland et al., 2000). The last is the *destination therapy* group, who does not meet criteria for transplantation (Rose et al., 2001). In Figure 1.24 indications for ventricular assist device implantation are summarized together with the devices typically used for the intended therapeutic goals. Outcomes in terms of quality of life and survival are also displayed.

| | | | | Outcomes | |
| | | | | Short-Term | |
Intended Use	Therapeutic Goal	Devices	*Quality of Life*	*Survival* (days to weeks)	*Long-Term Survival* (months)
Bridge to recovery	Temporary support	IABP	+	++	0
		Centrifugal pump	+	+	0
		ECMO	+	+	0
		Abiomed	+	+	0
		HeartMate	+++	+++	+++
		Novacor	+++	+++	+++
Bridge to bridge	Stabilization to LVAD/BiVAD	Abiomed	+	++	0
		Centrifugal pump	+	+	0
		ECMO	+	+	0
Bridge to transplantation	Support to transplantation	HeartMate	+++	+++	+++
		Novacor	+++	+++	+++
		Thoratec BiVAD	++	++	++
		Abiocor/TAH	++	+	+
		Axial flow pump	+++	++	++
Destination	Permanent support	HeartMate	+++	+++	+++
		Novacor	+++	Undocumented →	
		Abiocor/TAH	+++	Undocumented →	
		LionHeart	+++	Undocumented →	

BiVAD = biventricular assist device; ECMO = extracorporeal membrane oxygenator; IABP = intraaortic balloon pump; LVAD = left ventricular assist device; TAH = total artificial heart.

Figure 1.24 – indications for VAD implantation (Zipes et al., 2004, p. 628).

2.2. Devices

There are a plenty of devices for mechanical circulatory support. Aim of this section is to give an overview of the working principles of these devices and to present some representative examples of such devices. A detailed description of currently available devices can be found in (Delgado et al., 2002, Mihaylov et al., 2000, Song et al., 2003).

In a purely subjective classification, devices for mechanical circulatory support can be categorized according to their pumping principle, in particular we distinguish positive displacement or rotary pumps.

Positive displacement pumps

Positive displacement pumps have a blood chamber that fills with blood during one part of the heart cycle and ejects the blood during the other part, thus working like the native heart. Most of this blood pump use a polyurethane sac as a blood chamber, or a rigid shell on one side and a membrane on the other (Figure 1.25). The membrane thus forms a barrier between the blood and the other pump components. Coatings are often applied on blood contacting surfaces in order to prevent thrombus formation and to spare the patient a heavy anticoagulation regime.

The blood chamber is usually connected, in the case of left ventricular assistance, to the apex of the LV and to the aorta by means of valved conduits/cannulas to direct the blood from the heart to the pump and further to the aorta. All the valves available for heart valve replacement are used in VADs.
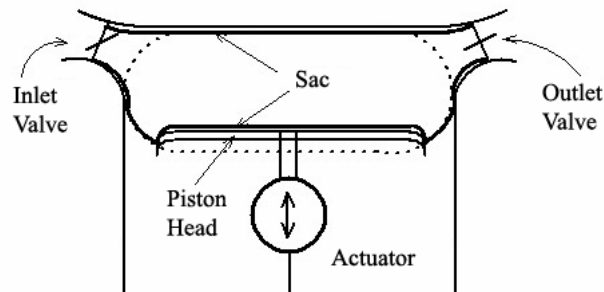
Figure 1.25 – schematic positive displacement blood pump.

An actuation system is needed to compress the sac or push the membrane towards the housing and thus achieve ejection.

Pneumatic actuation is the simplest mechanism: the sac or membrane is compressed by pressurized air during ejection; this air flows back out of the pump during the filling phase. Typical example of such kind of device is the EXCOR® (BerlinHeart GmbH, Berlin, Germany), see Figure 1.26.

a air chamber

b driving tube connector

c triple-layer membrane

d blood chamber (de-airing nipple at back of pump)

e arrow mark: indicates blood flow direction

f inflow stub

g outflow stub

h titanium connector: outflow stub – outflow cannula

i titanium connector: inflow stub – inflow cannula
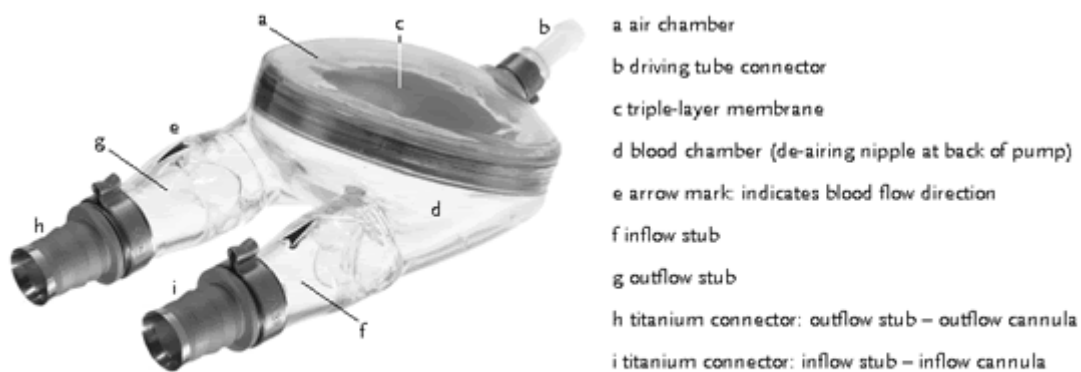
60 ml blood pump, here with polyurethane leaflet valves

Figure 1.26 – EXCOR® from BerlinHeart, pneumatically actuated positive displacement blood pump[2].

Electromechanical actuation is usually built around a DC motor, whose rotational movement is mechanically transformed into a linear movement that actuates a plate that pushes the membrane. An example of such kind of device is the HeartMate® LVAD (Thoratec Corporation, Pleasanton, CA, USA), see Figure 1.27.

---

[2] http://www.berlinheart.de/englisch/medpro/EXCOR/pumpen/. Accessed November 15, 2007
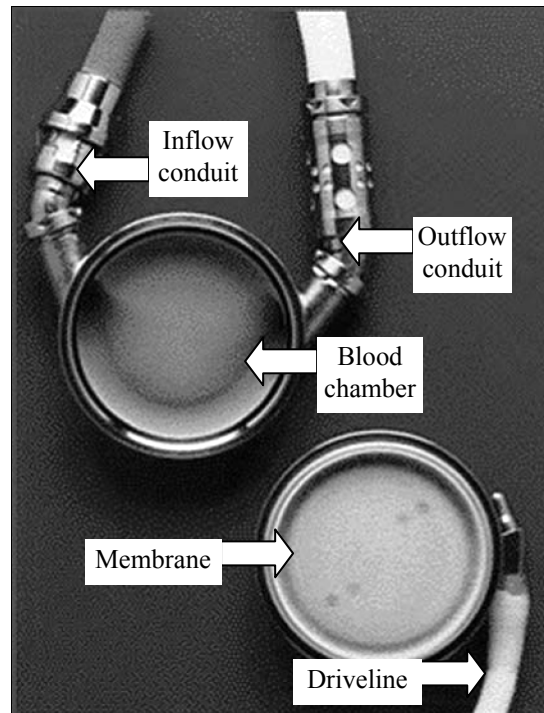
Figure 1.27 – HeartMate® form Thoratec, electromechanical actuated positive displacement blood pump (Zipes et al., 2004, p. 632).

The bigger advantage of positive displacement pumps is the generation of pulsatile blood flow, which is a condition more similar to the native heart blood flow. Furthermore their pumping action is almost afterload insensitive and they could deliver up to about 10 L/min of blood to the patient. Among the disadvantages we have the quite big dimensions, a drawback for implantable devices, they require valves, complex driving mechanisms and they are in general expensive devices.

Rotary pumps

Rotary pumps have an impeller that spins around at high speed and transfers energy to the blood by velocity changes along the impeller radius. The impeller is usually composed of a disc or cone with vanes, but there are also vaneless alternatives. The rotary pumps can be further divided into radial (centrifugal), axial and diagonal rotary pumps (Figure 1.28).

CENTRIFUGAL   DIAGONAL   AXIAL
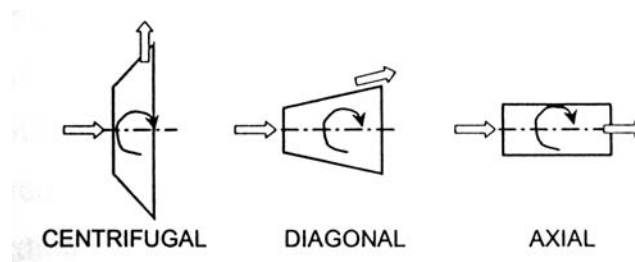
Figure 1.28 – rotary pumps.

Centrifugal pumps have the inflow path that is parallel to the rotation axis while the outflow path is orthogonal to it. An example of such kind of

device is the HVAD[TM] (HeartWare, Sydney, Australia). Diagonal pumps have an inflow that is parallel to the rotational axis, but the outflow is diagonal to that axis. An example of such kind of device is the DELTA*STREAM*[®] (Medos Medizintechnik, Stolberg, Germany). Finally axial pumps have both inflow and outflow parallel to the rotational axis. An example of such kind of device is the DeBakey VAD[®] (MicroMed Cardiovascular, Huston, TX, USA). See Figure 1.29 for pictures of the abovementioned devices.

<div align="center">(a)   (b)   (c)</div>
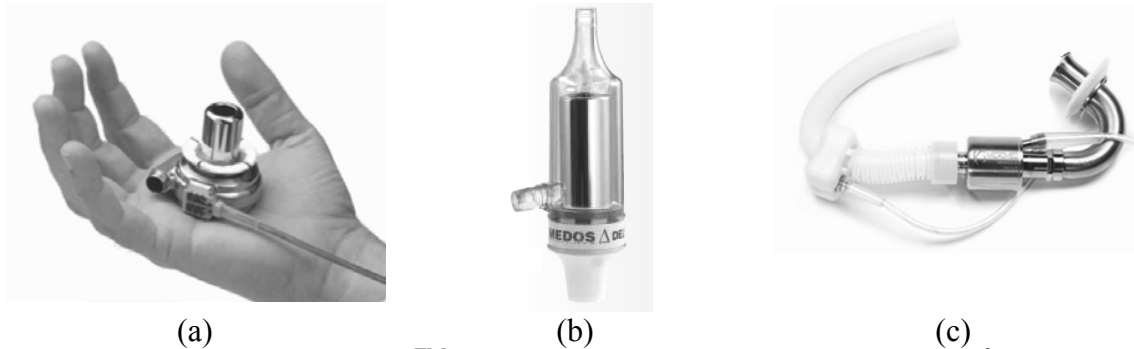
Figure 1.29 – (a) HVAD[TM] form HeartWare, centrifugal blood pump[3]; (b) DELTA*STREAM*[®] from Medos, diagonal blood pump[4]; (c) DeBakey VAD[®] from MicroMed Cardiovascular, axial blood pump[5].

Each design results in a different pump characteristics and, generally speaking, centrifugal pumps are capable of producing higher pressure at lower flows, whereas axial pumps typically generate higher flows at lower pressure rises (Song et al., 2003).

Rotary pumps have several advantages: they have only one moving part (the impeller), they do not need valves, the are very small and compact, silent and suited for mass production at low cost. However they deliver continuous flow, they need complex physiologic control strategies and there may be wear and heat problems at the bearings (in those devices that does not have magnetic suspension or hydrodynamic bearing for the impeller).

Several studies have demonstrated that pulsatile flow was not critical to maintaining the integrity of the pulmonary or systemic circulation and organ function, whereas other experiments have suggested evidence to the contrary (Allen et al., 1997). The implication of continuous flow condition remain unclear to the medical community, and additional research may provide insight into design consideration for both positive displacement and rotary blood pumps.

---

[3] http://www.heartware.com.au/IRM/content/europe/home.html. Accessed November 15, 2007
[4] Bro_DELTASTREAM_112005_DE.pdf in http://www.medos-ag.com/deltastream_de.html. Accessed November 15, 2007
[5] http://www.micromedtech.com/products2.html. Accessed November 15, 2007

Chapter 2

A numerical model of the cardiovascular system.

The numerical model of the human cardiovascular system is presented in its compartments. First a brief review of history in cardiovascular modeling and of model already available in literature is presented. Then a detailed description of the implemented model is presented: the heart model, comprising both ventricles and atria; the vascular tree, comprising both the systemic and pulmonary circulations, autoregulatory mechanisms. The model validation, using literature data, is then presented.

1 Introduction

Along with the experimental approach, mathematical modeling has become a popular way to study the cardiovascular system. Of several modeling approaches, the lumped parameter model is broadly used to analyze the hemodynamics of the cardiovascular system. The hemodynamics can be represented by the relationship between blood pressure and blood flow in compartments of the cardiovascular system (e.g. heart, arterial tree, venous system etc.). Electric analogs are widely used for physical modeling (Beranek, 1996, p. 51). Pressure and flow are analog to voltage and current, respectively. Resistance to blood flow is analog to electric resistance, vascular compliance to capacitance and inertia for blood acceleration to inductance. Electric analog and mathematical modeling has been recognized since the sixties as a useful tool for analyzing cardiovascular system physiology and, in general, bio-engineering problems (Arabia et al., 1966).

Many mathematical models of the cardiovascular system have been published since Grodins made the first global dynamic model of one in 1959 (Grodins, 1959). Guyton's system analysis of circulatory regulation (Guyton et al., 1972) was performed with a complex model which comprised of 354 blocks, each representing one or more mathematical equations describing some physiological facet of circulatory function. In general, each of the functional blocks has been the subject of research investigation by one or many investigators. Some other modeling studies dedicated to characterizing certain causal relationships between circulatory variables and hemodynamic consequences using mathematical models were conducted by (Beyar et al., 1987, Maughan et al., 1987, Santamore and Burkhoff, 1991). Based on these works, a significant improvement was made by (Sun et al., 1997) who constructed an elaborated right–left heart interaction mathematical model capable of predicting cardiac hemodynamics for not only normal but also various pathological conditions. For ventricular modeling a considerable step forward was done by (Campbell et al., 1982a, Campbell et al., 1982b) that developed the so-called time-varying elastance model, as proposed by (Sunagawa and Sagawa, 1982). More recent works integrate models at different scales, e.g. from cells to system (Shim et al., 2006) or computational fluid dynamics models with lumped parameter models (Liang et al., 2007).

A numerical model of the cardiovascular dynamics was implemented using the Matlab®-Simulink® computing language. The circulatory system was modeled as a closed hydraulic circuit comprising left and right ventricle, modeled by nonlinear time-varying elastances and internal resistance, active left and right atrium, systemic and pulmonary arterial load, and systemic and pulmonary venous return. Using the huge amount of literature data nowadays available, the model was accurately built in each

single compartment. Because most of the literature results are in a graphic form (signal waveforms, various plots), a program which extracts numerical coordinates from pictures was written using Matlab®. The so obtained "numbers" are suited for further elaboration and information extraction. Model was then validated by comparing with available literature the cardiac functions and the left ventricular PV loop behavior with respect to preload and afterload variations.

2 Model Implementation

First the heart model is presented with both ventricles and atria. Particular attention is paid into the left ventricle model, having the right ventricle and the atria essentially the same structure with just different parameters. Second arterial networks, both systemic and pulmonary are presented, followed by venous returns (systemic and pulmonary). Finally autoregulatory mechanisms are presented.

2.1 Heart

Cardiac chambers (ventricles and atria) are modeled by nonlinear time-varying elastances and internal resistance (Campbell et al., 1982a). Equation (2.1) represents the mathematical relation between blood pressure and volume inside the chamber.

$$P(t) = \varphi[V(t), t] - R_i \cdot \frac{dV(t)}{dt} \tag{2.1}$$

Where t represents the time, $V(t)$ the instantaneous blood volume inside the chamber, $P(t)$ the instantaneous blood pressure inside the chamber, R_i the internal resistance. The internal resistance term is not present in the atrial models. It takes into account the internal ventricular dissipation of energy during ejection and the values for both the ventricles were set dependent on the pressure developed into the ventricle according to (Ursino, 1998). The $\varphi[V(t),t]$ function represents the non-linear time-varying elastance. The instantaneous ventricular elastance, $E(t)$, is the slope of the function $\varphi[V(t),t]$ at the time t and volume $V(t)$. The mathematical relation for the $\varphi[V(t),t]$ function is:

$$\varphi[V(t), t] = \varphi_p[V(t)] + \varphi_a[V(t)] \cdot F_{iso}(t) \tag{2.2}$$

where $F_{iso}(t)$ represents the ventricular contraction function normalized with respect to cardiac cycle duration (T) and amplitude (E_{max}).

Let φ_p and φ_a be the passive and active pressure volume pump relationships, respectively. Being φ_p also the end-diastolic pressure-volume relation (EDPVR) and $\varphi_p + \varphi_a$ the end-systolic pressure-volume relation (ESPVR). The function φ_p is realized by means of a straight line for both atria, a power function ($\varphi_p = a*V^b$) for the left ventricle, an hyperbole for the right ventricle. The function φ_a is modeled, in all cases, by using a

parabolic relation (Burkhoff et al., 1987), equation (2.3). This relation is characterized by downward concavity, vertex having coordinates (V^*, P^*), and passing through the point with coordinates (V_d, 0), where V_d is the so-called ventricular dead volume.

$$\varphi_a[V(t)] = \left[1 - \left(\frac{V^* - V(t)}{V^* - V_d} \right)^2 \right] \cdot P^* \qquad (2.3)$$

Here (V^*, P^*) are used to locate the ESPVR in the PV plane and thus obtain different contractility levels for the ventricles and atria.

Left ventricle

To particularize equation (2.2) in order to obtain the model for the left ventricle, first the used $F_{iso}(t)$ will be introduced and then the φ_p function.

(Senzaki et al., 1996) derived a normalized time-varying elastance curve. Pressure-volume data from 3 to 5 sequential steady-state beats were signal-averaged to yield a PV loop. Time-varying elastance $E(t)$ was defined as the instantaneous ratio of ventricular pressure and volume. The curve was normalized, $E_N(t_N)$, with respect to the maximal value of elastance E_{max} and the time to achieve E_{max}. The mean $E_N(t_N)$ curve (Figure 2.1) was the average of data from 72 randomly selected loops from 52 patients (12 normal, 12 hypertrophic cardiomyopathy, 9 dilated cardiomyopathy, 12 coronary artery disease, and 7 ventricular aneurysm), with several patients providing more than one condition (i.e. altered heart rate or contractility).
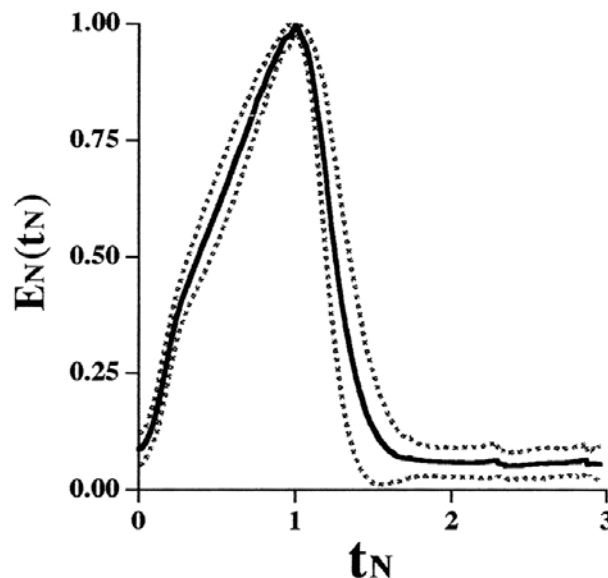
Figure 2.1 – averaged normalized elastance curve $E_N(t_N)$; solid line shows mean and dotted lines ±1 standard deviation (Senzaki et al., 1996).

There is a relatively little variance about the mean for each $E_N(t_N)$ curve among the groups. Furthermore, the mean $E_N(t_N)$ curves were quite similar

between groups despite marked differences in disease condition, afterload, preload, and contractility. It can be therefore concluded that the normalized elastance function is quite insensitive to working condition or ventricular health state.

The solid line of Figure 2.1 was imported in Matlab®, the ordinate scale was re-normalized to have values ranging from 0 to 1. It was then possible to choose three cubic functions that approximated the curve for time t between *0* and *Tsys* (see Figure 2.2). In particular a first cubic function for t between *0* and *Xrise*, a second one between *Xrise* and *Trise* and a third one between *Trise* and *Tsys*. The function for t between *Tsys* and *T* was *0*.
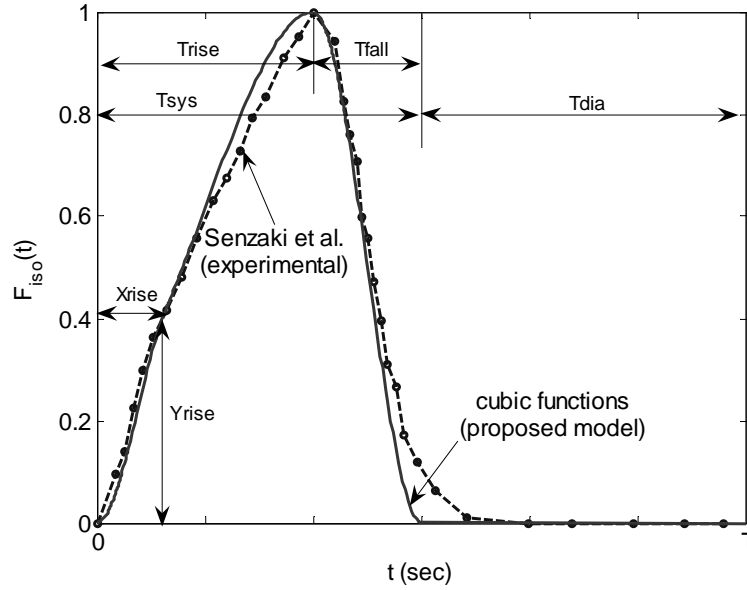
Figure 2.2 – dashed: normalized elastance curve imported from (Senzaki et al., 1996); solid: piecewise cubic functions used for the model.

The ratio between *Tsys* and *Tdia* was heart rate (*HR*) dependent according to (Vollkron et al., 2002), in particular the mathematical form for *Tdia* is:

$$Tdia = \frac{1}{2} \cdot \left[e^{-0.01207 \cdot (HR-40)} + e^{-0.038 \cdot (HR-40)} \right] \tag{2.4}$$

Trise was set equal to 2/3 of *Tsys*, whereas *Xrise* and *Yrise* were set to *0.32*Trise* and *0.42*, respectively. All the parameters can be modified thus allowing to simulate different conditions like impaired ventricular relaxation (increased *Tfall*) or inotropic stimulation (higher *Yrise*).

The $F_{iso}(t)$ can be then expressed into mathematical form:

$$F_{iso}(t) = \begin{cases} a_{13} \cdot t^3 + a_{12} \cdot t^2 & 0 < t < Xrise \\ a_{23} \cdot t^3 + a_{22} \cdot t^2 + a_{21} \cdot t + a_{20} & Xrise < t < Trise \\ a_{33} \cdot t^3 + a_{32} \cdot t^2 + a_{31} \cdot t + a_{30} & Trise < t < Tsys \\ 0 & Tsys < t < T \end{cases} \tag{2.5}$$

where the coefficients a_{ij} are so calculated:

39

$$a_{13} = \frac{-2 \cdot Yrise + Xrise \cdot slope}{Xrise^3}$$

$$a_{12} = -\frac{-3 \cdot Yrise + Xrise \cdot slope}{Xrise^2}$$

$$a_{23} = \frac{-2 \cdot Yrise + Xrise \cdot slope + 2 - Trise \cdot slope}{Xrise^3 + 3 \cdot Xrise \cdot Trise^2 - Trise^3 - 3 \cdot Trise \cdot Xrise^2}$$

$$a_{22} = -\frac{slope \cdot Xrise^2 - 3 \cdot Xrise \cdot Yrise + 3 \cdot Xrise + Xrise \cdot Trise \cdot slope - 2 \cdot Trise^2 \cdot slope - 3 \cdot Trise \cdot Yrise + 3 \cdot Trise}{Xrise^3 + 3 \cdot Xrise \cdot Trise^2 - Trise^3 - 3 \cdot Trise \cdot Xrise^2}$$

$$a_{21} = \frac{Trise \cdot \left(-Xrise \cdot Trise \cdot slope + Trise^2 \cdot slope + 2 \cdot slope \cdot Xrise^2 - 6 \cdot Xrise \cdot Yrise + 6 \cdot Xrise\right)}{Xrise^3 + 3 \cdot Xrise \cdot Trise^2 - Trise^3 - 3 \cdot Trise \cdot Xrise^2}$$

$$a_{20} = \frac{Xrise^3 - 3 \cdot Trise \cdot Xrise^2 - Trise^3 \cdot Yrise + Trise^3 \cdot Xrise \cdot slope - Trise^2 \cdot slope \cdot Xrise^2 + 3 \cdot Trise^2 \cdot Xrise \cdot Yrise}{Xrise^3 + 3 \cdot Xrise \cdot Trise^2 - Trise^3 - 3 \cdot Trise \cdot Xrise^2}$$ (2.6)

$$a_{33} = \frac{2}{-Trise^3 - 3 \cdot Trise \cdot Tsys^2 + Tsys^3 + 3 \cdot Tsys \cdot Trise^2}$$

$$a_{32} = \frac{3 \cdot (Tsys + Trise)}{-Trise^3 - 3 \cdot Trise \cdot Tsys^2 + Tsys^3 + 3 \cdot Tsys \cdot Trise^2}$$

$$a_{31} = \frac{6 \cdot Trise \cdot Tsys}{-Trise^3 - 3 \cdot Trise \cdot Tsys^2 + Tsys^3 + 3 \cdot Tsys \cdot Trise^2}$$

$$a_{30} = \frac{Tsys^2 \cdot (Tsys - 3 \cdot Trise)}{-Trise^3 - 3 \cdot Trise \cdot Tsys^2 + Tsys^3 + 3 \cdot Tsys \cdot Trise^2}$$

here the parameter *slope* defines the slope of the $F_{iso}(t)$ at the point with coordinates (*Xrise*, *Trise*) and it was set equal to *1/Trise*.

The next element that must be introduced in order to particularize equation (2.2) is the function φ_p. This function represents, in the pressure volume plane, the passive characteristic of the ventricular muscle, the end-diastolic pressure volume relationship (EDPVR). In other words, it defines the stiffness of the ventricle when it is in its relaxed state. This characteristic is very important because it is related to the preload sensitivity of the ventricle itself, i.e. how much blood the ventricle pump will deliver depending on its filling pressure (the atrial pressure or preload pressure).

In a recent paper (Klotz et al., 2006) noted that independent of etiology, when EDPVRs were normalized (EDPVRn) by appropriate scaling of left ventricle volumes, EDPVRns were nearly identical and were optimally described by the relation $EDP = An*EDVn^{Bn}$, with An = 27.78 mmHg and Bn = 2.76 (see Figure 2.3).

The EDPVR of the ventricle model was calculated by forcing the curve through a pressure volume point (V_m, P_m), and volume at 0 mmHg pressure and 30 mmHg pressure (V_0 and V_{30}). In particular V_{30} is calculated from equation (2.7):

$$V_{30} = V_0 + \frac{V_m - V_0}{\left(\dfrac{P_m}{An}\right)^{\frac{1}{Bn}}}$$ (2.7)

The coefficients of the relationship $EDP = \alpha * EDV^{\beta}$ are calculated with the following relations:

$$\alpha = \frac{30}{V_{30}^{\log\left(\frac{P_m}{30}\right) / \log\left(\frac{V_m}{30}\right)}}$$ (2.8)

$$\beta = \frac{\log\left(\dfrac{P_m}{30}\right)}{\log\left(\dfrac{V_m}{30}\right)}$$ (2.9)
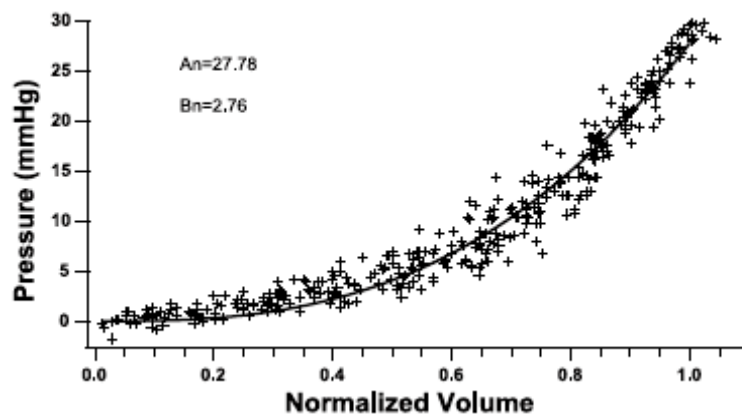
Figure 2.3 – all ex vivo human volume-normalized EDPVR data shown superimposed on each other; *An* and *Bn*, parameter values (Klotz et al., 2006).

When the left ventricular volume is lower than the value V_0 the EDPVR has an inflection and the pressure decreases more rapidly as shown in Figure 2.4.
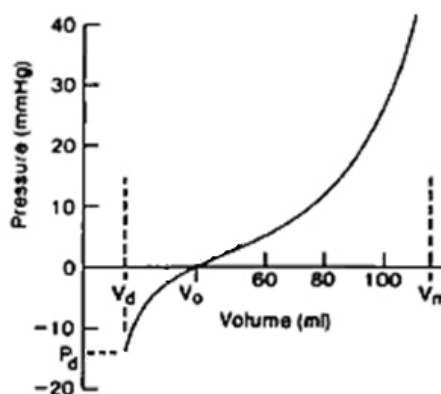
Figure 2.4 – representative plot of a measured ventricular passive pressure-volume relation. V_0 volume at zero transmural pressure; *Vd* and *Pd* minimum volume and pressure, *Vm* maximum volume. Partially modified from (Nikolic et al., 1988).

This part of the EDPVR at negative pressures represents the so-called diastolic suction (Suga et al., 1988). It was modeled by a cubic function

which passes through the points of coordinates (V_d, P_d) and $(V_0, \alpha * V_0^\beta)$, that has an assigned slope in (V_d, P_d), and the slope of the previously calculated EDPVR relation, $EDP = \alpha * EDV^\beta$, in their joining point $(V_0, \alpha * V_0^\beta)$. Used values for P_d, V_d and V_0 where defined according to (Suga et al., 1988).

To complete the model of the φ_p function an offset pressure term P_{offset} was added. In equation (2.10), the complete mathematical representation of the φ_p function is reported.

$$\varphi_p(V) = \begin{cases} \left(c_3 \cdot V^3 + c_2 \cdot V^2 + c_1 \cdot V + c_o\right) + P_{offset} & V_d < V < V_0 \\ \alpha \cdot V^\beta + P_{offset} & V > V_0 \end{cases} \qquad (2.10)$$

Because the parametric expressions of c_3, c_2, c_1 and c_0 are considerably long, they are omitted. A list of the parameter values used to model the left ventricle, both in the physiological and pathological state, is reported in Table 2.1. The parameters for the pathologic left ventricle were chosen in order to mimic a systolic left heart failure of the NYHA (New York Heart Association) class III to IV (Zipes et al., 2004, p. 542). This corresponds to a patient that has already discomfort during slight physical activity or even at rest (Hunt et al., 2001).

Table 2.1: values used for the left ventricle model parameters.

|	physiologic ventricle	pathologic ventricle
HR (bpm)	72	90
$V*$ (mL)	175	300
$P*$ (mmHg)	270	120
LVM (gr) (Zipes et al., 2004, p. 513)	175	300
V_0 (mL) (Suga et al., 1988)	15.8*LVM/100	like physiologic
P_{offset} (mmHg)	2.5	like physiologic
V_d (mL) (Suga et al., 1988)	4.3*LVM/100	like physiologic
P_d (mmHg) (Suga et al., 1988)	-9.5	like physiologic
V_m (mL)	230	250
P_m (mL)	25	like physiologic
$c3$	-0.0011	-4.254e-5
$c2$	0.0454	-0.0034
$c1$	0.0025	0.6089
$c0$	-11.6244	-16.697
α	4.127e-12	2.124e-13
β	5.4122	5.8679
$Ri(t)$ (mmHg*s/mL) (Ursino, 1998)	3.75e-4*$P_{lv}(t)$	like physiologic

Parameters $V*$, $P*$, P_0, V_m and P_m were chosen to reproduce the correct cardiac function curves of the physiologic and pathologic left ventricle (see Figure 2.18 in paragraph 3.1 of this chapter).

PV plane with respective ESPVRs and EDPVRs obtained by the model are plotted in Figure 2.5 both for the physiologic and pathologic modeled left ventricle.
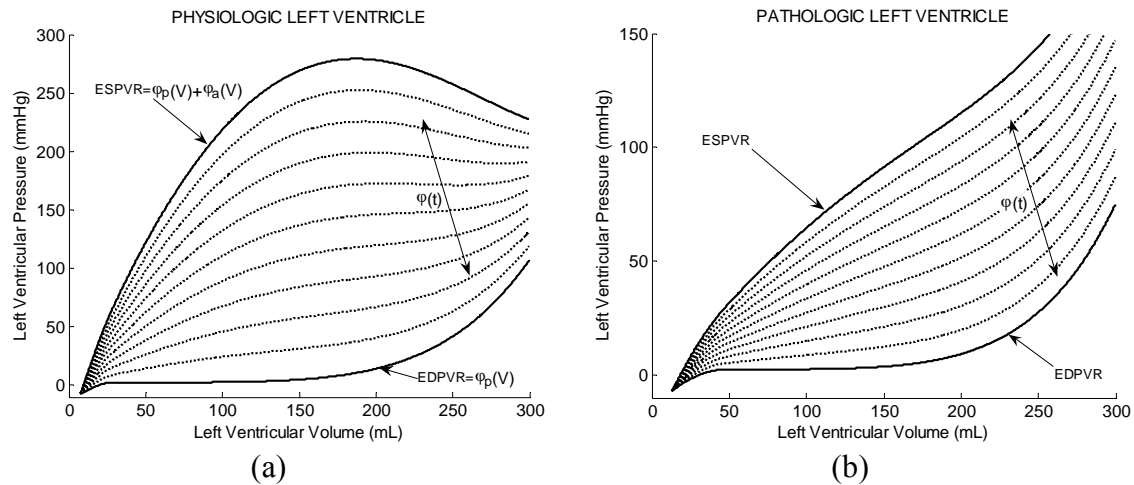
Figure 2.5 – model generated elastance functions $\varphi[V(t),t]$ for the physiologic (a) and pathologic (b) left ventricle.

It is interesting to compare these curves, and in particular their non-linear behavior, with the measured curves of (Burkhoff et al., 1987), reported in Figure 2.6. The model can reproduce the non linearity of the elastance curves and, in particular, the concavity inversion of these curves at different contractility levels.
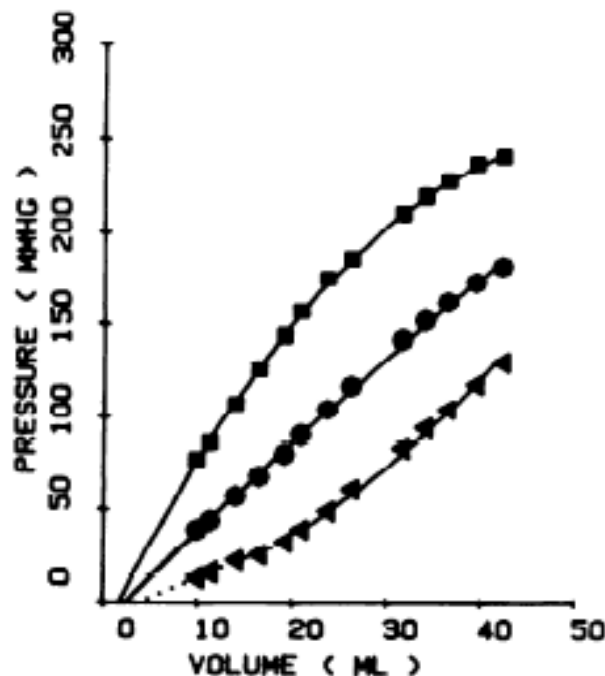
Figure 2.6 – end systolic pressure-volume relation (ESPVR) in an isolated dog heart is reasonably linear for normal level of contractility (●);at higher levels of contractility (■) the ESPVRs become concave to the volume axis, whereas at lower levels of contractility (◄) the curves become convex to the volume axis (Burkhoff et al., 1987).

Right ventricle

The approach used to model the right ventricle was similar to the one used for the left. Apart from different parameter values, equations (2.1), (2.2), (2.3) and (2.5) are valid for the right ventricle as well. The main difference consists into the φ_p function, that was modeled using another method.

Equation (1.14) is the starting point of this other method and it is rewritten in here in (2.11). This equation states that the flow delivered by the right ventricle is essentially a function of the right atrial pressure *Pra*, for a given contractile state (*Kr*) and extracardiac pressure (*Pec*):

$$F = Kr - \frac{a}{Pra - Pec - b} \tag{2.11}$$

here *F* is the total flow (in L/min) delivered by the right ventricle and *a* and *b* constants.

The end diastolic volume (EDV) is equal to the stroke volume (SV) summed to the end systolic volume (ESV). In turn the SV is the flow *F* divided by the heart rate (*HR*), so that we can write this equation:

$$EDV = \frac{1000 \cdot F}{HR} + ESV = \frac{1000 \cdot \left(Kr - \dfrac{a}{Pra - Pec - b} \right)}{HR} + ESV \tag{2.12}$$

here pressures are expressed in mmHg, the volumes in mL, Hr in beats per minute, the flow *F* in L/min. Solving equation (2.12) for *Pra* leads to:

$$Pra = \frac{HR \cdot (Pec + b) \cdot EDV - \left[1000 \cdot Kr \cdot (Pec + b) + 1000 \cdot a + ESV \cdot HR \cdot (Pec + b) \right]}{HR \cdot EDV - (1000 \cdot Kr + ESV \cdot HR)} \tag{2.13}$$

If we reasonably assume that end systolic volume is relatively independent on right atrial pressure, because it is only determined by the ESPVR and the afterload pressure into the pulmonary artery, we can set it equal to 70 mL. Being the end diastolic pressure (EDP) equal to the *Pra* diminished of the pressure drop across the tricuspid valve (*ΔP*). We can write the equation for the φ_p function that relates the end diastolic right ventricular pressures (EDP) to the end diastolic right ventricular volume (EDV):

$$EDP = \frac{HR \cdot (Pec + b) \cdot EDV - \left[1000 \cdot Kr \cdot (Pec + b) + 1000 \cdot a + ESV \cdot HR \cdot (Pec + b) \right]}{HR \cdot EDV - (1000 \cdot Kr + ESV \cdot HR)} - \Delta P \tag{2.14}$$

A list of the parameters values used to model the right ventricle is reported in Table 2.2. V_0 was selected to have, in normal condition, an ejection fraction (EF=SV/EDV) of about 0.54 (Milnor, 1990, p. 36). V^* and P^* were selected to reproduce the correct cardiac function curve of the right ventricle (see Figure 2.18 in paragraph 3.1 of this chapter). PV plane with respective ESPVRs and EDPVRs obtained by the model are plotted in Figure 2.7.

Table 2.2: values used for the right ventricle model parameters.

	physiologic ventricle
HR (bpm)	72
V^* (mL)	200
P^* (mmHg)	80
V_0 (mL) (Milnor, 1990, p. 36)	50
P_0 (mmHg)	0
Pec (mmHg) (Guyton et al., 1963, p. 268)	-4
Kr (Guyton et al., 1963, p. 268)	14
a (Guyton et al., 1963, p. 268)	5.3
b (Guyton et al., 1963, p. 268)	3.3
ΔP (mmHg)	0.4
$Ri(t)$ (mmHg*s/mL) (Ursino, 1998)	$1.4e\text{-}3*P_{rv}(t)$
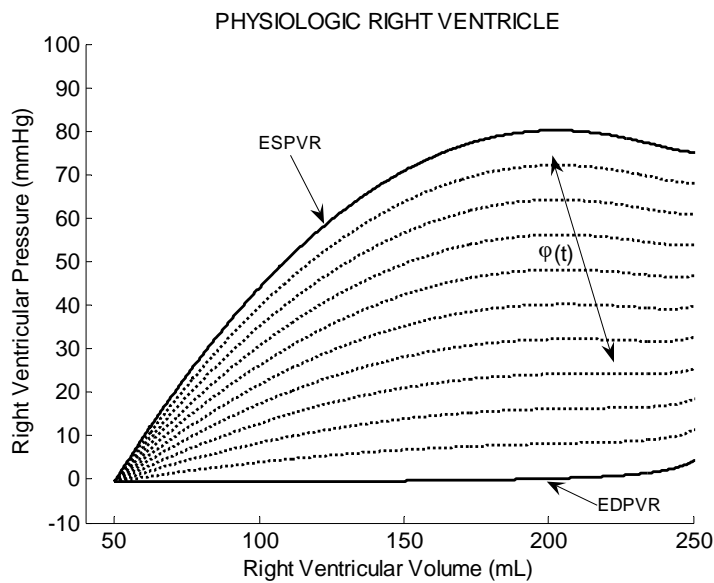
Figure 2.7 – model generated elastance functions $\varphi[V(t),t]$ for the physiologic right ventricle.

Left and right atria

The model for the atrium is substantially the same to that of the ventricle, beside the strength of contraction, lower than the ventricular one. The main differences of atrial model with respect to ventricular ones are two:

The atrial contraction leads the ventricular contraction so that the $F_{iso}(t)$ is anticipated of time span that corresponds to 20% of the heart period. This value was derived from examination of the PR interval in relation with the RR interval of the normal electrocardiogram [figure 9-5 in (Guyton and Hall, 2000, p. 99)]. The P wave in the electrocardiogram indicates the onset of the atrial contraction, whether the R wave the onset of the ventricular one.

The passive characteristic of the atria were selected as simple linear relations passing through the point (V_0, P_0):

$$\varphi_p(V) = (V - V_0) \cdot E\min + P_0 \qquad (2.15)$$

In Table 2.3 parameter values used in the atrial model are shown.

Table 2.3: values used for the atrial models parameters.

	left atrium	right atrium
$F_{iso}(t)$ lead (% of heart period) (Guyton and Hall, 2000, p. 99)	20	20
V^* (mL)	200	200
P^* (mmHg)	30	10
V_0 (mL)	0	0
P_0 (mmHg)	0	-5
$Emin$ (mmHg/mL)	0.125	0.100

Heart valves

Heart valves were modeled as resistors with switching value depending on the flow direction: when the flow is in the forward direction the resistance value is low (R_{dir}) in order to generate the naturally existing pressure gradients, when the flow is in the backward direction resistance is very high (R_{inv}) thus simulating valve closure. An additional inertance term was added (L_v) to simulate the correct LV/RV filling/ejection dynamics. In Figure 2.8 an electric analog model of the valve is shown.
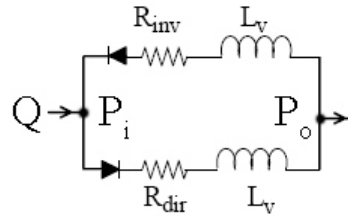
Figure 2.8 – electric analog of the valve model.

The differential equation that describes the valve is the following:

$$P_i - P_o = R_v \cdot Q + L_v \cdot \frac{dQ}{dt} \tag{2.16}$$

where the valve resistance R_v is:

$$R_v = \begin{cases} R_{dir} & Q > 0 \\ R_{inv} & Q < 0 \end{cases} \tag{2.17}$$

To derive the aortic and mitral valves parameter values the following procedure was used: (1) from the normal aortic/mitral valve area and the Gorlin formula mean gradient across the valve was calculated (Zipes et al., 2004, p. 414); (2) mean gradient divided by normal cardiac output gave as result the direct value of valve resistance (R_{dir}); (3) from anatomical considerations and from studies on the LV filling dynamics (Sun et al., 1995) the length of the valve conduit and consequent inertance were determined. Because of lack of information on tricuspid and pulmonary

valve, similar parameter values were used. In Table 2.4 valves parameter values are shown.

Table 2.4: values used for the valve models parameters.

Valve:	Mitral (LA-LV)	Aortic (LV-Ao)	Tricuspid (RA-RV)	Pulmonary (RV-PA)
R_{dir} (mmHg*s/mL)	0.005	0.020	0.003	0.003
R_{inv} (mmHg*s/mL)	50	50	50	50
valve conduit length (cm) (Sun et al., 1995)	2	2	2	2
valve area (cm^2) (Zipes et al., 2004, p. 414)	5.00	3.05	5.00	3.05
Lv=ρ*length/area (mmH*s^2/mL)	3.15e-4	5.16e-4	3.15e-4	5.16e-4

2.2 Arterial load

The arterial systemic and pulmonary arterial loads are modeled by a five-component model (Toy et al., 1985), that is an evolution of the simple *Windkessel* model developed by Otto Frank in 1899 (Frank, 1899, Sagawa et al., 1990).

An electric analog schema of the used model is shown in Figure 2.9.
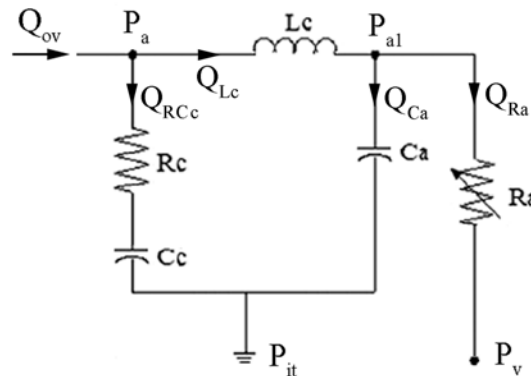
Figure 2.9 – electric analog of the arterial load model.

The differential equations that rule the physics of the system are the following:

$$Q_{ov} - Q_{Lc} = Cc \cdot \frac{d(P_a - R_{Rc} \cdot Q_{RCc})}{dt} \tag{2.18}$$

$$P_a - P_{a1} = Lc \cdot \frac{dQ_{Lc}}{dt} \tag{2.19}$$

$$Q_{Lc} - Q_{Ra} = Ca \cdot \frac{dP_{a1}}{dt} \tag{2.20}$$

$$P_{a1} - P_v = Ra \cdot Q_{Ra} \tag{2.21}$$

here the subscripts *s* or *p* were dropped to make the equations applicable both to systemic and pulmonary arterial load; Q_{ov} is the outflow of either

the left or right ventricle, P_a is either the aortic or pulmonary artery pressure, P_v is either the systemic or pulmonary venous pressure, P_{it} is intratoracic pressure and it is set to be 0 mmHg, Rc, Lc and Cc are the resistance, inertance and compliance characteristics describing either the aorta or the pulmonary artery, Ra and Ca and are the resistance and compliance respectively of the systemic or pulmonary arterial system. The Ra is variable due to autoregulatory mechanisms, this explains the symbol in Figure 2.9.

The parameter values were derived using to the following procedure: (1) the arterial resistance Ra values were determined as described by (Guyton and Hall, 2000, p. 149); (2) the compliance $Ca+Cc$ of the systemic circulation was determined as the slope in the arterial pressure volume curve in Fig. 15-1 of (Guyton and Hall, 2000, p. 153); the $Ca+Cc$ of the pulmonary circulation was chosen to mach the peak to peak pressure pulse in the pulmonary arterial reported in (Guyton and Hall, 2000, p. 145) (3) the other parameter were determined by comparison of the measured input arterial impedances [see figure 7.7B in (Milnor, 1989, p. 182) and figure 11.4 in (Milnor, 1990, p. 370) also reported in Figures 1.13b and 1.14 of chapter 1] and the model generated ones (Figure 2.10). In Table 2.5 the parameter values are shown.
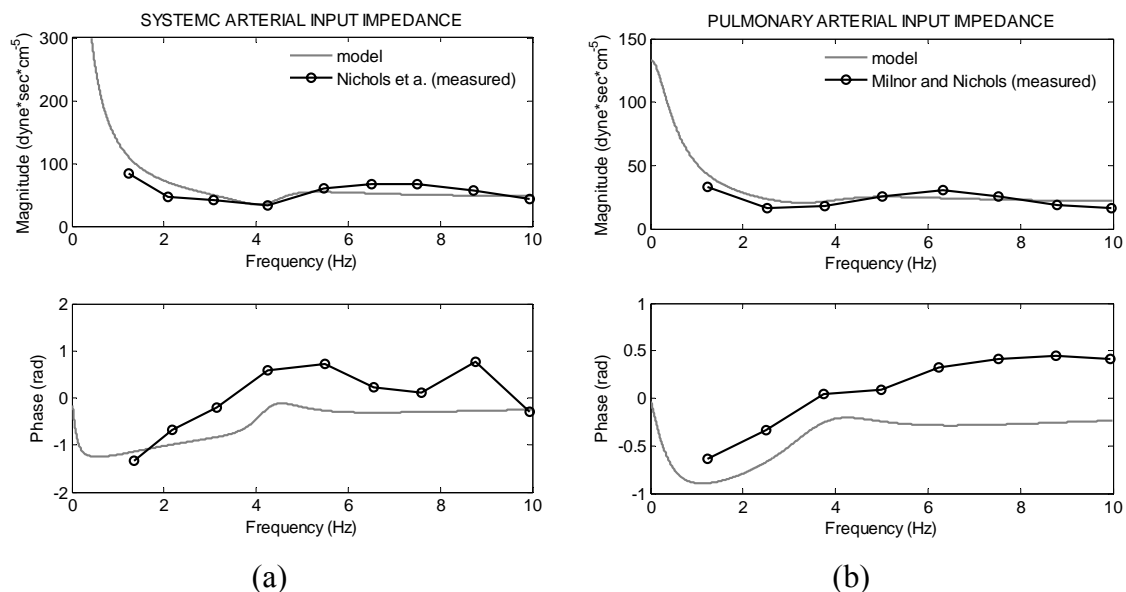
Figure 2.10 – comparison of measured [(Milnor, 1989, p. 182) and (Milnor, 1990, p. 370)] and modeled normal arterial input impedances for the systemic (a) and the pulmonary (b) circulation.

Complex phenomena of wave reflection that are present in the arterial system (because there is a mismatching of impedances of the branching system) cannot be reproduced by simple lumped-parameter models (Milnor, 1989, p. 102). This fact mainly determines the discrepancies in the phase plots of the arterial impedances of Figure 2.10. The use of so-called

transmission line models (Taylor 1959) or even more elaborate models (Womerseley, 1958) improves this aspect.

The shape and amplitude of normal pressure pulses in large arteries vary mainly because of changing vascular parameters, that are closely related with age (Milnor, 1990, p. 47). Parameters which determine normal and hypertensive behavior of the systemic circulation are both reported in Table 2.5. Essentially there is an increase of the arterial resistance (*Ra*) together with a stiffening of the relative compliance (*Ca*). The parameters chosen for the hypertensive behavior determine a stage 2 hypertension according to the classification reported in (Zipes et al., 2004, p. 962). Waveforms for both the normal and hypertensive aortic pressure are shown in Figure 2.11b. They were generated by feeding into the arterial model (Figure 2.9 with parameters in Table 2.5) the left ventricular flow shown in Figure 2.11a. This flow was imported in Matlab® by digitalizing the measured waveform available in (Milnor, 1990, p. 112). The same applies to the pulmonary circulation (Figure 2.11c and Figure 2.11d).
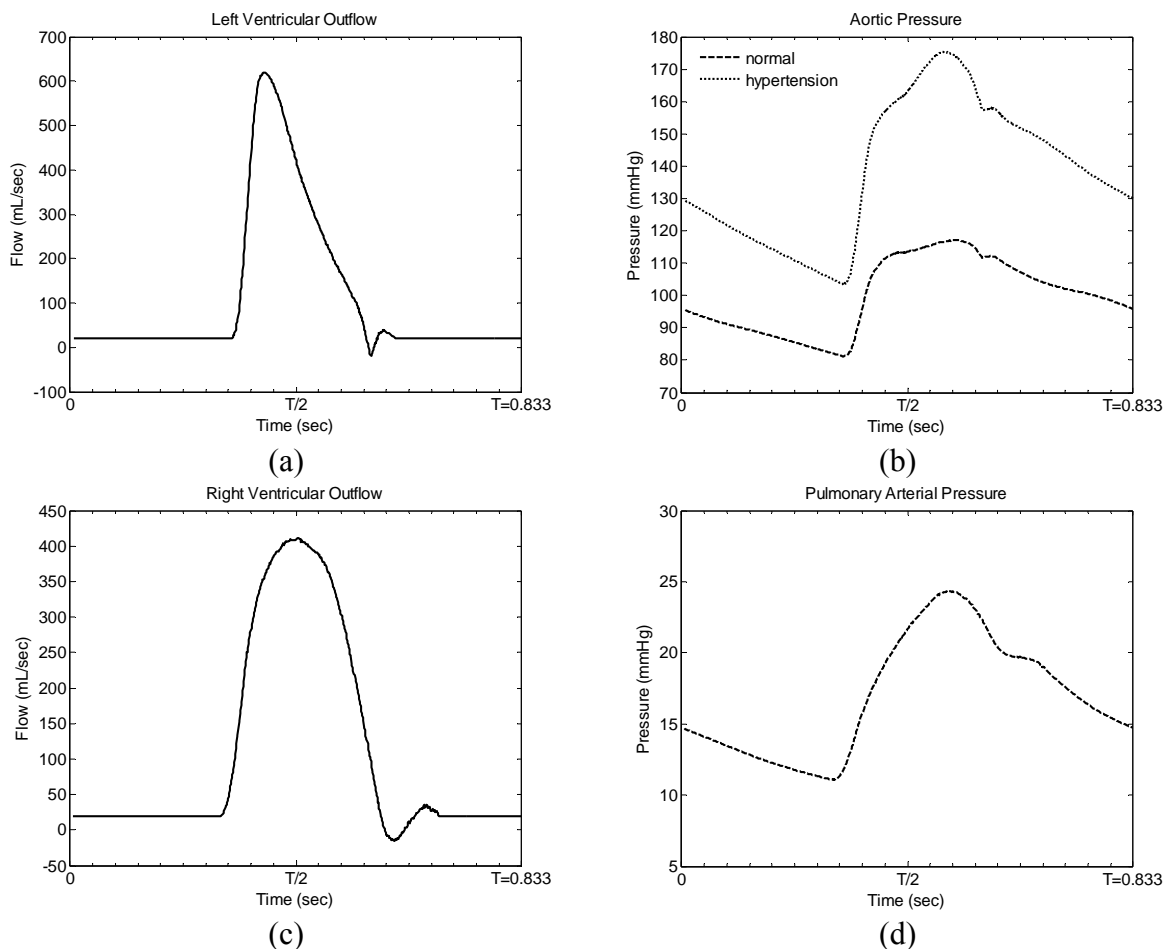
Figure 2.11 – (a) left ventricular outflow from (Milnor, 1990, p. 112); (b) aortic pressure for the normal and hypertensive conditions as calculated from the model; (c) right ventricular outflow from (Milnor, 1990, p. 112); (d) pulmonary arterial pressure as calculated from the model.

Table 2.5: values used for the arterial load parameters.

	systemic		pulmonary
	normal	hypertension	
Rc (mmHg*s/mL)	0.0333	0.0666	0.015
Cc (mL/mmHg) (Guyton and Hall, 2000, pp. 153 and 145)	1.445	0.7225	3.0
Lc (mmH*s^2/mL)	0.0093	0.0093	0.0027
Ca (mL/mmHg) (Guyton and Hall, 2000, pp. 153 and 145)	0.155	0.1033	0.7
Ra (mmHg*s/mL) (Guyton and Hall, 2000, p. 149)	1.066	1.492	0.11

2.3 Venous returns

The systemic and pulmonary venous returns are modeled according to (Guyton et al., 1972). An electric analog schema of the model for the systemic circulation is shown in Figure 2.12. The pulmonary venous return has the same structure, but does not have the control mechanisms on the resistance and compliance of the vessels (denoted by arrows on the circuit components Rvs and Cvs).
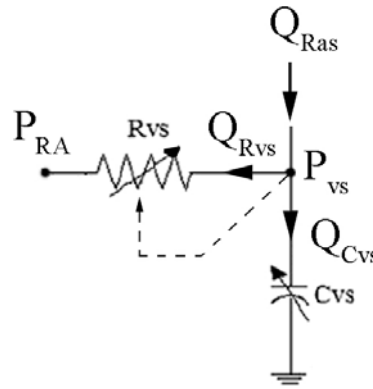
Figure 2.12 – electric analog of the systemic venous return model.

The differential equations that rule the physics of the system are the following:

$$\int (Q_{Ras} - Q_{Rvs})dt = EVs = V - Vvso \tag{2.22}$$

$$P_{vs} = \frac{V - Vvso}{Cvs} \tag{2.23}$$

$$P_{vs} - P_{RA} = Rvs \cdot Q_{Rvs} \tag{2.24}$$

here the subscripts s means that the equations apply to systemic venous returns. For the pulmonary venous return equations are the same. EVs is the blood extra-volume that stretches the compliance, $Vvso$ is the rest volume which is controlled by autoregulatory mechanisms (see next paragraph); V is the total blood volume in the venous vessels.

The systemic compliance parameter value (Cvs) and compliance unstressed volume ($Vvso$) were determined as the slope and intercept in the arterial pressure-volume curve in Fig. 15-1 of (Guyton and Hall, 2000, p.

153). The *Rvs* is dependent of the pressure in the venous systemic vessels *Pvs*, and calculated with the following equation from (Guyton et al., 1972).

$$Rvs = \frac{0.164}{P_{vs}}$$ (2.25)

This equation states that the resistance to the venous return increases when the pressure in the veins decreases. This finding is supported by experimental studies from (Guyton et al., 1955) that demonstrated, given a constant right atrial pressure, the cardiac output does not varies linearly with mean circulatory filling pressure, a pressure that is very closely related to the P_{vs}. (Figure 2.13).
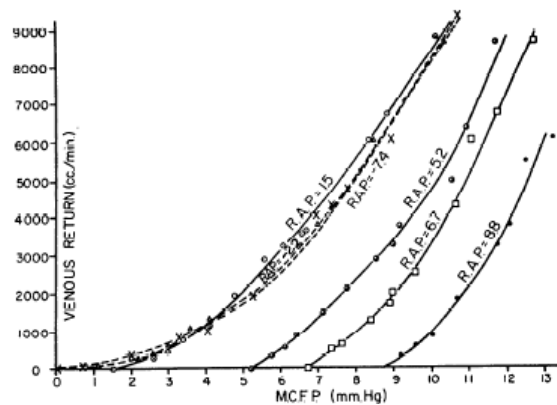
Figure 2.13 – relationship of mean circulatory filling pressure (MCFP) to venous return at different right atrial pressures (RAP) as determined in a dog with a pump replacing the heart (Guyton et al., 1955).

In Figure 2.13 the inverse of the slope of the curves is the resistance to venous return which is very closely related to the systemic venous resistance (*Rvs*).

Table 2.6: values used for the venous return parameters.

	systemic	pulmonary
Rv (mmHg*s/mL) (Guyton et al., 1972)	see equation (2.25)	0.01
Cv (mL/mmHg) (Guyton and Hall, 2000, p. 153)	50	10
Vso (mL) (Guyton and Hall, 2000)	2200	200

2.4 Autoregulatory mechanisms

The intrinsic and basic mechanisms of cardiac output regulation are further adjusted by other factors that adapt the cardiovascular parameters to physiological needs under a wide variety of external conditions. As Guyton observes "the effect of these other factors is *in addition to, rather than instead of,* the basic intrinsic mechanism" (Guyton et al., 1973, p. 494).

Among these other factors we can find short-term (whose action occurs in a time span of seconds to minutes) and long-term (hours to day) regulation mechanisms. The short-term cardiovascular regulation include several mechanisms like arterial pressure, unstressed venous volume, heart

rate and heart contraction force controls. Among them the first two controls were included into the model according to (Ursino, 1998, Ursino et al., 1996, Ursino and Magosso, 2002). Long-term regulation mechanisms were not included into the model.

The first mechanism is the major determinant of the arterial systemic pressure regulation. It is the arterial systemic resistance (*Ras*) control. This mechanism has a first order dynamics with *gain* = –0.01 (mmHg*s/mL)/mmHg, and *time constant* = 1 sec. The difference between mean aortic pressure set point value, 100 mm Hg, and the continuously measured mean aortic pressure is fed into the aforementioned first order system. The output is then summed to the initial *Ras* thus determining the adjusted *Ras* value. This value together with the systemic venous resistance (*Rvs*), determines the slope of the systemic venous return curve (Figure 1.16).

The second autoregulatory mechanism mainly determines the cardiac output control through the systemic venous pressure control (modifying in turn the preload pressure of the right ventricle). It represents the mechanism that rules the tissue oxygen (and therefore blood) need. In Figure 2.14 it is shown in the pressure volume diagram for the venous systemic compliance (*Cvs*), how a reduction of both the unstressed volume (*Vsvo*) of *Cvs* and the *Cvs* value itself affect the systemic venous pressure. Because the *Cvs* variation has a small influence its modification through autoregulatory control was not considered.
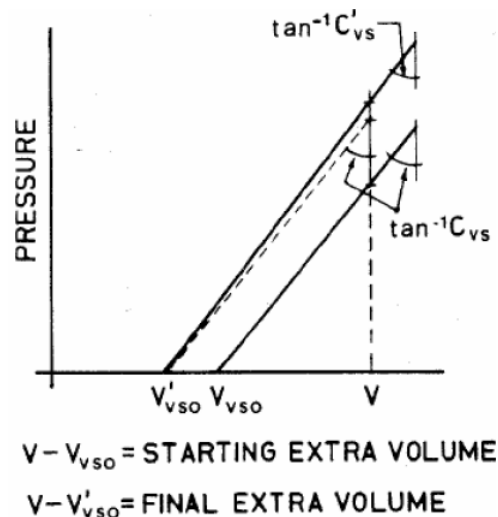
Figure 2.14 – effect of a reduction of systemic venous compliance (*Cvs*) and compliance rest volume (*Vvso*): if the blood volume is *V*, an increase of the systemic venous pressure is obtained (Arabia and Akutsu, 1984).

This control mechanism is provided by first order controller with *gain* = 140 mL/(L/min), and *time constant* = 10 sec. It uses a cardiac output set point, 5 L/min, which is continuously compared with the current mean value of cardiac output. This difference is fed into the aforementioned first

order system, whose output is then summed with the initial unstressed volume, thus determining the adjusted *Vsvo*. When increased oxygen need has to be simulated the CO set point must be increased.

2.5 Waveforms and average hemodynamic values

The electric analog schema of the complete cardiovascular system is shown in Figure 2.15. Two simulations of 50 seconds duration were performed: in the first simulation the implemented model reproduced a physiological behavior; in the second simulation the left ventricle was pathologic in order to mimic a systolic left heart failure of the NYHA (New York Heart Association) class III to IV.
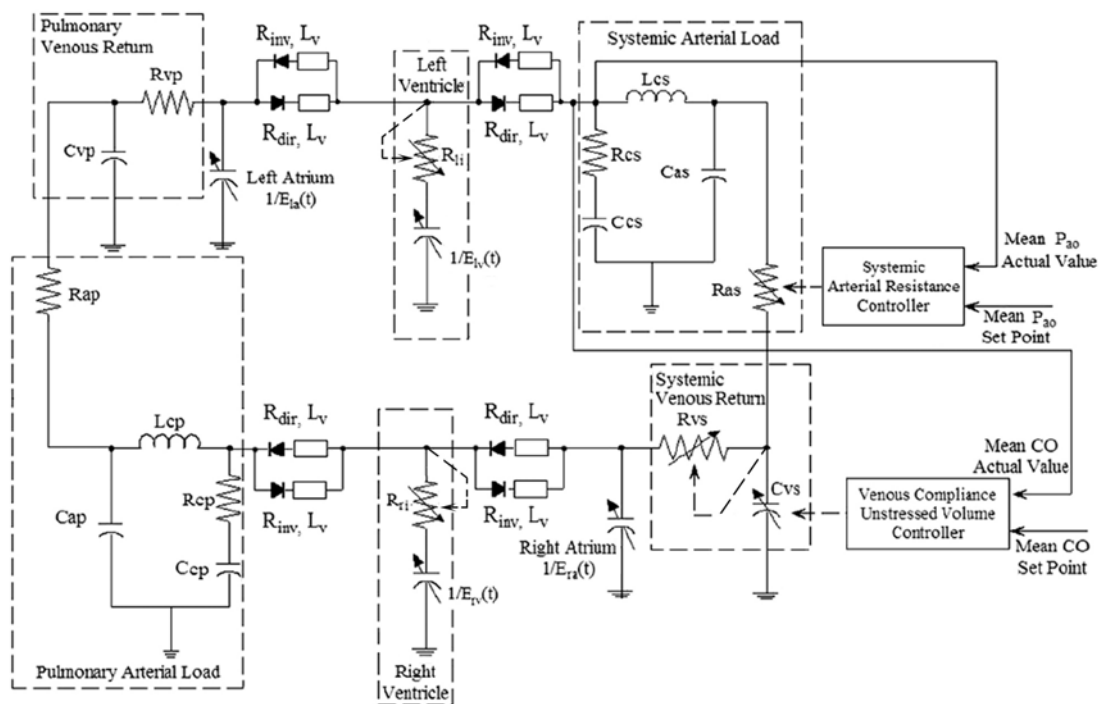
Figure 2.15 – electric analog of the complete cardiovascular model (for symbols see the text).

Figure 2.16 shows the pressure/volume/flow waveforms relative to the left heart both in the physiologic and pathologic condition. In particular waveforms of the ventricular, atrial and aortic pressures; ventricular and atrial volumes as well as inflow and outflow are shown. Figure 2.17 is shows the analogous signals but for the right heart. In Table 2.7 mean values of the hemodynamic parameters relative to both the physiological and pathological condition are presented.

Both the waveforms and the mean values are comparable in a very sufficient way with several measured data from the literature (Guyton and Hall, 2000, Guyton et al., 1963, Milnor, 1989, Milnor, 1990, Sun et al., 1995, Yellin, 1995).

physiologic — pathologic
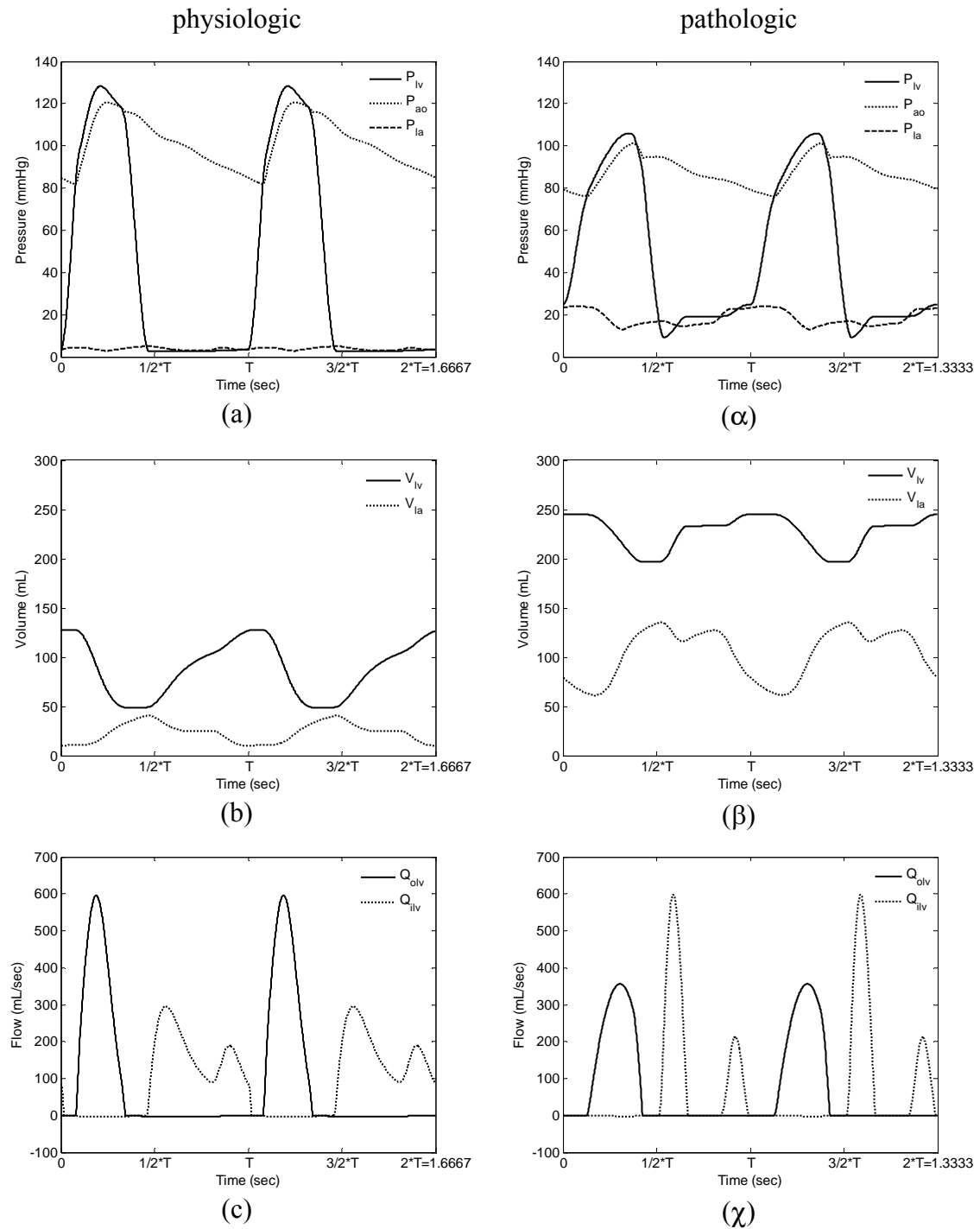
Figure 2.16 – left heart waveforms; on the left column the physiologic condition is simulated, on the right one the pathologic condition is simulated: (a) and (α) pressures in the left ventricle, P_{lv}, aorta, P_{ao}, and left atrium, P_{la}; (b) and (β) left ventricular volume, V_{lv}, and left atrial volume, V_{la}; (c) and (χ) left ventricular outflow, Q_{olv}, and inflow, Q_{ilv}.

physiologic   pathologic
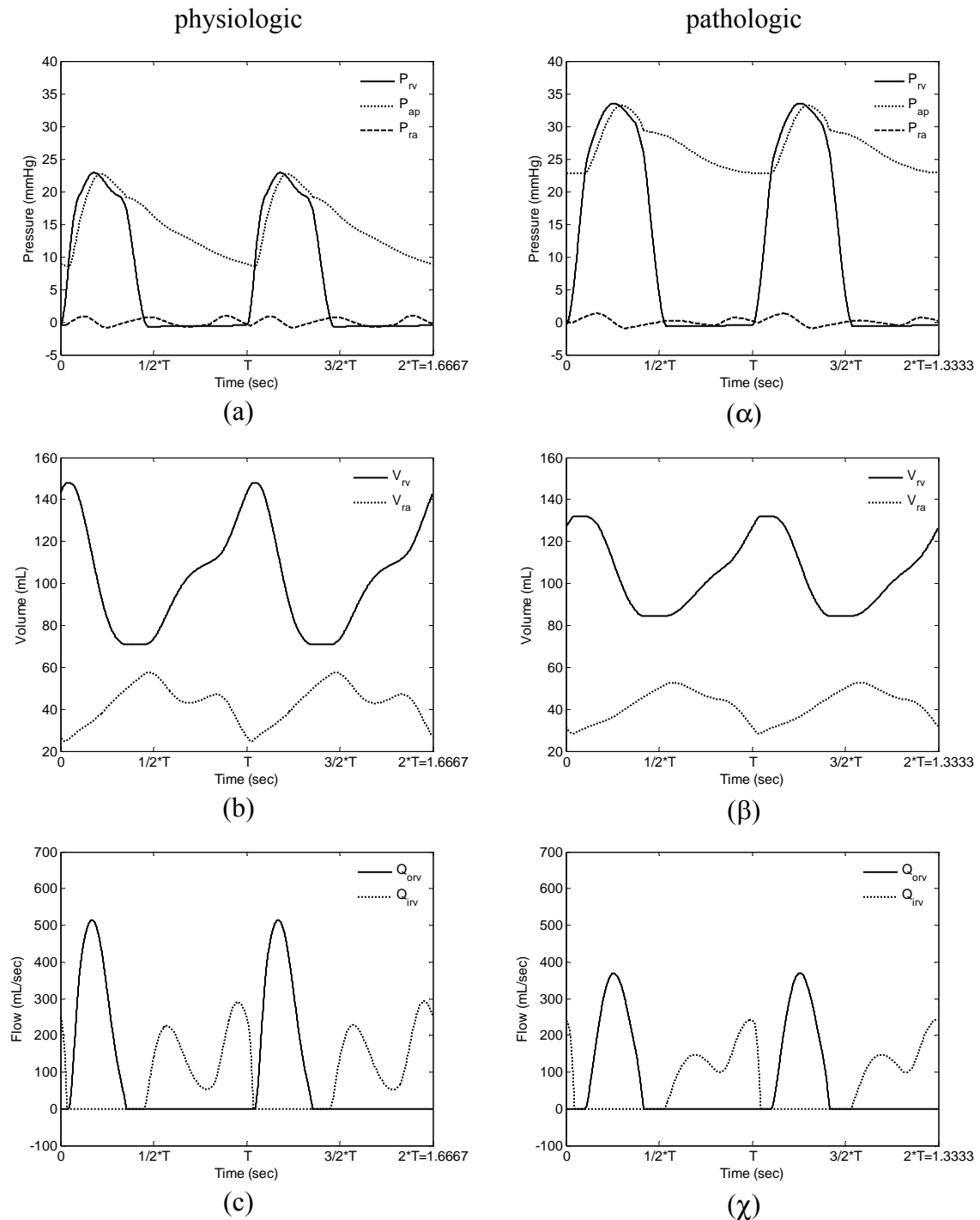
Figure 2.17 – right heart waveforms; n the left column the physiologic condition is simulated, on the right one the pathologic condition is simulated: (a) and (α) pressures in the right ventricle, P_{rv}, pulmonary artery, P_{ap}, and right atrium, P_{ra}; (b) and (β) right ventricular volume, V_{rv}, and right atrial volume, V_{ra}; (c) and (χ) right ventricular outflow, Q_{orv}, and inflow, Q_{irv}.

Table 2.7: values of hemodynamic variables of the cardiovascular model in both physiological and pathological situations.

| hemodynamic variable	physiologic	pathologic	units
CO	5.5	4.2	L/min
HR	72	90	bpm
V_{lv} (min/mean/max)	49/88/126	197/226/244	mL
EF_{lv}	0.61	0.19	-
V_{la} (min/mean/max)	11/23/41	62/104/135	mL
V_{rv} (min/mean/max)	71/103/148	85/105/132	mL
EF_{rv}	0.52	0.36	-
V_{ra} (min/mean/max)	25/42/58	28/42/53	mL
P_{lv} (max)	128	106	mmHg
P_{rv} (max)	23	34	mmHg
P_{ao} (min/mean/max)	82/101/121	76/88/101	mmHg
P_{ap} (min/mean/max)	9/15/23	23/27/33	mmHg
P_{la}	3.8	18.4	mmHg
P_{ra}	0.1	0.1	mmHg
Pmc	7.2	9.4	mmHg
Pms	7.1	6.2	mmHg
Pmp	7.5	21.2	mmHg

3 Model Validation

The model of the whole cardiovascular system was validated in two different but complementary ways.

1. The cardiac functions generated by both ventricle model were compared with those described by equations (1.14) and (1.15) (Guyton et al., 1963, p. 268).
2. The left ventricle pump was validated in the PV plane comparing PV loops with literature data (Sagawa et al., 1988, p. 113). In particular how the PV loop moves in the PV plane as a consequence of both a preload and an afterload variation was considered.

The first validation way allows to determine if the ventricles are correctly modeled to reproduce the average values of flow rate depending on correct average atrial pressure. The second method focuses on the pulsatile components of pressure and volume signals and the classical PV loop theory.

3.1 Cardiac functions

In order to obtain from the model the cardiac functions of both ventricles an ex-vivo situation was simulated. Specifically, with the heart explantend (i.e. not inserted into the torax), the outflow of both ventricles was connected to a reservoir where a constant pressure is held (16 mmHg for the right ventricle and 100 mmHg for the left ventricle); the atrial pressure was increased from –3 mm Hg to 5 mmHg for the right ventricle, from 0 mmHg to 20 mmHg for the left ventricle, both ventricles in a

physiologic condition; and from 2 mmHg to 25 mmHg for a pathologic left ventricle. Mean flow generated at the ventricle outflow each heart beat was recoded and plotted as a function of the correspondent atrial pressure (Figure 2.18). Along with the model results the cardiac functions curves described by equations (1.14) and (1.15) are plotted. The parameter values for these curves were Kr=14 and Kl=16 for the physiologic heart condition and Kl=7 for left ventricular failure; in all cases the extracardiac pressure Pec was –4 mmHg. These curves represent measured data by (Guyton et al., 1963, p. 268).
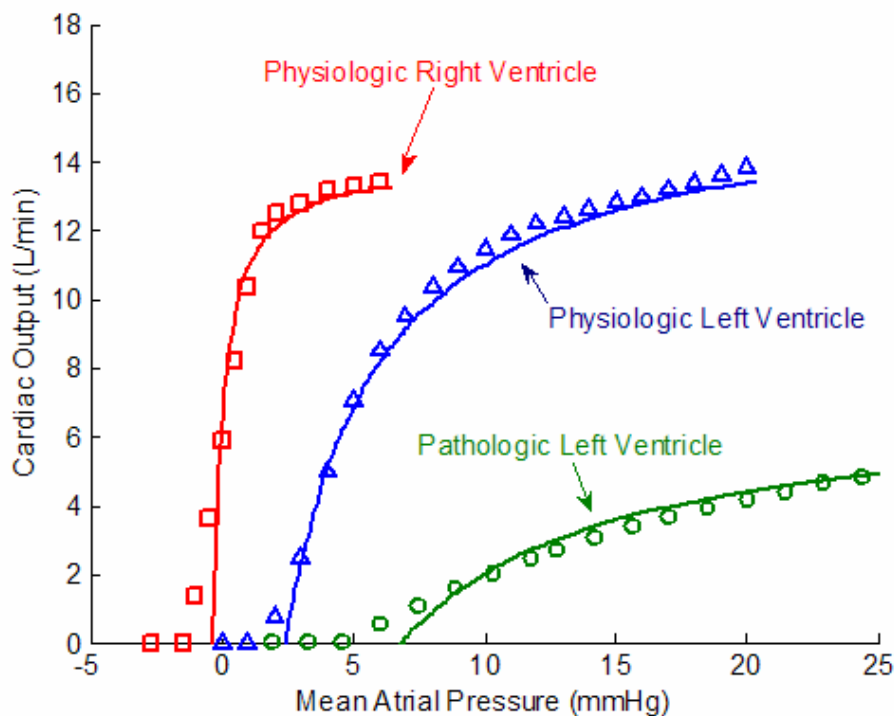
Figure 2.18 – cardiac functions generated by the model are symbolized with (□) for the physiologic right ventricle, (Δ) for the physiologic left ventricle and (O) for the pathologic left ventricle; respective cardiac functions generated by equations (1.14) and (1.15) representing measured data by (Guyton et al., 1963, p. 268) are shown as solid lines.

Figure 2.18 shows how the modeled ventricle pumps behave with the correct preload sensitivity, i.e. the slope of the cardiac function curve. Also the to get a flow of about 5 L/min, pressures must be about 0 mmHg for the right atrium and 4 mmHg for the left atrium, in a physiologic condition. For a pathologic left ventricle its atrial pressure must increase up to 25 mmHg.

3.2 Pressure Volume loops

Preload and afterload effects on the left ventricular PV loop were tested by performing a transient vena cava occlusion and a transient aortic occlusion respectively. The vena cava occlusion was performed on the model by increasing the systemic venous resistance (Rvs) up to a value of

0.4 mmHg*s/mL in 10 seconds; the aortic occlusion was performed by increasing the arterial systemic resistance (*Ras*) up to a value of 2.2 mmHs*s/mL in 10 seconds. Pressure and volume in the left ventricle were recorded and plotted in the PV plane (Figure 2.19).
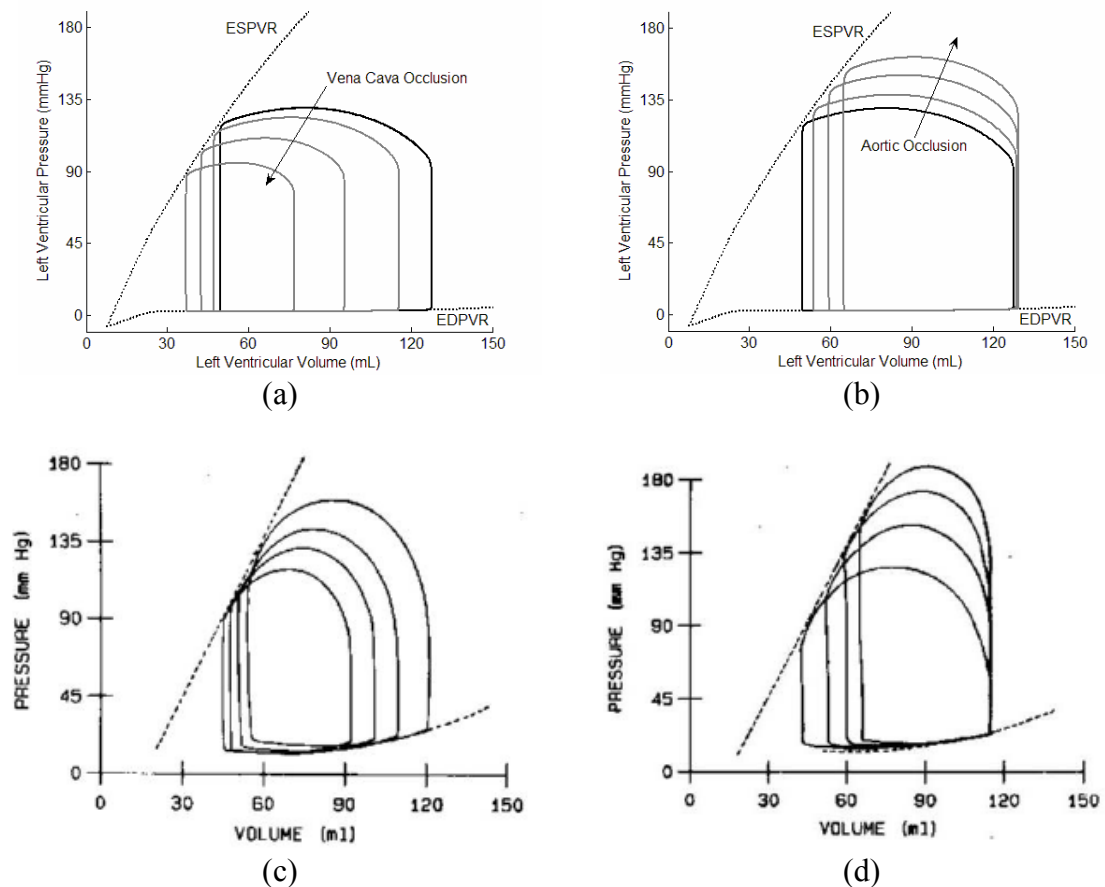
Figure 2.19 – (a) effect of changing end diastolic pressure (preload) by transient vena cava occlusion in the mathematical model - afterload constant; (b) effect of a varying resistive term of the arterial impedance (afterload) by transient occlusion of the aorta in the mathematical model- preload constant; (c) and (d) the same as in (a) and (b) from (Sagawa et al., 1988, p. 113).

The modeled ventricle behaves according to the studies on PV loops reported in (Sagawa et al., 1988) and previously described in the ventricular preload and afterload section of Chapter 1. Comparison with literature data of preload and afterload effects on the left ventricular PV loop is shown in Figure 2.19.

*Chapter 3**

A hydrodynamic numerical model of the MicroMed-DeBakey VAD® : software and hardware tools used for identification.

This chapter describes the identification and numerical modeling of an axial flow blood pump (MicroMed-DeBakey VAD®). The procedures and mathematical techniques used for identification and validation are first presented. The experimental setup used for the axial flow pump identification is then described. It comprised a displacement pump, which was also identified and controlled to properly generate the VAD identification signals; an air-trapped reservoir; an adjustable tube clamp resistance and tube connections. The blood pump identification results follow.

1 Introduction

The identification and modeling of a ventricular assist device (VAD) is of particular interest for two main reasons. The first reason is the possibility to study the VAD interaction with the native impaired heart and circulation and the design of VAD control strategies, on a mathematical model basis (Choi, 1998, Giridharan et al., 2002, Schima et al., 2004, Vollkron et al., 2002, Wu et al., 2005). The second reason is to investigate algorithms that can estimate online variables or hemodynamic states, otherwise not measurable or of difficult clinical access (Bertram, 2005, Schima et al., 1992). Among VADs, rotary blood pumps have received, in the last years, increasing interest from the scientific community because they offer a cost-effective way to assist the failing heart. Moreover simpler design, fewer moving parts, small size, simpler surgical procedures for implantation and better patients quality of life would answer the shortcomings of positive displacement blood pumps (Goldstein, 2003 Sep). Although literature reports on both centrifugal or axial flow blood pump identification and modeling (Ayre et al., 2003, Choi, 1998, Tanaka et al., 2003, Vandenberghe, 2004), a few information could be found on the MicroMed-DeBakey VAD® (Vollkron, 2004), which is nowadays one on the most used axial flow pump in clinical applications.

The MicroMed-DeBakey VAD® Pump System includes the titanium pump and inlet cannula, the percutaneous cable, the flow probe, and the outflow graft. The pump is attached to a titanium inlet cannula that is placed into the left ventricle. A graft is connected to the pump outlet and attached to the aorta. The Figure 3.1a shows the individual components of the pump. The inducer/impeller is the only moving part of the pump. It has six blades with eight magnets hermetically sealed in each blade. The inducer/impeller spins at speeds between 7.5–12.5 krpm and is capable of generating flow in excess of 10 L/min. The components are fully enclosed in a titanium flow tube that has been hermetically sealed. The pump is driven by a brushless DC motor stator that is contained in the stator housing (Figure 3.1b).

(a)   (b)
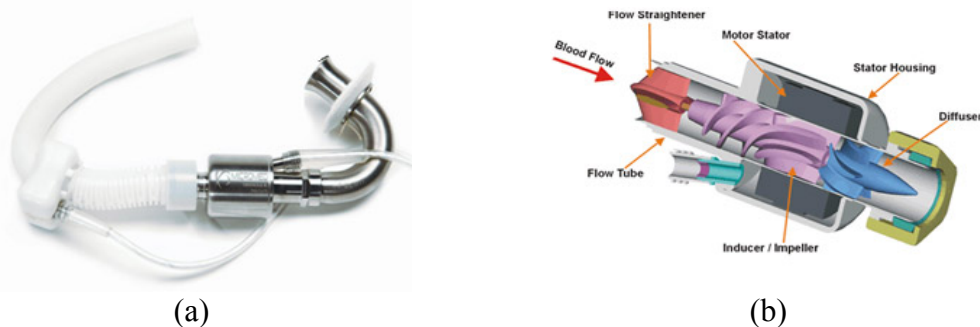
Figure 3.1 – (a) pump components; (b) cross section of the axial flow pump[6].

---

[6] http://www.micromedtech.com/products2.html. Accessed October 01, 2007.

The aim of the study presented in this chapter was to identify a dynamic model which describes the hydraulic behavior of the MicroMed-DeBakey VAD$^{®}$.

In section 2, the materials and methods section, the procedures and mathematical techniques used for identification and validation are presented; the experimental setup and VAD identification protocol are described. In section 3 results of the identification and discussion are presented. Section 4 draws conclusions.

2   Materials and Methods

2.1 *Identification procedure and theoretical background*

Parametric and nonparametric time and frequency domain identification techniques are broadly used for cardiovascular and prosthesis modeling (Avanzolini et al., 1980, Fetics et al., 1999, Milnor, 1989, Yu et al., 2001). Measurement noise constitutes the main limitation to the applicability of sophisticated techniques, mainly because of the difficulty in discriminating measurement artifacts from true information. A systematic approach to identification and modeling that allows checking the validity of the identification process and its results is therefore highly desirable.

The identification procedure used for the modeling purposes comprises usually several steps as shown schematically in Figure 3.2.
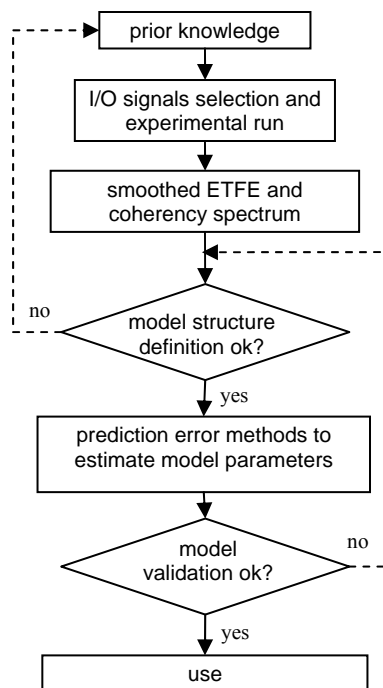
Figure 3.2 – identification procedure

The first step is the choice input and output measurements of the system we want to identify, they are respectively the signals that force the system

(either controllable or not), and the measurable outcomes. The choice of input-output signals is always guided by prior knowledge of the physics of the system. Once selected, the appropriate I/O signals are acquired.

The second step consists of a nonparametric frequency domain identification performed on the acquired signals. In particular, the transfer function between the input and output signals is estimated by means of a stochastic spectral estimation technique. This estimate is usually referred to as the Empirical Transfer Function Estimate (ETFE) (Ljung, 1998, p. 173), symbolized as $\hat{G}_N\left(e^{j\omega}\right)$.

The third step of the identification procedure is a parametric identification of an assumed model structure. Usually those methods are known as *prediction-error identification methods* (Ljung, 1998, p. 199), where the parameter values ($\hat{\theta}$) are estimated minimizing a norm (V, quadratic or nonquadratic) of the prediction error vector (ε), as shown in equation (3.1). This vector is calculated as the difference between the measured system outcomes and the ones predicted by the model: $\varepsilon\left(\hat{\theta}\right) = y - \hat{y}\left(\hat{\theta}\right)$.

$$\hat{\theta} = \arg\min\left\{V\left(\hat{\theta}, \varepsilon\right)\right\} \tag{3.1}$$

Here "arg min" means "the minimizing argument of the function".

The last step of the identification procedure is the evaluation of the model in comparison to its intended purpose. This step is known as model validation. Different measures to assess a model's ability to reproduce the acquired data can be used. Two measures are particularly useful: the Root Mean Square Error, RMSE, equation (3.2), and the so called Percent Variance Accounted For, %VAF, equation (3.3) (Westwick and Kearney, 2003, p. 105):

$$RMSE = \sqrt{\frac{1}{N}\sum_{k=1}^{N}\left[y(k) - \hat{y}\left(u(k), \hat{\theta}_N\right)\right]^2} \tag{3.2}$$

$$\%VAF = \left(1 - \frac{\text{var}\left(y_N - \hat{y}_N\right)}{\text{var}\left(y_N\right)}\right) \cdot 100 \tag{3.3}$$

in equation (3.2) $y(k)$ and $\hat{y}\left(u(k), \hat{\theta}_N\right)$ represent the measured and estimated sampled signals, where N is the total number of samples and $k=1, 2, \ldots, N$. The estimated signal is a function of the input $u(k)$, of the model structure and its parameter values ($\hat{\theta}_N$). In equation (3.3) $var(x_N)$ indicates the estimate of the variance, normalized by N samples, of the vector x_N. The %VAF represents the part of the measured output variation that is explained by the model. Ideally the predicted outputs $\hat{y}\left(u(k), \hat{\theta}_N\right)$ completely explain the measured outputs $y(k)$.

Frequency domain identification algorithms

The ETFE (nonparametric identification) is calculated as the ratio of the discrete Fourier transform of the time domain output over the discrete Fourier transform of the corresponding time domain input, both obtained experimentally, equation (3.4). It has been demonstrated that, as the number of samples N tends to infinity ($N \rightarrow \infty$), the ETFE becomes an unbiased estimate of the true I/O transfer function. However, it has a variance that does not decrease as N increases and depends on the signal-to-noise (S/N) ratio at each specific frequency (Ljung, 1998, p. 178).

$$\hat{\hat{G}}_N\left(e^{j\omega}\right) = \frac{Y_N(\omega)}{U_N(\omega)} \tag{3.4}$$

The poor asymptotic variance property of the ETFE can be improved by computing it for more overlapping signal sections of a specified constant window length, and then averaging the results as described by Welch (Welch, 1967). The coherency spectrum ($\hat{\kappa}_{yu}^N$), equation (3.5), is calculated along with the ETFE. It is a function of the power spectral density ($\hat{\Phi}_u^N$ and $\hat{\Phi}_y^N$) of the input and output signals (u and y) and the cross power spectral density ($\hat{\Phi}_{yu}^N$) of u and y. The coherency spectrum varies from 0 to 1 as a function of frequency and indicates how well input u correlates to output y at each frequency. A value of 1 indicates perfect correlation between u and y.

$$\hat{\kappa}_{yu}^N(\omega) = \sqrt{\frac{\left|\hat{\Phi}_{yu}^N(\omega)\right|^2}{\hat{\Phi}_y^N(\omega) \cdot \hat{\Phi}_u^N(\omega)}} \tag{3.5}$$

The nonparametric frequency domain identification procedure does not assume any model structure and it is sometimes referred to as model-free identification. The ETFE represents, therefore, a useful tool to assess a suitable parametric model structure for the system, and the coherency spectrum indicates whether the generated data contain enough information to identify the model parameters of the physical system.

For parametric frequency domain methods the goal is to estimate the real coefficients (α_i and β_i) of the rational transfer function model of equation (3.6) using a discrete set of measured input and output spectra ($U_M(\omega)$, $Y_M(\omega)$).

$$\hat{G}\left(e^{j\omega}, \hat{\theta}\right) = \frac{\sum_{i=0}^{n} \alpha_i \cdot s^i}{\sum_{i=0}^{d} \beta_i \cdot s^i} \tag{3.6}$$

The parameter estimates are found by minimizing a quadratic-like cost function, which is usually a non-linear function of the measurements and

model parameters, one example is given in equation (3.7) (Pintelton et al., 1994).

$$V_M\left(\hat{\theta}_M, U_M(\omega), Y_M(\omega)\right) = \frac{1}{2}\sum_{k=1}^{M}\left|\log \hat{G}\left(e^{j\omega_k}, \hat{\theta}\right) - \log \hat{\hat{G}}\left(e^{j\omega_k}\right)\right|^2 \qquad (3.7)$$

This norm V_M can be minimized using the Simplex Search Method (Lagarias et al., 1998), which is a direct search method that does not use numerical or analytic gradients.

Time domain identification algorithms

Parameters of the selected model structure ($\hat{\theta}_N$) are estimated, for the time domain methods, by minimization of a measure of the discrepancy, over N samples, between the measured and estimated sampled signal, $y(k)$ and $\hat{y}\left(u(k), \hat{\theta}_N\right)$. In particular, when the sum of the squares of the differences between the measured and estimated signals is chosen, one has the well known Least Squares Criterion, equation (3.8).

$$V_N\left(\hat{\theta}_N, u_N, y_N\right) = \frac{1}{N}\sum_{k=1}^{N}\frac{1}{2}\left[y(k) - \hat{y}\left(u(k), \hat{\theta}_N\right)\right]^2 \qquad (3.8)$$

The norm V_N can be minimized again using the Simplex Search Method (Lagarias et al., 1998).

Among different prediction error algorithms the Extended Kalman Filter (EKF) (Gelb, 1974, p. 182) can be selected to perform the parametric estimation in time domain. Along with other capabilities, the EKF can identify time-varying parameters of continuous-time, non-linear models and it produces an optimal estimate in the sense that the error is statistically minimized given noise corrupted data.

The filter equations can be derived writing the system in state space form, i.e. state and measurement equations as in (3.9), and giving the initial state conditions $\underline{x}(0) \sim N(\hat{\underline{x}}_0, P_0)$, where the initial estimate of the state is the vector $\hat{\underline{x}}_0$, and the initial estimate of the error covariance matrix P_0 is a diagonal matrix with values depending of the level of uncertainty of the initial state vector values (i.e. the higher the values the uncertain the initial state estimate).

$$\begin{cases} \dot{\underline{x}}(t) = \underline{f}(\underline{x}(t), t) + \underline{g}(\underline{u}(t), t) + \underline{w}(t) \\ \underline{y}(t) = \underline{h}(\underline{x}(t), t) + \underline{v}(t) \end{cases} \qquad (3.9)$$

Here $\underline{x}(t)$ is the state vector, $\underline{u}(t)$ the input vector, $\underline{y}(t)$ the measurement vector, $\underline{w}(t)$ and $\underline{v}(t)$ are process and measurement noise vectors respectively. The process noise vector represents model parameters uncertainty, and it is usually assumed to be a zero mean white Gaussian process with spectral density matrix (Q) which reflects the level of confidence in the estimates of the state variables. This matrix is usually set to be time-invariant and diagonal. Measurement noise vector assumed as a

zero mean white Gaussian noise process with spectral density matrix (R) with variance related to the accuracy of the measurements. This matrix is also set to be time-invariant and diagonal.

The vectors $\underline{f}$ and $\underline{h}$ are in general nonlinear functions of the state and the vector $\underline{g}$ is a nonlinear function of the input.

The EKF state and the error covariance (a measure of the estimated accuracy of the state estimate) equations can be written:

$$\dot{\hat{\underline{x}}}(t) = \underline{f}(\hat{\underline{x}}(t), t) + \underline{g}(\underline{u}(t), t) + K(t) \cdot \left[\underline{y}(t) - \underline{h}(\hat{\underline{x}}(t), t) \right] \tag{3.10}$$

$$\dot{P}(t) = F(\hat{\underline{x}}(t), t) \cdot P(t) + P(t) \cdot F^{T}(\hat{\underline{x}}(t), t) + Q - K(t) \cdot H(\underline{x}(t), t) \cdot P(t) \tag{3.11}$$

where $K(t)$ is calculated as shown in equation (3.12) and represents the so-called optimal gain matrix:

$$K(t) = P(t) \cdot H^{T}(\hat{\underline{x}}(t), t) \cdot R^{-1} \tag{3.12}$$

finally matrices F and H are calculated as follows:

$$F(\hat{\underline{x}}(t), t) = \left. \frac{\delta \underline{f}(\underline{x}(t), t)}{\delta \underline{x}(t)} \right|_{\underline{x}(t) = \hat{\underline{x}}(t)}$$

$$H(\hat{\underline{x}}(t), t) = \left. \frac{\delta \underline{h}(\underline{x}(t), t)}{\delta \underline{x}(t)} \right|_{\underline{x}(t) = \hat{\underline{x}}(t)} \tag{3.13}$$

Substantially the state estimate $\hat{\underline{x}}(t)$ is calculated by the state prediction corrected by available measurements, equation (3.10). Measurements are weighted by the optimal gain matrix $K(t)$, which is in turn calculated by minimizing the estimated error covariance, equation (3.11). Linearization of the estimation problem is, in fact, derived by means of a linear Taylor series expansion of the system equations about the current state estimate, and dropping all but the first term of the power series (Gelb, 1974, p. 184).

Axial flow VAD: steady state identification and theory

The MicroMed-DeBakey VAD® was previously identified in steady state operation mode (Vollkron, 2004). By running the pump at eleven pump rotating speeds ranging form 7500 rpm to 12500 rpm, the pressure head across the pump was, for each speed value, stepwise modified by means of a controllable concentrated loss. The flow delivered by the pump was recorded. The working fluid used was a 40% glycerin-water mixture that reproduces quite well the viscous properties of blood. The so obtained flow/head curves are shown Figure 3.3. To make the figure clearer only six of the eleven curves are displayed; the other five curves are situated between the plotted ones. Curves at negative flow are also displayed because the backflow condition through the pump is of interest. This represents, in fact, the condition of pump stopped due to malfunction. Backflow from the aorta through the ventricle occurs.

The flow/head curves of Figure 3.3 are consistent with the ones predicted by axial flow pumps theory. They show a decreasing head for increasing flow and with an inflection point.
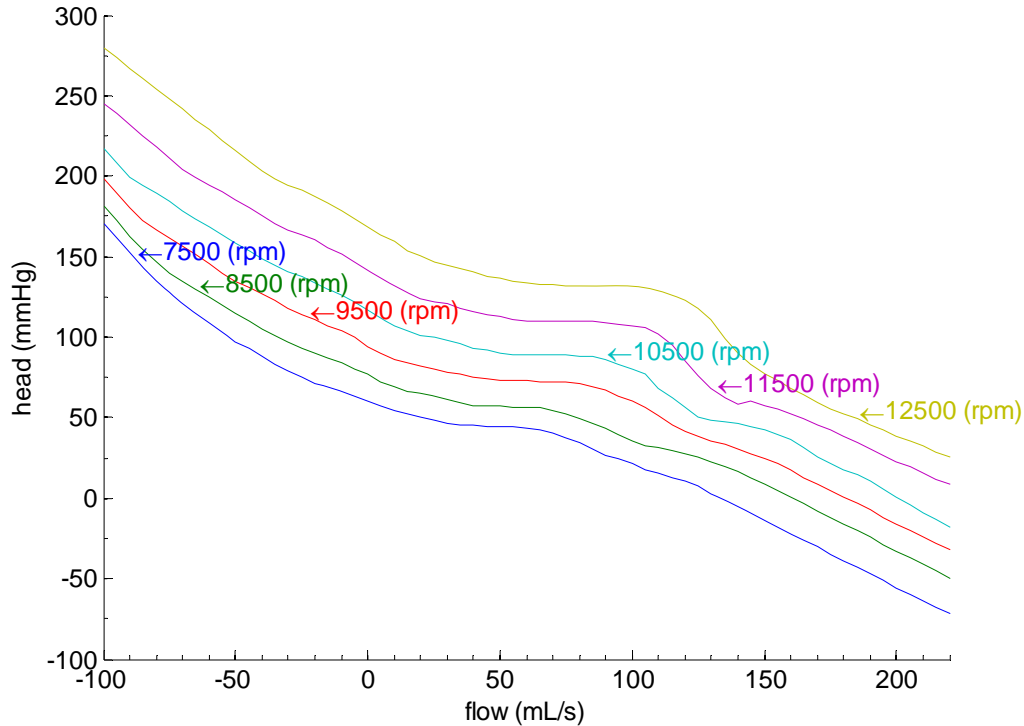
Figure 3.3 – steady-state identification of the axial flow MicroMed-DeBakey VAD®; flow-head characteristics; modified from (Vollkron, 2004).

In an axial flow pump, liquid particles leave the impeller at the same radius at which they enter. Applying Euler's head equation to a point on the impeller periphery and noting that the peripheral velocities of the impeller are equal at the impeller entrance and discharge ($u_1=u_2=u$):

$$H_e = \frac{c_{u2}^2 - c_{u1}^2}{2 \cdot g} - \frac{w_{u2}^2 - w_{u1}^2}{2 \cdot g} \qquad (3.14)$$

being c_{u2} and c_{u1} the projection of the absolute flow velocity vector (c) on the peripheral impeller velocity vector (u), at the pump entrance and discharge respectively; w_{u2} and w_{u1} the projection of the relative flow velocity vector (c) on the peripheral impeller velocity vector (u), at the pump entrance and discharge respectively, g is acceleration due to gravity. Assuming that the fluid approaches the impeller without prerotation ($c_{u1}=0$ and $w_{u1}=u$), and substituting $c_{u2}=u-w_{u2}$ equation (3.14) reduces to:

$$H_e = \frac{u^2}{g} - \frac{u \cdot w_{u2}}{g} \qquad (3.15)$$

here w_{u2} is related to the flow Q_e through the pump, being $w_{u2}= w_2 *cos\beta_2$ (β_2 the vane angle at the pump discharge) and $w_2= Q_e/(A_2*sin\beta_2)$ (A_2 the effective discharge area). Equation (3.15) can be rewritten:

$$H_e = \frac{u}{g}\left(u - \frac{Q_e}{A_2} \cdot \cot \beta_2\right) \tag{3.16}$$

where the angle β_2 is always $<90°$ and equation (3.16) represents a line with negative slope that intercepts the zero flow axis at the point u^2/g. The head, when flow is zero, is dependent on the square of the impeller speed u. By fitting a quadratic function of speed through the zero flow speed/head curve a consistent result is found (Figure 3.4).
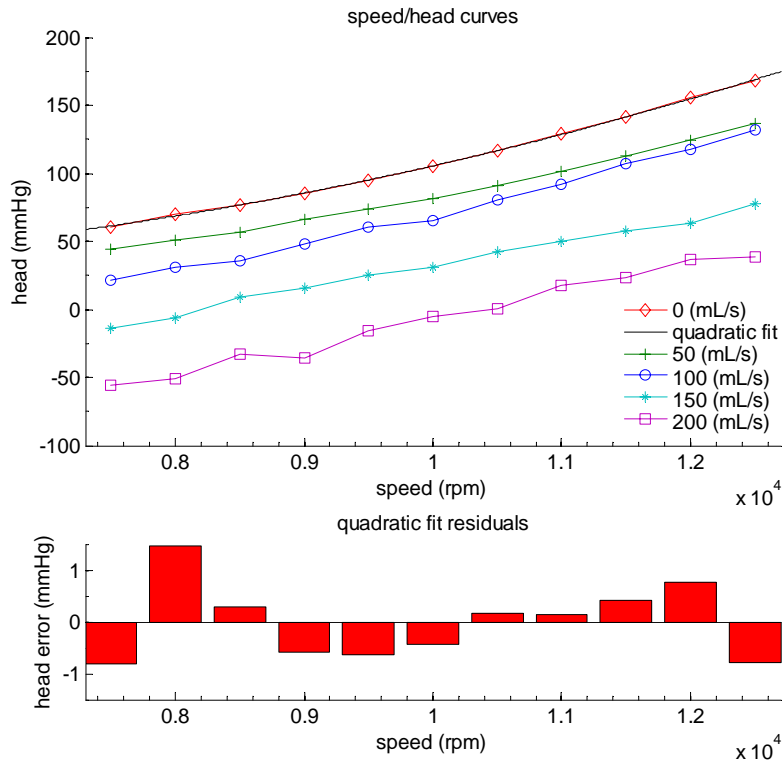
Figure 3.4 – steady-state identification of the axial flow MicroMed-DeBakey VAD[®]; speed-head characteristics.

It must be noted that the head produced at different radii are different, being maximum at the periphery and minimum at the hub. The pump total head is therefore an integrated average. The hydraulic integration of the head over the whore impeller area takes place in the discharge casting. From equation (3.16) it is also clear that as the vane angle β_2.decreases the negative slope increases. This is shown experimentally in Figure 3.5a.

The real flow/head characteristic curve differs from theoretical one of equation (3.16) because of the losses and several other design elements. The real axial pump characteristics usually show an inflection point, like the one of Figure 3.3. The measured flow/head curves of Figure 3.3 are dependent on a number of design elements that does not entry directly into the theoretical discussion (Stepanoff, 1957, p. 144). These include: (1) hub ratio; (2) chord-spacing ratio (l/t); (3) number of vanes.

The hub ratio is the ratio of the impeller hub to the impeller outside diameter. This ratio is directly connected with the specific speed of the axial flow pump. Higher specific speed pumps have smaller hubs, which give a greater free area for the flow and a smaller diameter to the average streamline, resulting in greater capacity and lower head. In Figure 3.5b the characteristics of three fans having the same number of impeller vanes (seven) and approximately the same vane settings is shown, here effects of different hub ratio (hub ratio is 0.702, 0.573 and 0.426 for curve A, B and C, respectively) are shown (Stepanoff, 1957, p. 146).

The chord-spacing ratio (l/t) is the ratio between l, the vane length, and t, is the vane spacing or "pitch". This parameter is an index of "vane solidity" and influences the characteristic curves as show in Figure 3.5c, where the impellers had four vanes each, speed was 730 rpm, vane angle $\beta_2=20°$ and l/t ratios of 0.4, 0.6 and 0.8 (Stepanoff, 1957, p. 146).

The effect of number of vanes on pump characteristic curves is shown in Figure 3.5d, the head increase with the number of vanes and this is entirely due to the increase in the l/t ratio (Stepanoff, 1957, p. 147).

(a)

(b)

(c)

(d)
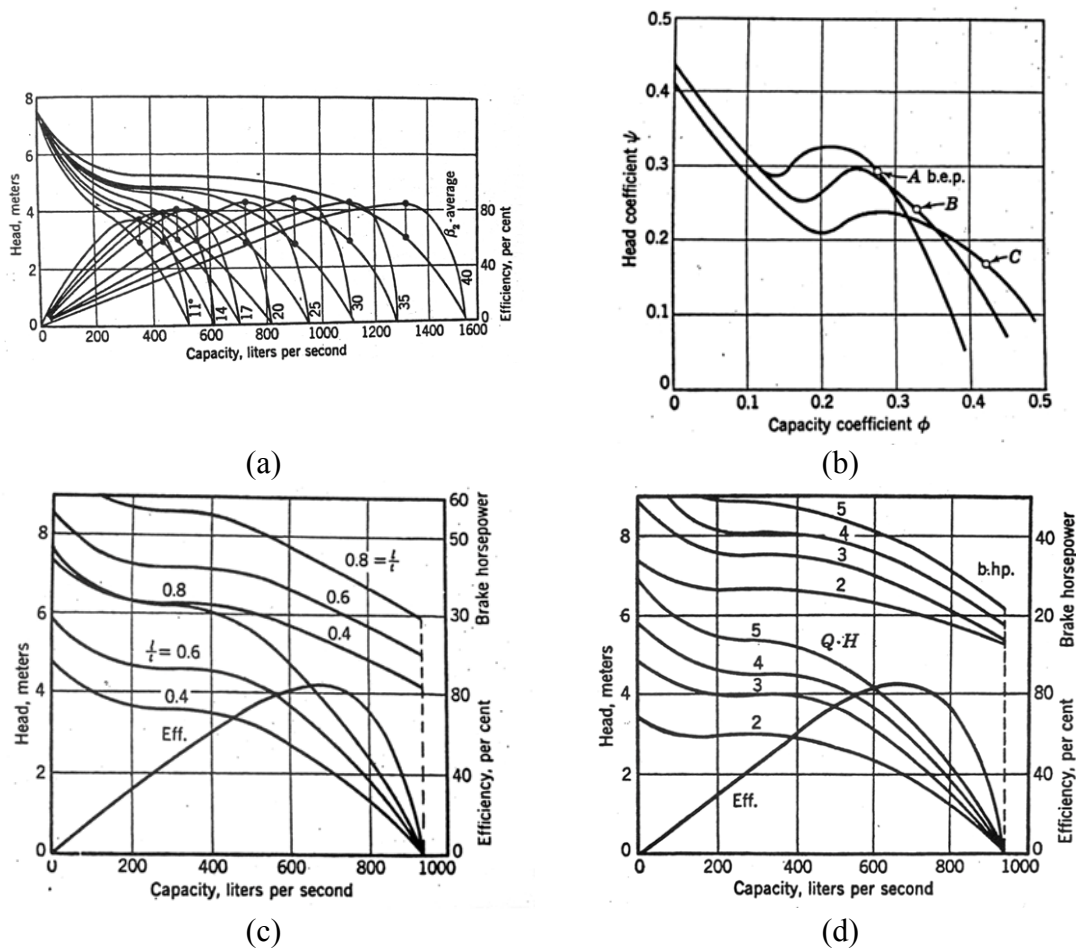
Figure 3.5 –flow/head characteristics in axial flow pumps depending on (a) vane angle β_2; (b) hub ratio; (c) chord-spacing ratio l/t; (d) number of vanes; all the figures are reproduced from (Stepanoff, 1957, pp. 145 to 148).

Because the axial flow VAD is inserted between the ventricle and the aorta, the pump does never work in steady-state. The pulsating ventricle develops a VAD inlet pressure that oscillates between about 0 and 100 mmHg, thus having a flow that is also pulsating. A static model such as the one depicted in Figure 3.3 failed to represent the pump in its real operating conditions, where fluid inertia plays an important role. For this reason a hydro-dynamic model of the axial flow VAD must be sought.

2.2 VAD Identification: experimental setup

To identify hydro-dynamically the VAD an experimental setup was build. This experimental setup comprised a displacement pump, an air-trapped reservoir; an adjustable tube clamp resistance and tube connections (Figure 3.6).
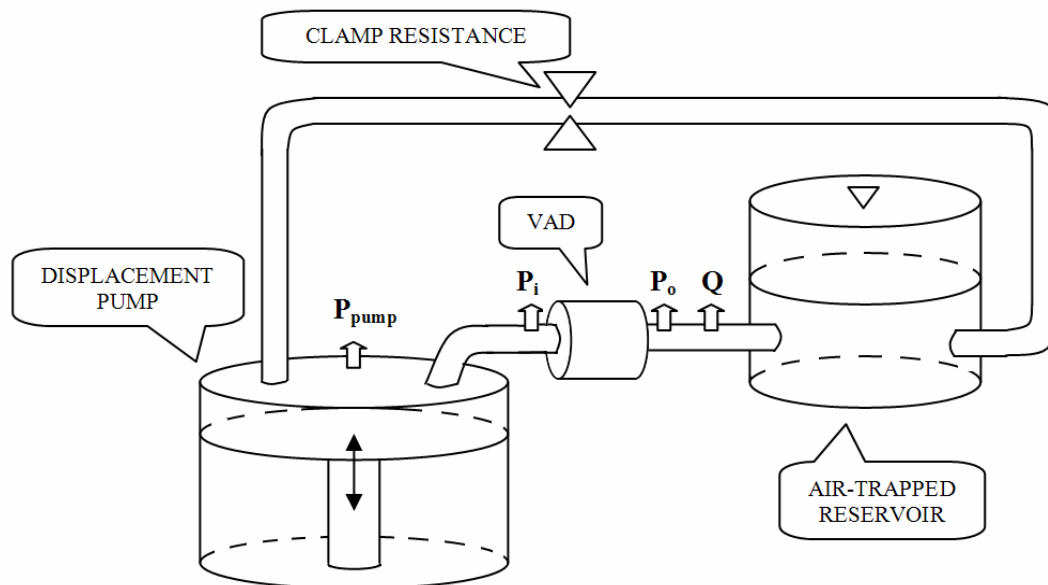
Figure 3.6 – schematic experimental setup for the VAD identification.

The piston of the displacement pump head consists of a stainless-steel bellow, which is driven by a modified linear shaker actuator (Model V455/6, Ling Dynamics Systems, Middleton, WI, USA) of the voice-coil type. Modifications listed in detail in (Neubacher, 1999). These were aimed to reduce the spring effects of the coil mounting system. The voice-coil is attached to the apex of a moving piston. By driving a voltage/current through the voice-coil, a magnetic field is produced. This magnetic field causes the voice-coil to react to the magnetic field generated by a permanent magnet fixed to the actuator's frame, thereby moving the piston (Figure 3.7).

A full-state feedback current digital control algorithm (Franklin et al., 1998, p. 279) was designed for the displacement pump. In order to design its control the displacement pump was first identified. The current control

was designed on the derived linear model and than implemented on the physical device. This allowed to control the coil current up to frequencies of 65 Hz. By adding a simple integral control loop, the pressure into the displacement-pump could be controlled as well.
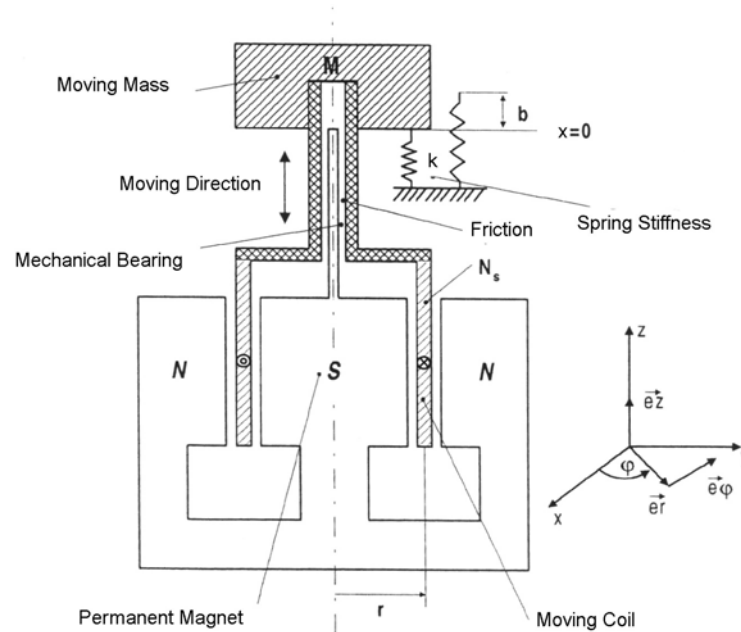
Figure 3.7 – voice-coil schema; modified from (Neubacher, 1999).

The displacement pump was used to modulate, through both current and pressure control, the pressure at the inlet of the VAD. Being the VAD connected with its inlet section to the displacement pump and the outlet section to an air-trapped reservoir. The air-trapped reservoir was connected back to the displacement pump through a tube which had embedded a clamp resistance (Figure 3.6). All the connections were PVC tubes of ½ inch diameter. The circuit was filled with 2.5 L of a 40% glycerin-water mixture to better mimic the blood fluid properties. An air volume of 640 mL was left into the air-trapped reservoir, and then the circuit was preloaded by further inoculation of fluid into the closed circuit until the pressures reached 80 mmHg.

Pressures were measured at the inlet and the outlet sections of the VAD (Pi and Po respectively), and in the displacement-pump chamber ($Ppump$) by means of disposable pressure transducers (Model TruWave, Edwards Lifesciences, Irvine, CA, USA). Flow (Q) was measured at the outlet of the VAD by means of an ultrasonic transducer (Model H11XL, Transonic Systems Inc., Ithaca, NY, USA). Rotational speed of the VAD (ω) was measured by counting the frequency of the PWM signals, and could be controlled by means of a modified controller box. The current flowing into the voice-coil was measured by a transducer which employs Hall effect (Model LTA100P/SP1, LEM holding SA, Plan-les-Ouates/Genève, Switzerland), the piston position was measured by means of a LVDT

transducer (Model MDCL20K1505, MEGATRON Elektronik AG & Co, Putzbrunn/München, Germany).

All signals were acquired with a sampling time (*Tsmp*) of 0.001 sec at a resolution of 16 bits, using a dSPACETM DS1103 signal-processor system (dSPACE GmbH, Padeborn, Germany). Computations were performed with Matlab® (The MathWorks Inc., Natick, MA, USA).

Displacement Pump Identification

The displacement pump consist of the linear actuator, connected to the pump piston, and its driving power amplifier. To identify the actuator and its driving power amplifier, a composed input voltage signal was fed into the amplifier (U_{in}). This signal was the result of the sum of a sinusoidal chirp with amplitude 0.1 V and frequencies ranging from 0.01 Hz to 100 Hz, a multi step function of amplitude ±0.1 V and a Gaussian random noise with mean μ=0 V and variance σ=0.02 V. The input was so created to get a signal with power on a broadband frequency spectrum (Ljung, 1998, p. 416), which at the same time does not saturate the electro-mechanical system. The step component gives power at low-frequencies, the chirp component power at frequencies up to 100 Hz and the random component power at high-frequencies (Figure 3.8).
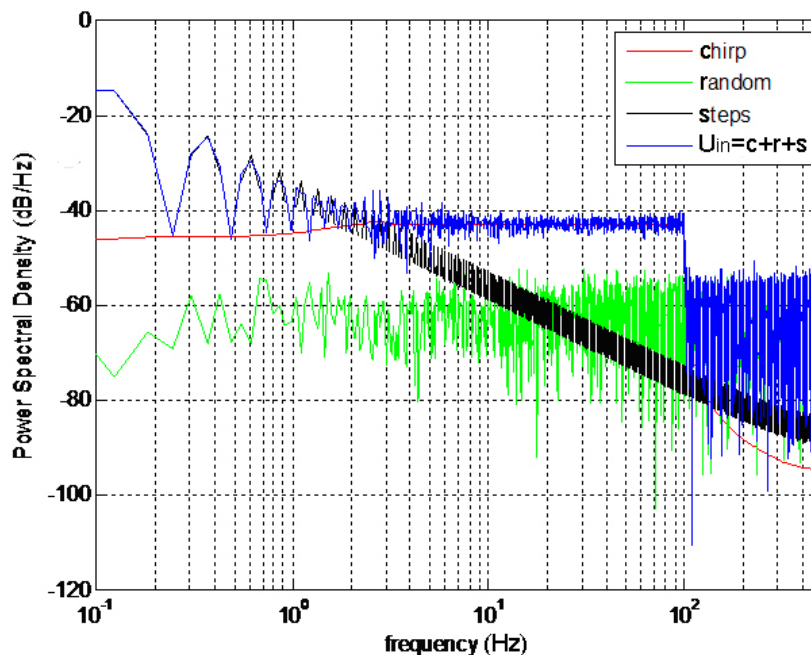
Figure 3.8 – power spectral density of the input voltage signal (U_{in}) to the amplifier for the actuator identification (blue), with its chirp (red), random (green) and step (black) components.

The generated outputs, with the pump chamber disconnected from the hydraulic circuit (no load), were then recorded: voltage from the amplifier (U_{amp}), the current into the voice-coil (i) and piston position (x). The time-domain input signal and the generated outputs are displayed in Figure 3.9.
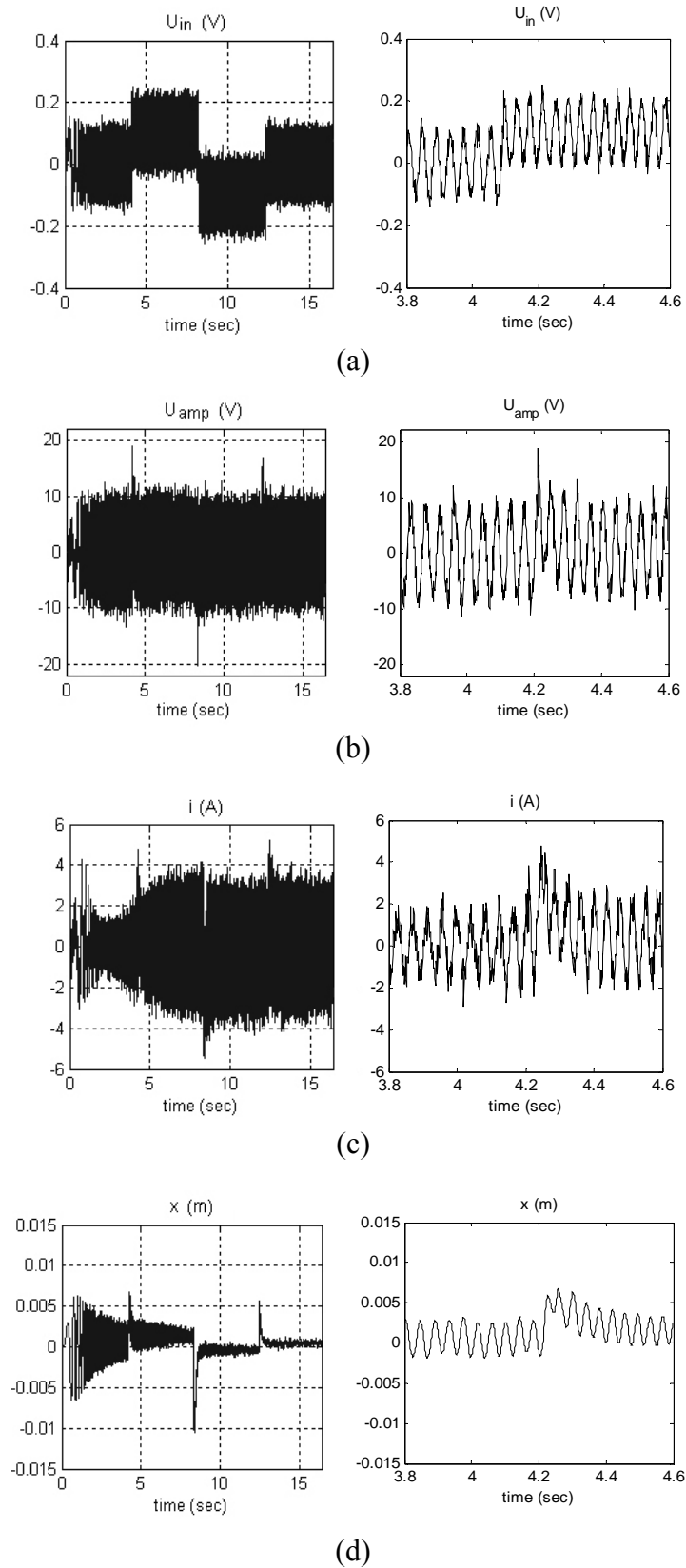
Figure 3.9 – (a) input voltage signal to the amplifier and (b) recorded output voltage from the amplifier, (c) current into the voice coil and (d) piston position; the whole signals acquisition (left) and waveforms detail are shown (right).

The Empirical Transfer Function Estimate (ETFE) between the input and the voltage given by the amplifier to the coil (U_{in} → U_{amp}) was calculated, equation (3.4). A Fast Fourier Transformation using 2^{15} points was applied to the signals. A Hanning window whose width was 2^{10} samples was used to section the signals, with an overlap of 2^9 samples. Then the Bode diagram of a continuous zero-pole-gain system with one zero and one pole was fitted with the estimated experimental transfer function, leading to a model of the amplifier in the form:

$$\frac{U_{amp}(s)}{U_{in}(s)} = 79.74 \frac{s+1.084}{s+21.46} \qquad (3.17)$$

In the upper and middle panels of Figure 3.10 the magnitude and phase of the amplifier ETFE are shown (red lines), Bode plots of the identified amplifier, equation (3.17), are superimposed (black lines) to the experimental ones. In the bottom panel the coherency spectrum, equation (3.5), is displayed. Because the coherency spectrum approaches the unity at each frequency we can rely on the ETFE and its parametric fitting.
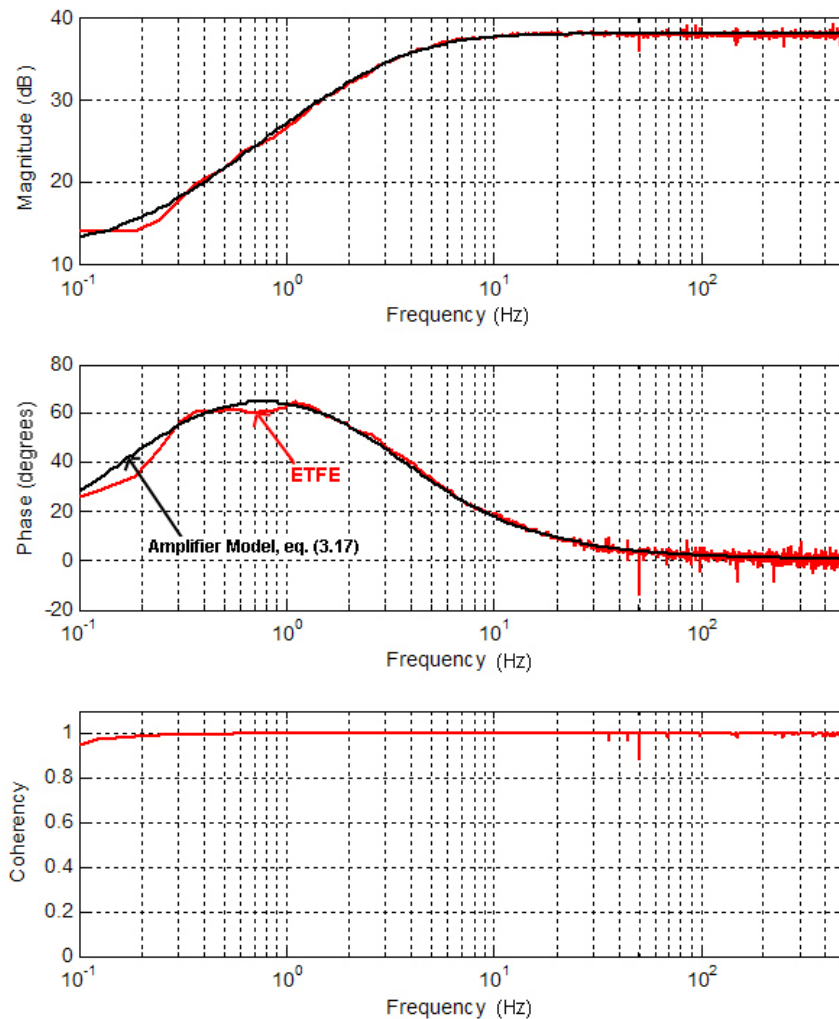
Figure 3.10 – upper panel: magnitude of the ETFE and of the amplifier; middle panel: phase of the ETFE and of the amplifier; bottom panel: coherency spectrum.

73

The visible decrease in the magnitude plot at decreasing frequencies (roll-off of 20 dB/decade) is caused in the amplifier by two main reasons: the output transformer of the push-pull amplifier and several resistance-capacitance coupling networks. This roll-off is undesirable. If we want to use the actuator to identify cardiovascular devices, the lower limit of the bandwidth of interest is about 1 Hz. Therefore a rectification network must be included into the actuator control algorithm to compensate for this low frequency roll-off.

Once the amplifier was modeled, three Empirical Transfer Function Estimates were calculated. A Fast Fourier Transformation using 2^{15} points was applied to the signals. A Hanning window whose width was 2^{10} samples was used to section the signals, with an overlap of 2^{9} samples. Specifically the ETFE were calculated between coil voltage and the coil current ($U_{amp} \rightarrow i$), between coil voltage and piston position ($U_{amp} \rightarrow x$), between coil current and piston position ($i \rightarrow x$). The obtained ETFEs are displayed in Figure 3.11, where the coherency spectrum for the three estimation is plotted as well.

From Figure 3.11 useful information can be inferred. From the ETFE between coil current and position (dashed green curves) it can be seen that a under-damped second order system (40 dB/decade roll-off) can satisfactory represent this ETFE. The resonant frequency is related to the moving elements mass and the spring stiffness, whether the damping relates to the viscous friction. The same resonant frequency can be seen in the ETFE between the voltage and the current into the coil (solid red curves). This transfer function estimate represents the load impedance seen by the power amplifier. The gain at zero frequency (DC gain) of this transfer function is the inverse of the electrical resistance of the coil. The last ETFE, between voltage and position (dotted blue curves), suggests a higher order system.

A close examination of the coherency spectrum (Figure 3.11, lower panel) shows that the notch in the region of the resonant frequency probably is an index of a spring and/or friction nonlinearity (being that part of the ETFE determined by spring/mass/damping); moreover lower coherency at low frequency could be related to a nonlinear electrodynamic coupling factor and/or to static friction (Kippel, 2006).
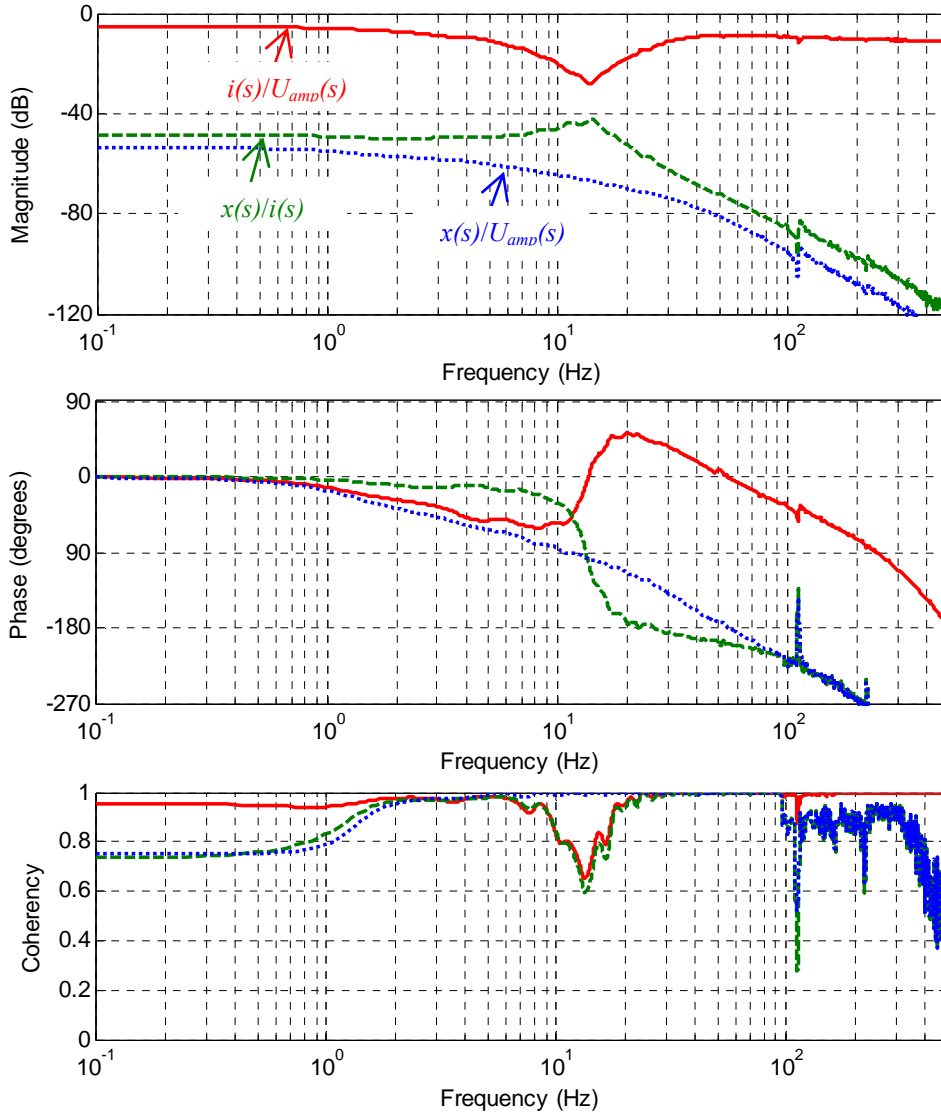
Figure 3.11 – Empirical Transfer Function Estimates: solid red = *i(s)/U$_{amp}$(s)*; dotted blue = *x(s)/U$_{amp}$ (s)*; dashed green = *x(s)/i(s)*. *U$_{amp}$* is the voltage fed by the amplifier into the coil, *i* is the current into the coil, *x* is the piston position. Upper panel: estimated magnitude; middle panel: estimated phase; bottom panel: coherency spectrum.

As a next step a parametric model of the actuator is sought. The model is obtained by writing the differential equations that rule the physics of the electro-mechanic system (Beranek, 1996, p. 185). In particular we have two coupled differential equations, the first for the electrical part, equation (3.18), and the second for the mechanical one, equation (3.19).

$$U_{amp}(t) - Kf \cdot v(t) = R_e \cdot i(t) + L_e \cdot \frac{di(t)}{dt} \tag{3.18}$$

$$Kf \cdot i(t) = M \cdot \frac{dv(t)}{dt} + F_{friction}(t) + F_{spring}(t) + F_{load}(t) \tag{3.19}$$

Here *U$_{amp}$(t)* is the voltage fed by the amplifier into the coil. The term *Kf*v(t)* represents the back electromotive force which is proportional to the moving coil speed *v(t)* through the coefficient *Kf*. This coefficient is the

effective instantaneous electrodynamic coupling factor (force/speed factor) and it is defined by the integral of the permanent magnetic flux density over the voice coil length. R_e and L_e are the coil electrical resistance and inductance, respectively. *Kf*i(t)* represents the piston driving force, proportional to the coil current *i(t)* through the same coefficient *Kf*. *M* is the mass of the moving elements. $F_{friction}(t)$ represents the friction force and $F_{friction}(t)$ the restoring spring force. To perform a transfer function analysis the system has to be linearized in all its components, therefore the friction force is approximated only with its viscous component, discarding the static friction contribution, thus having $F_{friction}(t) = F_v*v(t)$, where F_v is the viscous friction coefficient and *v(t)* the speed. The spring is modeled as a linear spring $F_{spring}(t) = k*x(t)$, where *k* is the spring stiffness and *x(t)* the moving coil position. $F_{load}(t)$ represents the load force acting on the piston surface.

Rearranging the equations (3.18) and (3.19) and substituting the *d/dt* operator with its Laplace transform *s*, three transfer functions, which corresponds to the calculated ETFE of Figure 3.11, can be written as:

$$\frac{i(s)}{U_{amp}(s)} = \frac{M \cdot s^2 + F_v \cdot s + k}{(M \cdot L_e) \cdot s^3 + (F_v \cdot L_e + M \cdot R_e) \cdot s^2 + (Kf^2 + k \cdot L_e + F_v \cdot R_e) \cdot s + k \cdot R_e} \quad (3.20)$$

$$\frac{x(s)}{U_{amp}(s)} = \frac{Kf}{(M \cdot L_e) \cdot s^3 + (F_v \cdot L_e + M \cdot R_e) \cdot s^2 + (Kf^2 + k \cdot L_e + F_v \cdot R_e) \cdot s + k \cdot R_e} \quad (3.21)$$

$$\frac{x(s)}{i(s)} = \frac{Kf}{M \cdot s^2 + F_v \cdot s + k \cdot} \quad (3.22)$$

the DC gain for the transfer functions of equations (3.20), (3.21) and (3.22) are then evaluated as:

$$DC_{gain}\left[\frac{i(s)}{U_{amp}(s)}\right] = \frac{1}{R_e} \quad (3.23)$$

$$DC_{gain}\left[\frac{x(s)}{U_{amp}(s)}\right] = \frac{Kf}{R_e \cdot k} \quad (3.24)$$

$$DC_{gain}\left[\frac{x(s)}{i(s)}\right] = \frac{Kf}{k} \quad (3.25)$$

moreover the natural frequency (f_n) and damping ratio (ζ) of the system represented by transfer function in equation (3.22) are easily determined and shown in equations (3.26) and (3.27).

$$f_n\left[\frac{x(s)}{i(s)}\right] = \frac{1}{2\pi} \cdot \sqrt{\frac{k}{M}} \quad (3.26)$$

$$\zeta\left[\frac{x(s)}{i(s)}\right] = \frac{F_v}{2 \cdot \sqrt{k \cdot M}} \cdot \quad (3.27)$$

Equation (3.23) states that the DC gain of the ETFE between voltage and current (solid red curve in Figure 3.11) is the inverse of the coil resistance. The value of coil resistance R_e is then determined from the red curve in Figure 3.11. By fitting a second order system to the ETFE between

current and position (dashed green curve in Figure 3.11), the numerical values of the natural frequency (f_n) and damping ratio (ζ) are identified. By knowing the moving elements mass (M), from equations (3.26) and (3.27), the spring constant (k) and the viscous friction coefficient (F_v) are determined. Form the DC gain of the ETFE between current and position (dashed green curve in Figure 3.11) and equation (3.25), the value of the force/speed coefficient (Kf) is determined. By fitting a third order system to the ETFE between coil voltage and position (dotted blue curve in Figure 3.11) and by letting the coil inductance (L_e) as the only unknown parameter, the latter can be identified. For the complete list of the identified actuator parameters see Table 3.1.

Table 3.1: identified actuator parameters.

Parameter	Value	Units
S (piston surface)	56.52	cm^2
Str (piston stroke)	2.540	cm
M (moving elements mass)	0.763	Kg
k (spring constant)	5336	N/m
F_v (viscous friction)	22.62	N/(m/sec)
R_e (coil resistance)	1.840	Ohm
L_e (coil inductance)	5.342	mH
Kf (force/speed coefficient)	19.94	N/A or V/(m/sec)
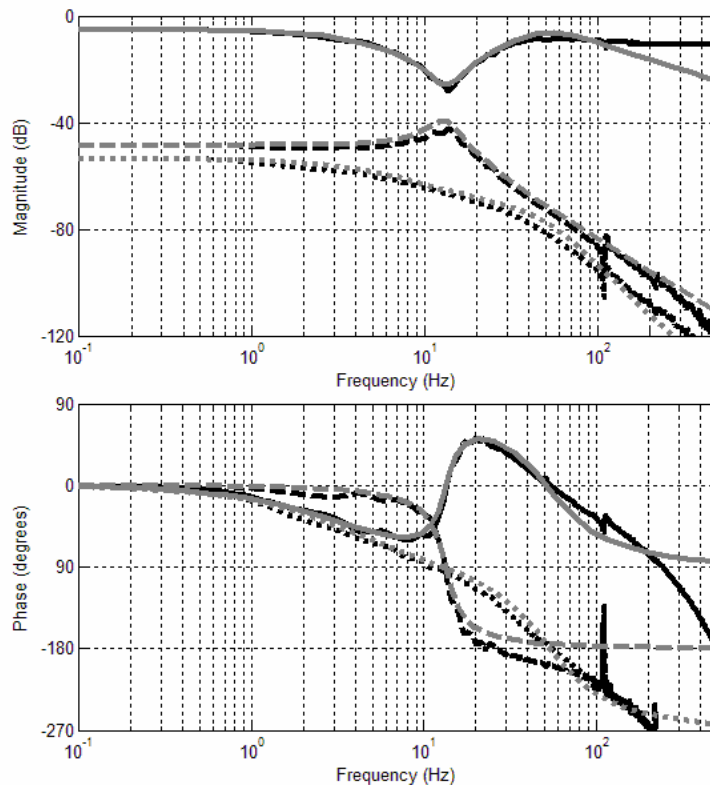
Figure 3.12 – comparison between the experimental ETFEs (**black**) and the Bode plots of the identified shaker model (**grey**).

In Figure 3.12 it is possible to see the experimentally estimated transfer functions plots (black lines) superimposed to the respective Bode plots obtained from the identified linear model (grey lines).

Most of the features of the ETFE are caught from the linear model, however some discrepancies are observable at high frequencies. In particular the difference in the magnitude plot for the transfer function between coil voltage and current (solid line in Figure 3.12) could be due to unmodeled increasing losses at increasing frequencies generated by eddy-currents in the iron material (Kippel, 2006).

Afterwards the model was implemented in Matlab$^\circledR$-Simulink$^\circledR$. It was possible to include in the Simulink$^\circledR$ model a nonlinear spring element and a more accurate and realistic model for friction (Figure 3.13).

(a)   (b)
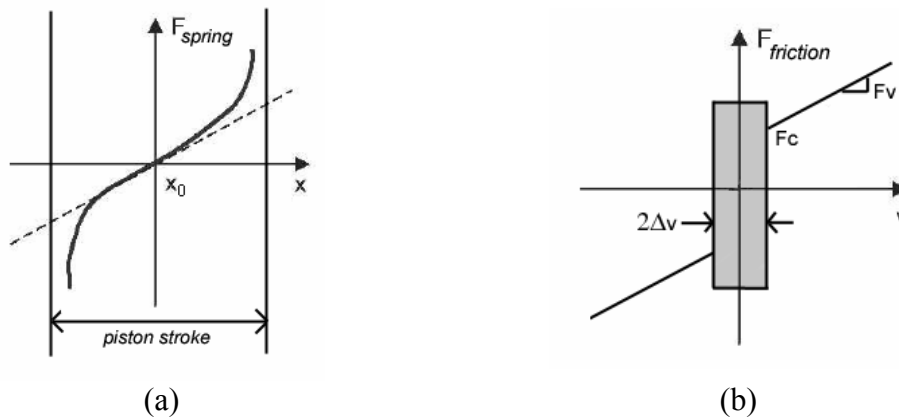
Figure 3.13 – (a) nonlinear spring force; (b) nonlinear friction force.

The nonlinear spring model was implemented to add the constrain of the piston stroke: when the piston reaches the end-stroke positions the nonlinear spring has infinite stiffness (Figure 3.13a).

The nonlinear friction model was necessary to reproduce the stick behavior of the piston when it inverts the motion direction (Figure 3.14).
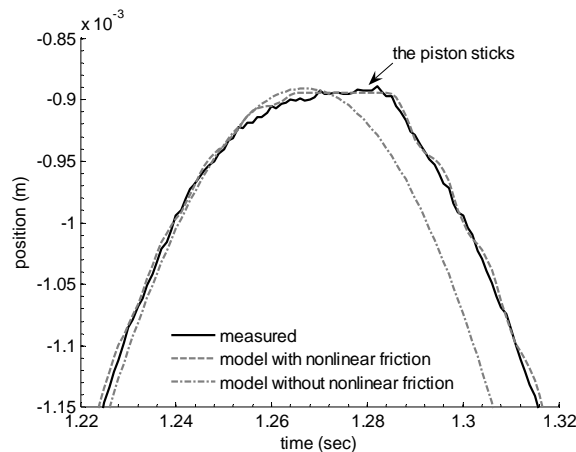
Figure 3.14 – piston position when the piston inverts the motion direction; measured position (solid) and model results with both nonlinear (dashed) and linear (dot-dashed) friction (i.e. only viscous friction) are shown.

The nonlinear spring was modeled according to the following relation:

$$F_{spring}(x) = k \cdot (x(t) - x_0) \cdot \frac{-1}{\tanh\left[(|x(t) - x_0| - Str/2) \cdot kSAT\right]} \qquad (3.28)$$

here x is the piston position, x_0 the unstretched position, k is the linear spring stiffness, Str is the piston stroke, $kSAT$ a coefficient which determines how fast the spring stiffens with increasing displacement.

To include static and Coulomb friction contributions, friction was modeled by the following relations (Karnopp, 1985):

$$F_{friction}(v, F) = \begin{cases} F_c \cdot \text{sgn}(v(t)) + F_v \cdot v(t) & |v| > \Delta v \\ \max(F(t), F_s) & |v| \leq \Delta v \end{cases} \qquad (3.29)$$

here $v(t)$ is the piston speed, F_c the Coulomb friction force, F_v the viscous friction coefficient, $F(t)$ is resultant force from the equilibrium in equation (3.19) except for the friction force, F_s is the static friction force, Δv is the zero velocity interval: outside this interval friction is a function of velocity, inside velocity is considered to be zero and friction is force dependent.

Parameter values of the nonlinear spring and friction models are reported in Table 3.2.

Table 3.2: actuator parameters for nonlinear spring and friction models.

Parameter	Value	Units
$x0$ (unstretched position)	-0.007	m
$kSAT$ (spring stiffening coefficient)	2000	–
Δv (zero velocity interval)	1e-5	m/sec
F_c (Coulomb friction)	5	N
F_s (static friction)	5	N

Displacement-Pump Control

The design objectives for the displacement pump control were: (1) current control with a closed loop flat response from DC up to about 75 Hz; (2) high disturbance rejection (the pressure load acting on the piston surface is considered the disturbance, this load may vary over a broad range depending on the hydraulic circuit connected to the pump); (3) robustness to parameter uncertainty and/or unmodeled nonlinearities; (4) rectification of the amplifier low-frequency roll-off.

To fulfill these objectives a full-state feedback digital control architecture was chosen (Franklin et al., 1998, p. 279). The control schema is shown in Figure 3.15. It comprises: (a) the control law as a feedback of a linear combination of all the state variables: $u = -K_x * x$; (b) a integrator term Ki, to increase disturbance rejection and robustness to parameter uncertainty; (c) a feedforward term $\bar{N}$, which performs the integrator pole cancellation and speeds up the response (Franklin et al., 1998, p. 323); (d) an amplifier rectification term.

Moreover a Kalman estimator is designed to reconstruct the full sate vector necessary for the feedback (piston speed is not measured). Piston speed may be available from the numerical differentiation of the piston position measurement. However this is a difficult operation performed on noise corrupted signals. The numerical differentiation leads, in fact, to the amplification of noise (Marble et al., 1981). For this reason the Kalman filter is used to reconstruct the state and estimate the piston speed.
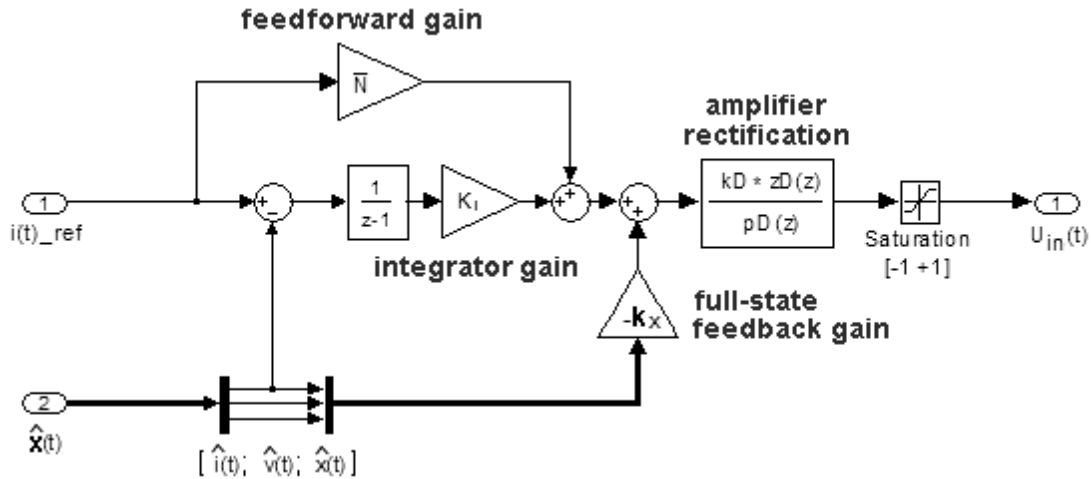
Figure 3.15 – current controller structure.

The system is first written in its state-space description (for a SISO system):

$$dx/dt = \boldsymbol{F}*\boldsymbol{x} + \boldsymbol{G}*u$$
$$y = \boldsymbol{H}*\boldsymbol{x}$$

(3.30)

where $\boldsymbol{x}$ is the state vector of the system, u is the input to the system, y the measured output we want to control, $\boldsymbol{F}$ is the system matrix, $\boldsymbol{G}$ the input vector, $\boldsymbol{H}$ the output matrix. They are shown in (3.31).

$$\boldsymbol{x} = \begin{bmatrix} i(t) \\ v(t) \\ x(t) \end{bmatrix}; u = U_{amp}; y = i(t)$$

$$\boldsymbol{F} = \begin{bmatrix} -R_e/L_e & -Kf/L_e & 0 \\ Kf/M & -F_v/M & -k/M \\ 0 & 1 & 0 \end{bmatrix}; \boldsymbol{G} = \begin{bmatrix} 1/L_e \\ 0 \\ 0 \end{bmatrix}; \boldsymbol{H} = \begin{bmatrix} 1 & 0 & 0 \end{bmatrix}$$

(3.31)

Because the control must be implemented in a digital form, the discrete equivalent of the system was calculated with the ZOH method (Franklin et al., 1998, p. 101), and a sampling time of 0.001 sec, thus having:

$$\boldsymbol{x}(k+1) = \boldsymbol{\Phi}*\boldsymbol{x}(k) + \boldsymbol{\Gamma}*u(k)$$
$$y(k) = \boldsymbol{H}*\boldsymbol{x}(k)$$

(3.32)

where $\boldsymbol{\Phi}$ is the system matrix and $\boldsymbol{\Gamma}$ the input vector of the discrete system.

Poles and zeros of the transfer function between voltage fed by the amplifier to the coil and current in the coil, $i(z)/U_{amp}(z)$, are sought (Table 3.3), being $i(t)$ the signal to be controlled and $U_{amp}(t)$ the driving input.

Table 3.3: open loop $i(z)/U_{amp}(z)$ poles and zeros

poles	zeros
$0.8072 \pm 0.2280i$	$0.9818 \pm 0.0813i$
0.9777	

By looking at the grid of Figure 3.16, it can be noted how the pole-zero map is related to the dynamical behavior of the system. In particular poles/zeros locations inside the unit circle, if real positive, represent critically damped (ζ=1) systems, if real negative or complex, underdamped (ζ<1) resonant systems. The complex zeros in Table 3.3 corresponds to the anti-resonance in the solid curve of Figure 3.12 (f_n=13.4 Hz, ζ=0.18); the complex poles in Table 3.3 corresponds to the resonance in the solid curve of Figure 3.12 (f_n=52 Hz, ζ=0.54); the real pole in Table 3.3 has a first order low pass effect with cutoff frequency f_c=3.59 Hz, damping ratio ζ=1.
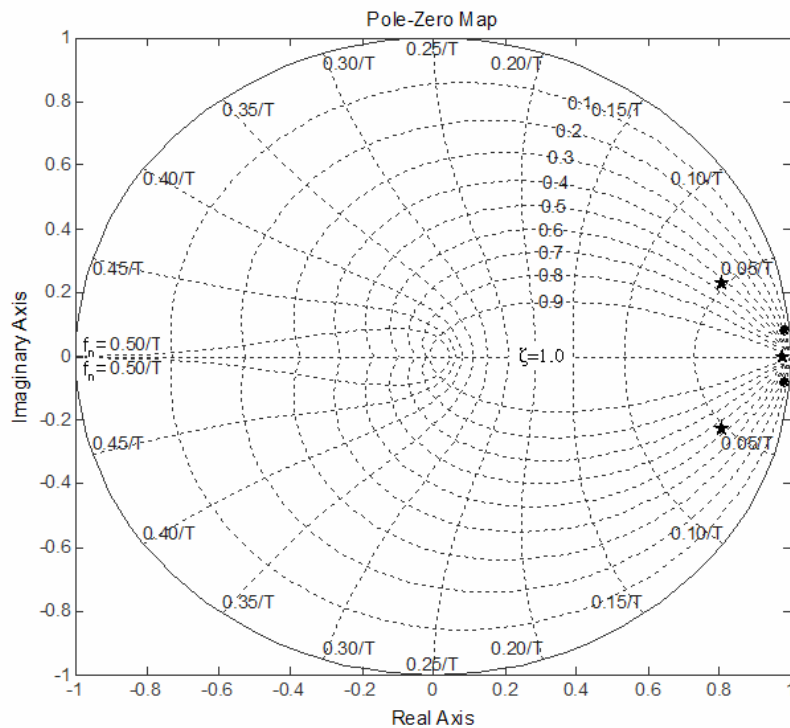
Figure 3.16 – pole-zero map of the $i(z)/U_{amp}(z)$ transfer function; (★) symbolizes the system poles, (●) symbolizes the system zeros.

The full state feedback control technique allows one to place the closed-loop poles in desired positions of the complex plane, thus determining the dynamic response of the controlled loop. It is desirable to have a closed-loop response that does not have resonances and that is fast enough for the control purposes. Therefore the poles should be located on the positive real

axis. Also the closer they to the zero the faster will be the response. However, when selecting the desired pole locations, it is always useful to keep in mind that the control effort required is related to how far the open-loop poles are moved by the feedback to the chosen closed loop locations.

An integral control was added. To do that the discrete model of the plant was augmented with the state x_I, equation (3.33). It represents the integral of the error between the reference command and the desired state we want to control ($e = r{-}y$).

$$x_I(k+1) = x_I(k) + e(k) \tag{3.33}$$

The selected closed loop pole locations (three system poles and one integrator pole) are then $\boldsymbol{p}$ = [0.900; 0.005; 0.910; 0.910]. By using the Ackermann formula (Ackermann, 1972) the integrator gain and the vector of feedback gains are then calculated: K_I=0.76599 and $\boldsymbol{K_x}$=[5.4008, 11.161, 3648.2].

The feed-forward term $\overline{N}$ is calculated using the following relation:

$$\overline{N} = K_x \cdot \left[-\frac{K_I}{(p(1)-1) \cdot K_x^T} \right]^T \tag{3.34}$$

where $p(1)$ is the first element of the chosen closed loop pole vector $\boldsymbol{p}$ and represents the integrator pole we want to cancel.

The amplifier rectification term is calculated as the inverse of the z-transform in equation (3.17): $U_{in}(z)/U_{amp}(z)$. A numerical saturation, [$-$1V +1V], of the signal fed into the amplifier is finally included for safety reasons.

The Kalman estimator, designed to estimate the whole state vector (and in particular the piston speed signal), receives as inputs the amplifier voltage, the coil current, the piston position and the pressure into the pump, which is considered as a measurable disturbance. As outputs it gives the filtered current and position and the estimated velocity, which is our missing state. The design of the Kalman filter was done by giving the system model in the form of state matrices, and the estimated statistics of disturbance and measurement noise. The disturbance statistics, i.e. the mean square value of the force acting on the piston due to the pressure into the pump chamber, was set to 1.8e3 N^2. The measurements noise statistics were set to, 1.08e-6 A^2 and 4.1e-12 m^2 for current and position respectively. The measurements noise statistics were estimated from the noise floor given by the sensors when the actuator was not moving, whereas the disturbance noise statistics was estimated by simulation.

Once the controller was designed, it was tested on the nonlinear continuous time model of the pump, no load was first connected to the pump, than the complete model of the hydraulic circuit was considered. The controller performed well in both conditions, therefore as a next step it was tested on the physical device to measure its real performances.

To measure the controller preformances a two seconds duration sinusoidal chirp with frequencies sweeping from 0.01 Hz to 100 Hz was chosen as a reference current signal. The pump chamber was filled with water and its inlet and outlet tubes clamped. The load acting on the piston was purely compliant due to some air bubbles left into the chamber. The developed pressure reached during the experiment values up to 150 mmHg. The actual current was measured and the closed-loop ETFE (between reference and measured currents) was determined. Time domain signals are shown in Figure 3.17, whether the calculated ETFE is shown in Figure 3.18.
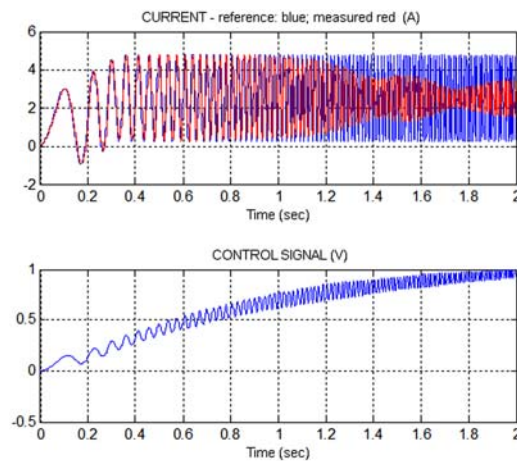
Figure 3.17 – upper panel: reference current (blue) and measured one (red); bottom panel: control signal, i.e. voltage to the amplifier.
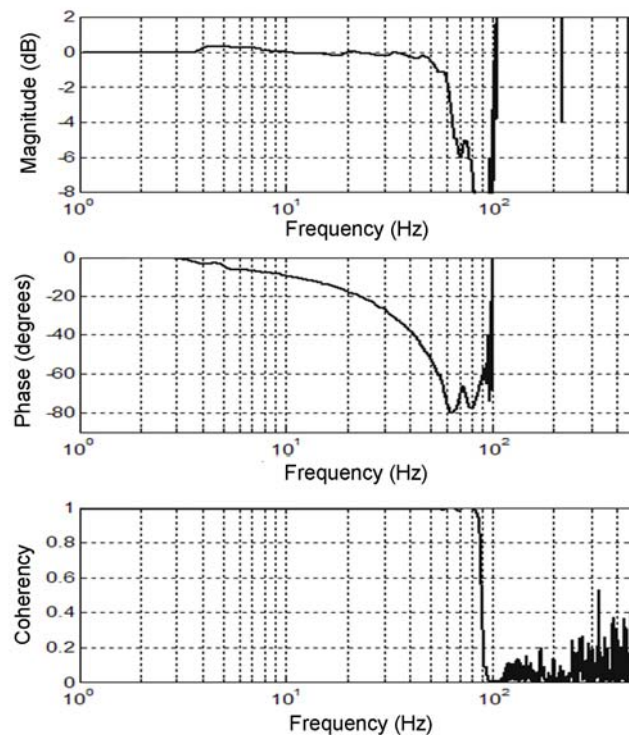
Figure 3.18 – ETFE between the reference and the measured current; upper panel: magnitude; middle panel: phase; bottom panel: coherency spectrum.

As it is shown in the magnitude plot of the closed-loop ETFE (upper panel in Figure 3.18) the bandwidth of the controlled system is of about 65 Hz; the phase plot (middle panel in Figure 3.18) reveals a delay of about 3 msec between the reference current and the measured one; the coherency spectrum (bottom panel in Figure 3.18) shows that we can rely the ETFE up to frequency of 90 Hz.

To control the pressure into the pump chamber an external control loop is added: reference and measured pressure are subtracted, this error is integrated and multiplied by K_p=2, the result of this calculation is the reference current for the actuator.

2.3 VAD Identification: experiments performed

Identification experiments

Twelve different measurement sets of 30 seconds duration were generated for the identification purpose. Each was characterized by different flow-head-speed signal waveforms and magnitudes. This was done to reproduce different hydrodynamic conditions.

Because the clamp resistance was not servo-controlled, a procedure to have repeatable resistance values had to be sought. Once the circuit was filled and pressure preloaded the VAD speed was controlled with a double ramp from the minimum to maximum speed (7500 and 12500 rpm, respectively) and back to minimum speed. The displacement-pump was inactive and the clamp-resistance was adjusted in two different positions in order to have a measured flow ranging from 65 to 125 mL/s and from 100 to 180 mL/s in each position (which we will call high and low resistance, respectively).

For each of the clamp-resistance position the displacement-pump was controlled first in current than in pressure. The current reference was a sinusoid with an amplitude of 1.5 A, bias of 1.5 A and frequency of 2 Hz; this generated a pressure into the pump chamber which was almost sinusoidal. The pressure reference was a square wave with an amplitude of 40 mmHg, bias 60 mmHg and frequency of 0.666 Hz (Figure 3.19a).

For each of the clamp-resistance position and displacement-pump control modality, the VAD speed was subject to three different reference signals: a double ramp from minimum to maximum and back to minimum speed; a 1000 rpm stepwise change from minimum to maximum and back to minimum speed, every 3 seconds; a sinusoid with an amplitude of 2500 rpm, bias of 10000 rpm and three different frequencies 0.05, 0.1 and 0.2 Hz each 10 seconds (Figure 3.19b).

measured displacement-pump pressure

a)

measured VAD speed

b)
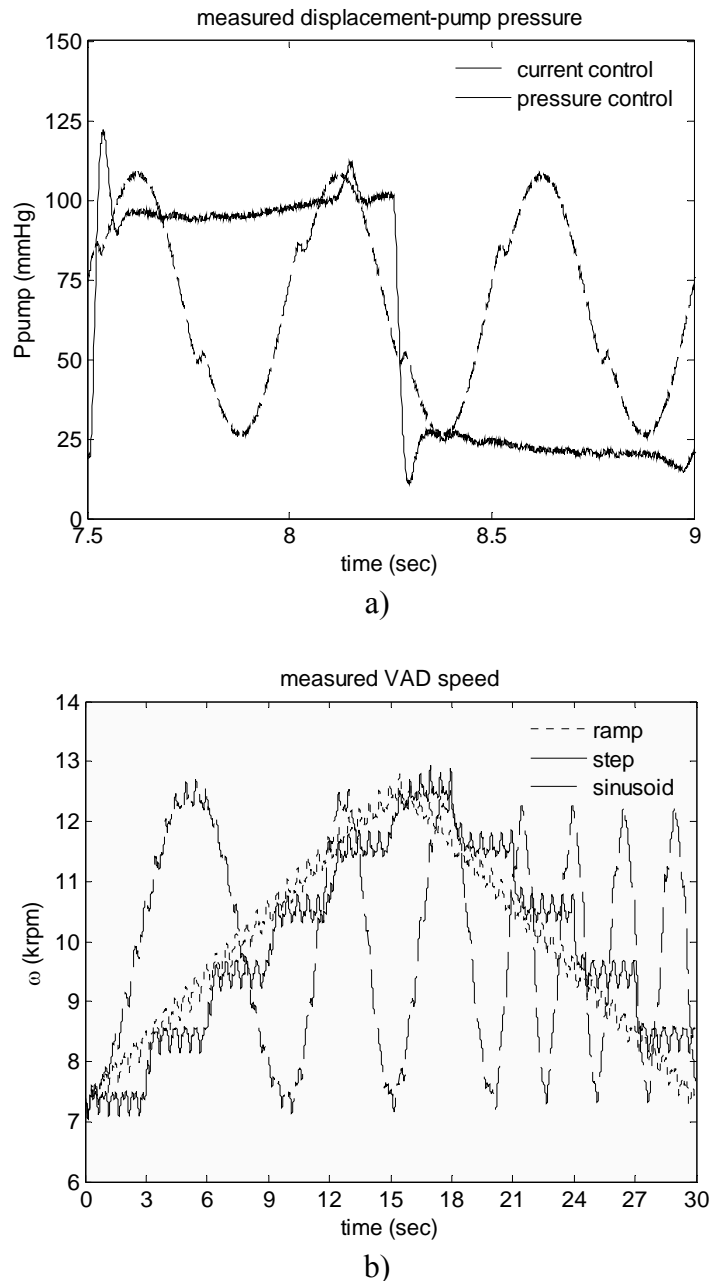
Figure 3.19 – identification datasets signals: a) detail of the measured displacement-pump pressure, when it was current controlled (dashed) and pressure controlled (solid); b) measured VAD speed when was is driven by double ramp (dotted), by steps (solid), by sinusoids of increasing frequency (dashed).

The model structure used for the VAD identification is the following:

$$H(t) = \alpha_\omega \cdot \omega(t)^2 - \left[a \cdot Q_{VAD}(t) + b \cdot Q_{VAD}(t)^2 \right] - L \frac{dQ_{VAD}(t)}{dt} \qquad (3.35)$$

here α_ω represents a VAD speed related parameter, a and b hydraulic resistance parameters, L the fluid inertance parameter, $H(t)$ the pressure head, $\omega(t)$ the rotational speed and $Q_{VAD}(t)$ the VAD flow. This model is modified from the one proposed by (Choi, 1998), that does not have the quadratic term $b*Q_{VAD}(t)^2$. Because all the measurements are sampled

signals, the model represented by equation (3.35) was discretized using the simple forward rule (Franklin et al., 1998, p. 78) thus obtaining:

$$Q_{VAD}(k+1) = \frac{1}{L} \cdot \left[\alpha_\omega \cdot \omega(k)^2 - a \cdot Q_{VAD}(k) - b \cdot Q_{VAD}(k)^2 - H(k) \right] \cdot T_{smp} + Q_{VAD}(k) \quad (3.36)$$

here k goes from 1 to N, that is the number of acquired samples and T_{smp} is the sampling time.

If the measured VAD rotational speed ω, expressed in rad/s, and the measured pressure head H, expressed in mmHg, are feed into equation (3.36), the VAD flow can be calculated. We will indicate this flow with $\hat{Q}_{VAD}(k|\theta)$, where the symbol $^\wedge$ is now used to distinguish it from the measured flow value. This flow depends on θ, the vector of adjustable parameters [L, a, b, α_ω].

The estimated parameter values are the ones that minimize the following norm of the prediction error sequence (Least Square Criterion):

$$V_N(\theta, Z^N) = \frac{1}{N} \sum_{k=1}^{N} \frac{1}{2} \cdot \left[Q_{VAD}(k) - \hat{Q}_{VAD}(k|\theta) \right]^2 \quad (3.37)$$

here Z^N represents the input and output time series, the difference $Q_{VAD}(k) - \hat{Q}_{VAD}(k|\theta)$ is the so called prediction error $e(k)$. The norm $V_N(\theta, Z^N)$ was minimized using the Simplex Search Method. The following values were used to initialize the minimization process: $L_0 = 0.05$ mmHg*s^2/mL, $a_0 = 0.001$ mmHg*s/mL, $b_0 = 0.001$ mmHg*s^2/mL^2, α $\alpha_{\omega 0} = 0.0001$ mmHg*s^2/rad^2. For each of the twelve experimental runs the individual parameter values were identified using this to this method. To measure the estimation result, the root mean square error (RMSE), defined by equation (3.2), was used.

The mean and standard deviation of the 12 identification results for both the parameter values and the RMSEs were calculated.

Validation experiments

A measurement set of 30 seconds duration was generated for the validation purpose. As before the hydraulic circuit was filled with 40% glycerin-water mixture and again pressure preloaded to 80 mmHg, than the clamp resistance was set in order to have a measured flow ranging from 75 to 135 mL/s. The current reference was quasi-white noise test input. In particular an independent sample was drawn, every 0.1 sec, from a random number generator according to a Gaussian probability distribution with mean 1.5 A and standard deviation 0.5 A . These kind of signals are referred to as constant-switching-pace symmetric random signals (Marmarelis, 2004, p. 80).

Figure 3.20 shows a detail of the reference and measured current in the voice coil and the resulting pressure into the displacement-pump. The VAD speed was subject to a 1000 rpm stepwise changing reference signal, from minimum to maximum and back to minimum speed, every 3 seconds. The

mean values of the identified parameters were used in a VAD model represented by equation (3.35), which was simulated using Matlab® Simulink® (solver used: ode23s). The model received as inputs the measured VAD pressure head and speed and gave as output the estimated flow. This was compared to the measured one and the RMSE could be calculated both for the whole experiment and for two seconds subsets, each corresponding to a different rotational speed.
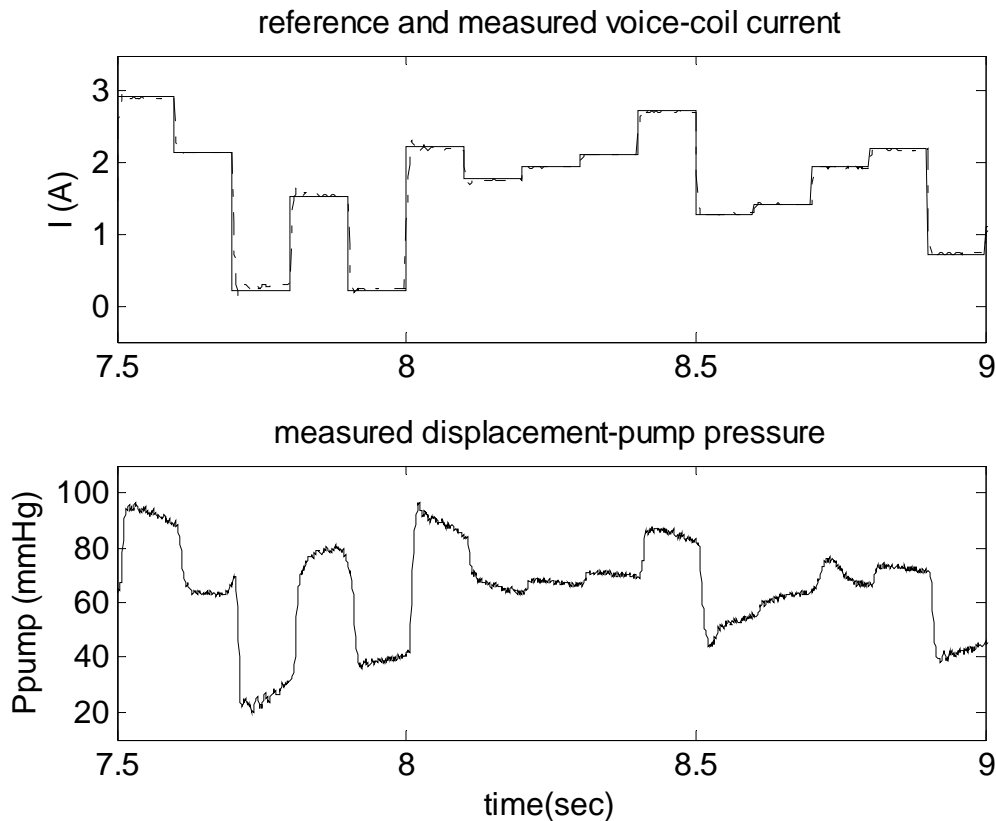
Figure 3.20 – details of the validation dataset signals: (upper panel) reference and measured current into the actuator voice coil, solid and dotted line, respectively; (bottom panel) resulting measured pressure in the displacement-pump.

3 VAD Identification Results and Discussion

Results

In each of the twelve data blocks the estimation process successfully converged. Mean values and standard deviation of the identified parameter are reported in Table 3.4.

Table 3.4: identified parameter values (mean ± standard deviation), n=12.

Parameter	Value	Units
L	0.203 ± 0.035	$mmHg*s^2/mL$
a	0.020 ± 0.001	$mmHg*s/mL$
b	$9.17e\text{-}4 \pm 2.22e\text{-}4$	$mmHg*s^2/mL^2$
α_ω	$8.56e\text{-}5 \pm 0.35e\text{-}5$	$mmHg*s^2/rad^2$

The RMSE for the twelve identification dataset was 6.10±1.10 mL/sec ranging form a minimum of 4.14 mL/s to a maximum of 7.63 mL/sec.

Data used for the validation purposes are shown in Figure 3.21, where it is possible to notice the quasi-white characteristic of the signals. In particular the predicted flow is almost undistinguishable from the measured one, the RMSE being 7.43 mL/sec.
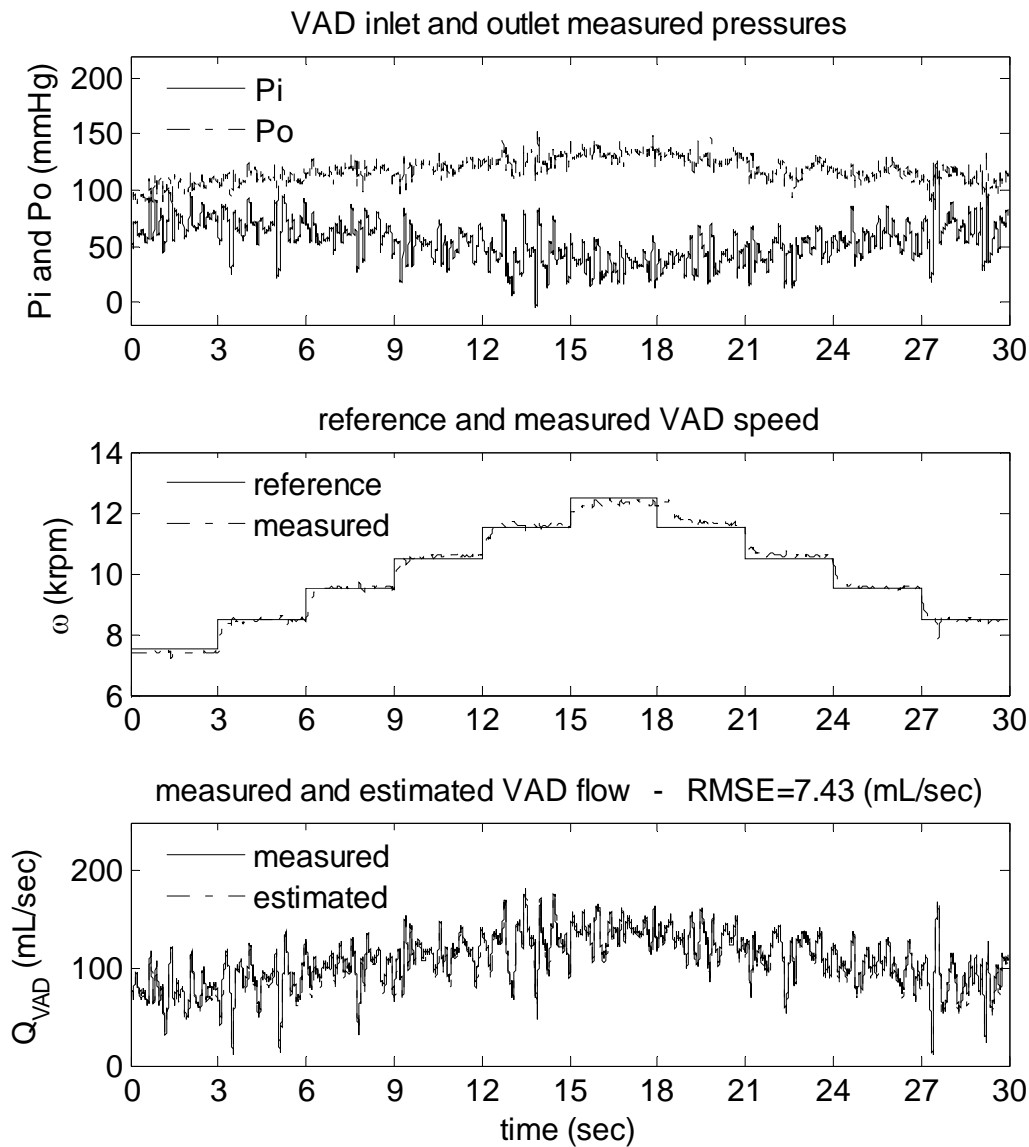
Figure 3.21 – validation dataset signals: (upper panel) pressures measured at the inlet and outlet VAD sections; (middle panel) reference and measured VAD speed; (bottom panel) measured and estimated flow.

A detailed view of the flow signals (Figure 3.22) reveals however some discrepancies, even if not of a big magnitude. The RMSE calculated from the whole validation dataset (7.43 mL/sec) and calculated for each of the two seconds subsets (values shown in Figure 3.22) are of the same order of magnitude of the one obtained from the identification data (6.10 mL/sec),

thus suggesting good predictive ability of the identified model and parameters.
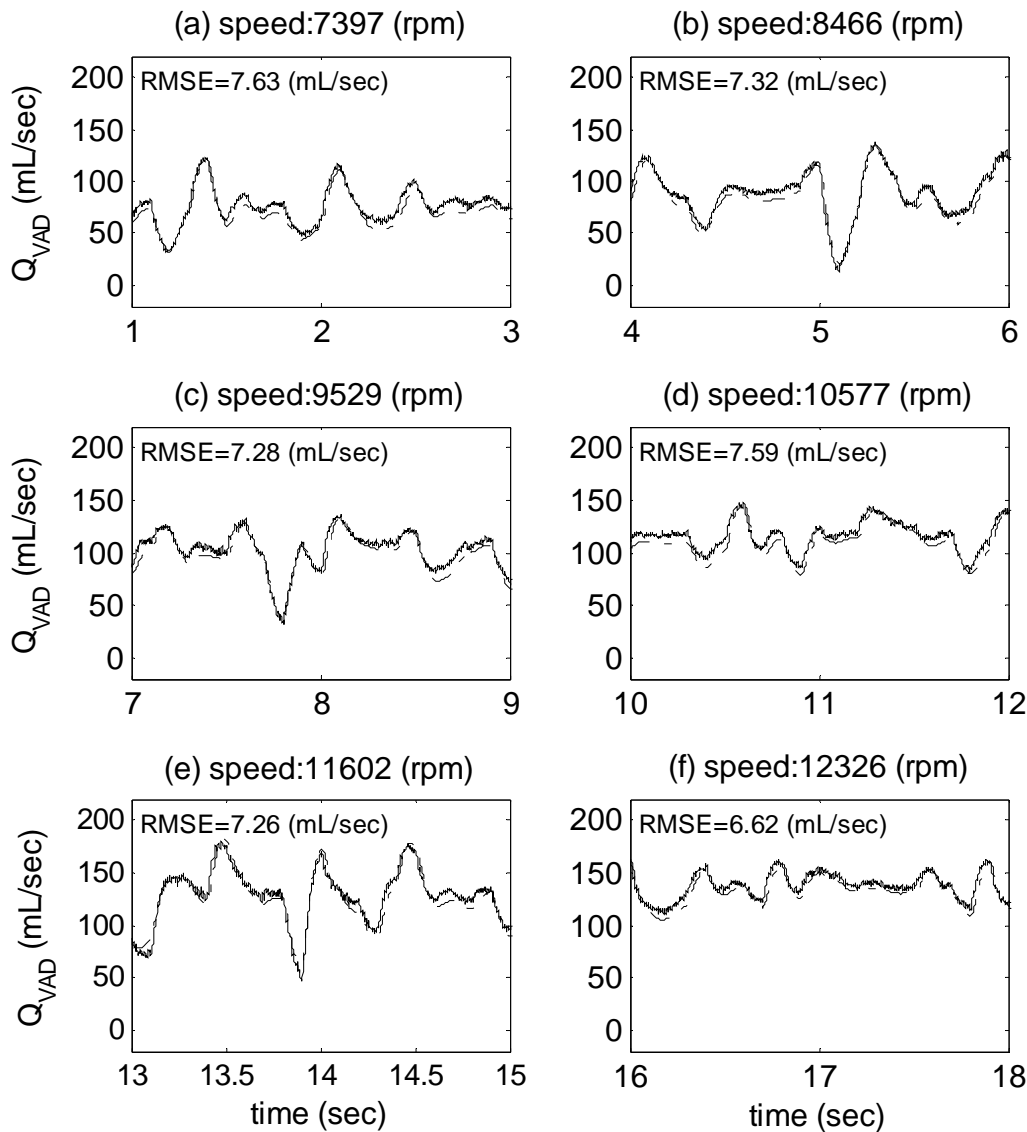
Figure 3.22 – details of measured (solid line) and estimated (dot-dashed line) flow at different VAD speeds (panels from a to f).

Discussion

A hydro-dynamic model of the Micromed-DeBakey VAD® was successfully identified. For the in-vitro configuration used, this model was able to predict the VAD flow, from measurements of the pressure head and rotational speed of the assist device, with a RMSE of about 7 mL/sec. A test bench was used to generate informative identification and validation measurement datasets. The measurements reproduced several hydrodynamic conditions, i.e. various VAD flow-head-speed signal waveforms and magnitudes.

From a careful observation of Figure 3.22, it can be noted that the predicted flow is biased with respect to the measured one. The mean value of the prediction error (i.e. the difference $Q_{VAD}(k) - \hat{Q}_{VAD}(k|\theta)$) being 4.92 mL/sec. If we try to estimate the flow using the mean parameter values increased or decreased by one standard deviation (Table 3.4, we have that the mean prediction error becomes 9.58 or –2.01 mL/sec. Thus we could conclude that the uncertainty of about 10 mL/sec is to be expected.

Certain aspects of the present study should also be noted. The use of glycerin-water mixture instead of blood as working fluid: it is known that haematocrit, and in general blood viscosity, have an impact on the hydrodynamic characteristics of the VAD (Tanaka et al., 2003, Wakisaka et al., 1997). However, as a first step, we decided to use a glycerin-water mixture, mainly because this is easier to handle than blood. The model should be validated with in-vivo measurements, where variation of the viscous property of blood can occur. The modeling of the brushless DC motor was not included into the presented analysis, which would be a next step for the Micromed-DeBakey VAD$^{®}$ identification. However the presented model has already its value, because it allows, when equation (3.36) is properly manipulated, to estimate the pressure head, given the measured flow and speed. Both measurements are available in the clinical setting.

4   Cannulae Identification

To complete the identification of the whole assist device, not only the pump should be modeled, but also the inlet and outlet cannulae. The pump inlet cannula is a rigid titanium tube which connects the ventricle to the pump inlet section. The pump outlet cannula is a Dacron graft which connects the pump outlet section to the aorta. The Dacron graft is a synthetic (manmade) material used to replace normal body tissues. It is made in tubular form usually to replace or repair blood vessels. It causes very few reactions because it is chemically harmless and easily tolerated by the body.

4.1 Outflow graft identification: materials and methods

To perform the identification of the outflow graft two experimental setups were built. Both setups are shown in Figure 3.23. In the first experimental setup, (Figure 3.23a), the graft was placed between two reservoirs with both of its ends open. Pressure was supplied to one reservoir by a pneumatic pressure driver; the other reservoir was partially filled with water and sealed from the atmosphere. The degree of filling of the outlet reservoir was selected to set the rise time in the graft and outlet reservoir at approximately half the period of the driving signal. This arrangement will be termed "open-ended". In the second experimental setup (Figure 3.23b), the outlet of the graft was plugged, i.e. the graft had a

closed-end. This arrangement will be termed "closed-ended". The open-ended setup is shown in Figure 3.24.

a)   b)
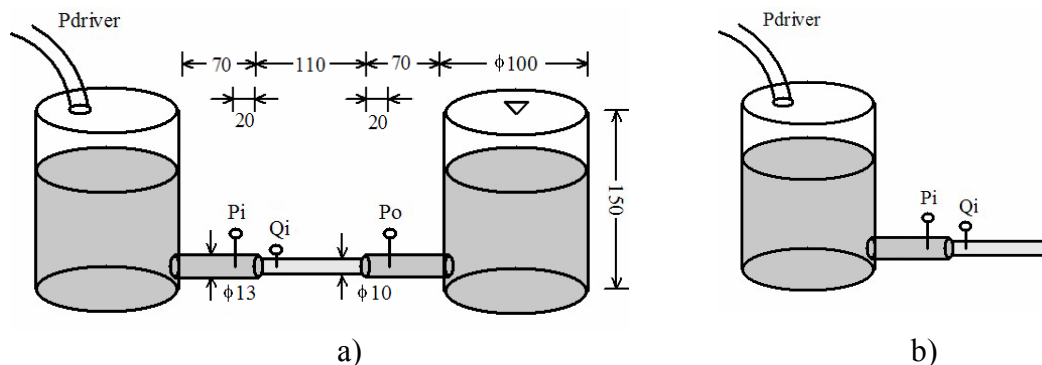
Figure 3.23 – schematic diagrams of the experimental setups: a) graft with both ends open; b) graft with outflow ended closed. *Pi* and *Po* are pressures measured at the inlet and the outlet of the graft. *Qi* is the flow measured at the inlet of the graft. *Pdriver* is the pressure supplied by a pneumatic pressure driver as measured in the first reservoir. Dimensions are in given in (mm).

Pressures were measured at the inlet and the outlet of the graft (*Pi* and *Po* respectively), and in the reservoir connected to the pressure driver (*Pdriver*) by means of disposable pressure transducers (Model TruWave, Edwards Lifesciences, Irvine, CA, USA). Flow (*Qi*) was measured at the inlet of the graft by means of an ultrasonic transducer (Model H11XL, Transonic Systems Inc., Ithaca, NY, USA).
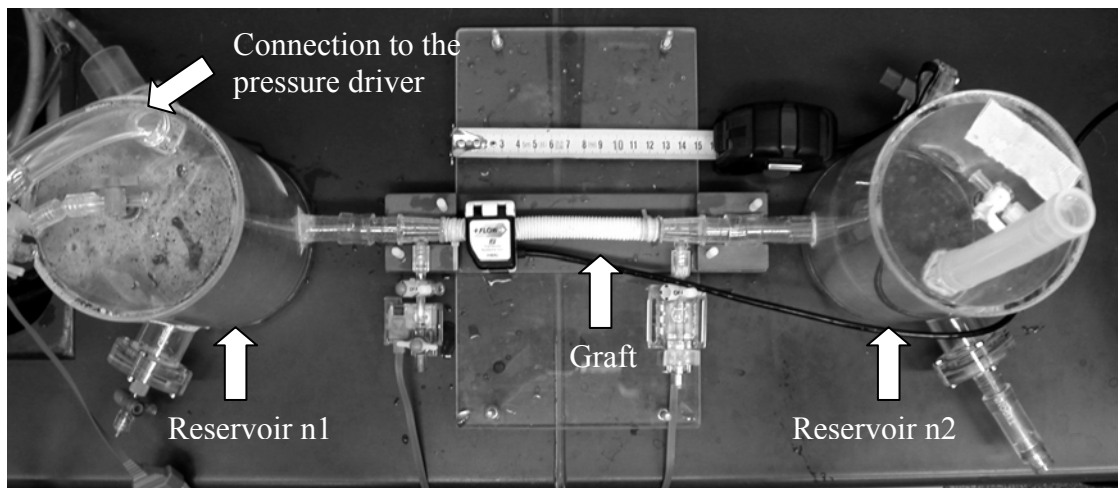
Figure 3.24 – picture of the experimental setup for open-ended setup.

The pneumatic pressure driver was set to impose a square wave on the first reservoir. In practice, the pressure waveform at the graft inlet was never square, due to the compressibility of the air coupled to the fluid inertance of the connector that joined the first reservoir to the graft. These factors limited the bandwidth of the observed signals to 20-30 Hz.

The working fluid does not affect the proposed identification procedure and its validity assessment. Although water does not reproduce the fluid properties of blood, it was used as a working fluid because it is easier to handle than blood or glycerin-water mixtures.

The Dacron graft was highly permeable to water and this fact made measurement practically unrepeatable, especially in the closed-ended setup. To overcome this problem, a thin layer of silicone was placed on the outer surface of the graft. This procedure reduced the leakage, although it slightly stiffened the graft.

A mathematical model of the experimental setup was built and used to generate signals that could be used to test the identification process. The real pressure, as measured in the first reservoir during the experiments, was fed to the mathematical model as the forcing input. The rigid connectors between the reservoirs and the graft were modeled as a series of hydraulic resistance and fluid inertance and the second reservoir was modeled as a pure compliant element (Figure 3.25a). The graft was modeled by means of a transmission line model comprised of eleven Π and T segments, alternatively connected (Figure 3.25b). The segments included fluid resistance, taken to be linearly dependent on the absolute value of the flow, inertance, radial compliance and leakage resistance.
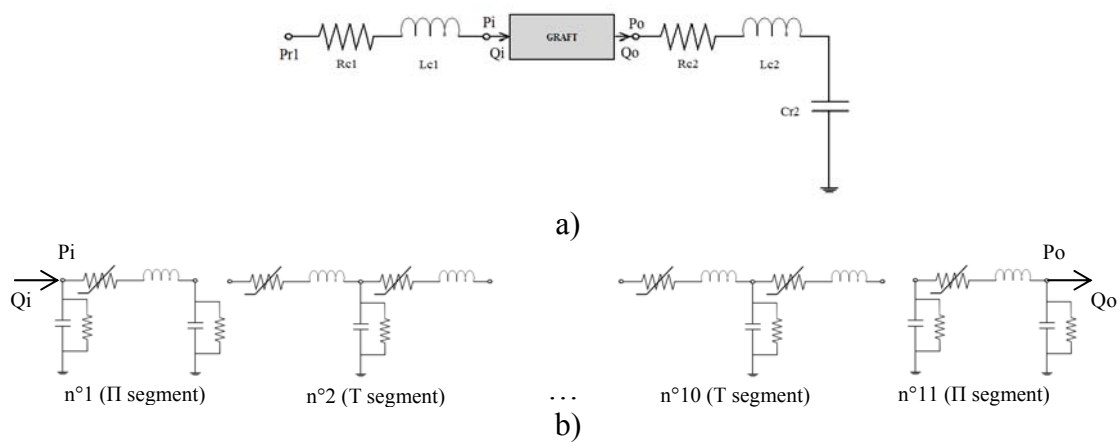
Figure 3.25 – a) electrical analog representation of the open-ended experiment; b) transmission line model of the graft, composed of eleven Π and T segments, connected in alternation.

Chosen values for the hydraulic circuit and graft parameters are reported in Table 3.5. The values of the resistance and inertance in the single segments were chosen so that they summed to the total resistance and inertance (R_{tot} and L_{tot}). The values of the compliance and leakage resistance in the single segments were chosen so that the reciprocal of the sum of their reciprocals equaled the total compliance and leakage resistance (C_{tot} and $Rleak_{tot}$).

Measurement noise was introduced by adding zero-mean Gaussian white noise to the model-generated signals. The white noise power was

chosen in order to match the S/N ratios observed in the open-ended experiments: 49 and 40 dB for the pressure and flow signal respectively. In physical terms, the variances of the modeled noises that led to the measured S/N ratios were 0.1 mmHg^2 and 1 (mL/s)^2.

Table 3.5: parameter values for the modeled hydraulic circuit and graft.

Parameter	Value	Units
$Rc1$ (inlet connector resistance)	0.02	mmHg*s/mL
$Lc1$ (inlet connector inertance)	0.005	mmHg*s^2/mL
$Rc2$ (outlet connector resistance)	0.02	mmHg*s/mL
$Lc2$ (outlet connector inertance)	0.005	mmHg*s^2/mL
$Cr2$ (second reservoir compliance)	0.7	mL/mmHg
R_{tot} (total graft resistance)	$\alpha*|Qi|+\beta$; α=0.0011; β=0.011	mmHg*s/mL
L_{tot} (total graft inertance)	0.012	mmHg*s^2/mL
C_{tot} (total graft compliance)	0.003	mL/mmHg
$Rleak_{tot}$ (total graft leak resistance)	100	mmHg*s/mL
n (number of graft segments)	11 (6 Π and 5 T segments)	–

The pressure driver delivered a quasi-square wave with minimum and maximum values of 20 and 120 mmHg or 40 and 120 mmHg respectively. Its frequency was varied over a range of 30 to 140 bpm (0.5 to 2.33 Hz). 25 experimental runs for the open-ended setup and 15 for the closed-ended setup were generated by varying the frequency. In addition, two continuous run were generated for the both open-ended and closed-ended setups. Here the driving pressure frequency was varied stepwise, every 40 seconds, from 30 bpm to 140 bpm and then back to 30 bpm. This generated a chirp-like signal with power spread over a broader spectrum. These data were used for the Empirical Transfer Function Estimate (ETFE, see paragraph 2.1 in this chapter) and for the final model validation, respectively. For the open-ended setup the input signal to the system was the pressure drop across the graft ($Pi–Po$) and the measured output was the flow (Qi), whereas for the closed-ended setup, the input was the flow (Qi), and the output was the pressure at the inlet section (Pi).

Thus two ETFE were calculated. In both cases a fast Fourier transformation using 2^{15} points was applied to the signals. A Hanning window whose width was 2^{10} samples was used to section the signals, with an overlap of 2^9 samples. From the smoothed ETFE, thus obtained, the dc-gain, cutoff frequency, high-frequency roll-off and phase shift were derived. From these quantities, the model structure and a first raw estimation of its parameters could be inferred.

Two Extended Kalman Filters (EKFs, see paragraph 2.1 in this chapter) were subsequently designed for the open-ended and closed-ended setups in order to identify the model parameters. The EKFs were first applied to the model-generated data that mimicked the 25 plus 15 experimental runs. This was done because the initialization of the EKF must be accomplished by a

trial and error procedure and performing this operation first on the model-generated data simplified the initialization of the EKFs for the physical experiment. Mean and standard deviation for the parameter estimates were obtained, and the percent errors with respect to the true model values were calculated. Once satisfactory results were obtained on the model-generated data, the EKFs were applied to the physical results and parameter values were obtained for each experimental run. Means and standard deviations for the parameter estimates were also calculated.

As a final step the model was validated using a cross-validation data set. In particular, for the graft operated in the open-ended setup, three different models were evaluated. The first and the simplest comprised a resistance and inertance connected in series. The hydraulic resistance was assumed to be constant and equal to the calculated RMS value of the identified time-varying resistance. The second comprised also a resistance and inertance connected in series, but with the resistance linearly dependent on flow. The last comprised a single T segment with a series of flow-dependent resistances and an inertance on each side of the T, and, between, a parallel branch of compliance and leakage resistances. The input to each model was the pressure drop across the graft and the output was the model-generated flow, which was compared with the physical measurement. For each model %VAF was calculated to obtain a measure of its prediction ability.

All signals were acquired with a sampling period of 0.003 sec at a resolution of 16 bits, using a dSpace^{TM} DS1103 signal-processor system. Computations were performed with the Signal Processing Toolbox from Matlab$^{\circledR}$. The whole hydraulic setup was numerically simulated with Matlab$^{\circledR}$-Simulink$^{\circledR}$ (solver ode23s).

4.2 Outflow graft identification: results and discussion

Results

Transfer function estimates for both the open-ended and the closed-ended setups show a low-pass characteristic, with a high-frequency roll-off of 20 dB/decade. The ETFE and coherency spectra are shown in Figure 3.26.

These results suggest that the underlying transfer function is first order for both cases. The model structure selected for the graft in the open-ended setup was a series of a fluid resistance and inertance, with resistance allowed to be either constant or flow-dependent (Figure 3.27a). The term β represents the resistance at zero flow. Although from a physical point of view it would have made sense to set it equal to zero, this term was included, thus representing an analogous of Coulomb or static friction term. It can be also be seen as a term which represents concentrated losses that does not depend on flow. The model structure selected for the graft in the

closed-ended setup was a parallel combination of compliance and leakage resistance (Figure 3.27b).

The dc-gain and the cutoff frequency of the ETFE give raw information on the magnitude of these parameters.

The coherency spectrum permits estimation of the bandwidth of the signals, and the frequency range in which the ETFEs can consequently be trusted: up to 20 Hz for the open-ended and 40 Hz for the closed-ended setup. This bandwidth limitation arises mainly from the pneumatic actuator. However the bandwidths were sufficient because signals into the cardiovascular system have little power at frequencies higher that 20-30 Hz. For the identification task itself, this bandwidth limitation means that every model feature that affects only frequencies beyond these limits cannot be identified.

(a)   (b)
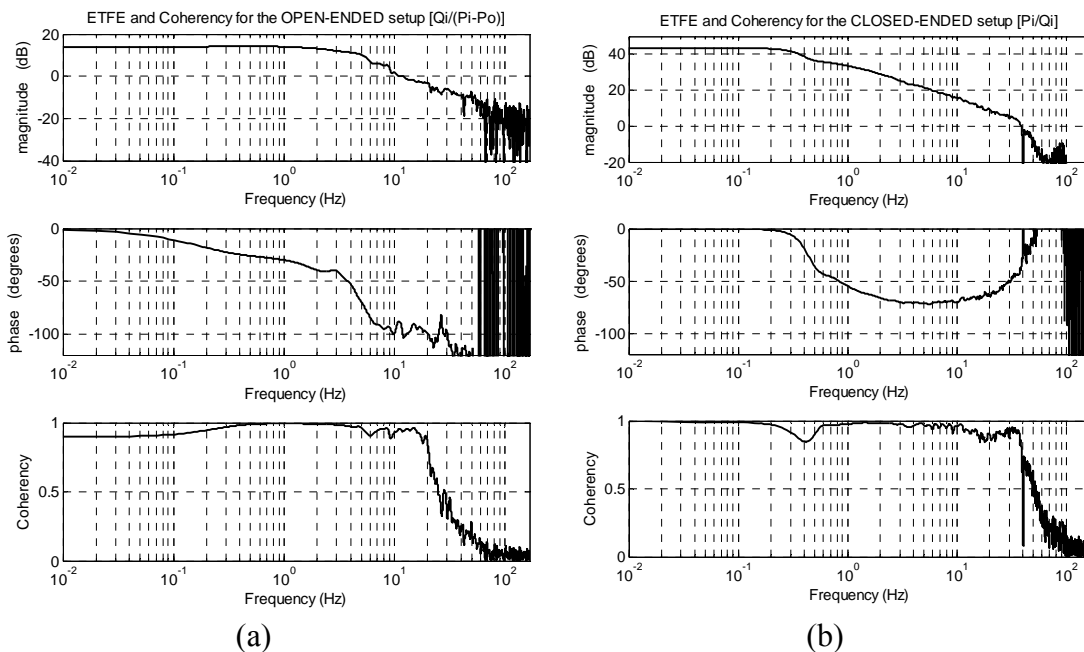
Figure 3.26 – (a) graft ETFE in open-ended setup between the pressure drop (*Pi-Po*) and flow (*Qi*); (b) graft ETFE for in closed-ended setup between flow (*Qi*) and inlet pressure (*Pi*). In the upper and middle panels the magnitude and phase are displayed; in the bottom one the coherency spectrum is displayed.

(a)   (b)
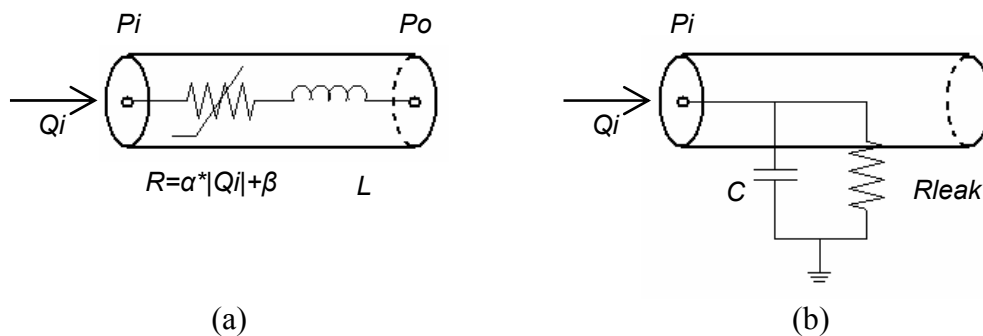
Figure 3.27 – lumped parameter model structure for the graft in the open-ended (a) and closed-ended (b) setup.

Once the model structures were defined, the EKF for the open-ended setup identified the time-variant hydraulic resistance and the fluid inertia. The EKF for the closed-ended setup identified the leakage resistance and the radial graft compliance.

Figure 3.28 shows results of the EKF identification applied to the model-generated data for the open-ended and closed-ended setups. The identified parameters are compared to the values used in constructing the model.

To obtain the relation between fluid resistance and flow, we plotted the time-varying resistance (solid line in Figure 3.28b) as a function of the absolute value of flow (dotted line in Figure 3.28a) and performed a linear regression on these data.

Comparison of the estimated flow dependent resistance with that of the model, over one cycle, is shown in Figure 3.29. Data corresponding to flows less than 30 mL/s were not included in the figure, because the EKF was not able to track the hydraulic resistance with sufficient accuracy in this flow range. The EKF performances greatly decrease at such low flow values due to ill-conditioning of the data. It is easy, in fact, to obtain incorrect values of resistance from a flow which is close to zero. Furthermore it have perhaps no sense to identify the value of flow-resistance when the flow is zero.

The parameter values, identified over the 25 open-ended and the 15 closed-ended trials, were averaged and compared to the prescribed model values. They are reported in Table 3.6. The 82% error in β estimation is caused by the poor identification of hydraulic resistance at low flow values.

Table 3.6: outflow graft parameters estimated from model-generated data (Mean±SD) compared with the prescribed model parameters. Percent error is defined as the difference between the identified and model values over the model value of the parameter multiplied by 100.

Open-ended(n=25)	Identified value	SD/Mean*100	Model Value	% error
α (mmHg*s^2/mL^2)	(1.07±0.036)e-3	3.3	1.11e-3	-3.6
β (mmHg*s/mL)	0.020±0.0057	28.5	0.011	81.8
L (mmHg*s^2/mL)	(1.18±0.036)e-2	3.0	1.20e-2	-1.7
Closed-ended (n=15)				
C (mL/mmHg)	(3.07±0.028)e-3	0.9	3.00e-3	2.3
R_{leak} (mmHg*s/mL)	97.5±1.1	1.1	100.0	-2.5
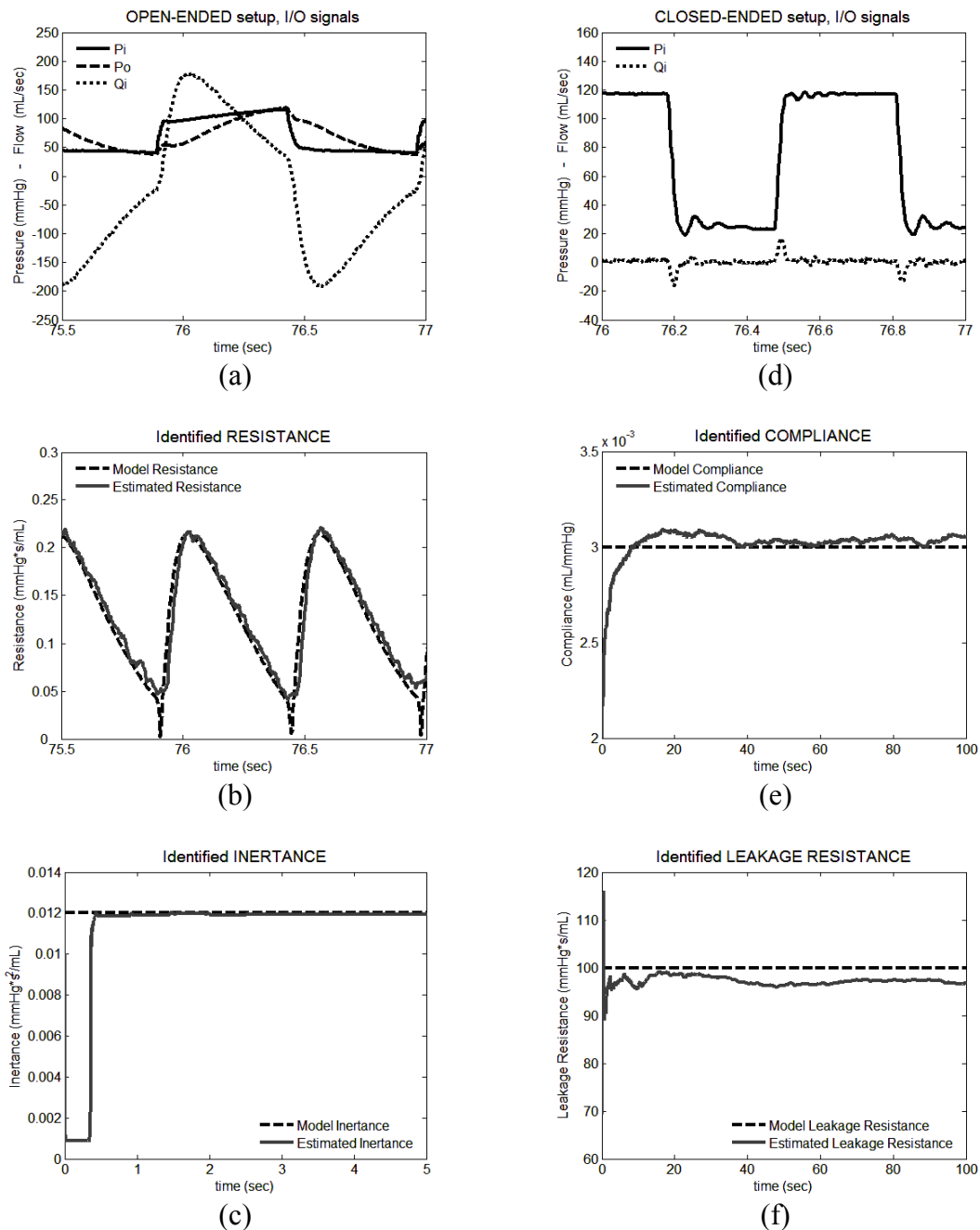
Figure 3.28 – model generated data and EKF results. In the open-ended setup: a) pressure at the inlet and the outlet of the graft (*Pi* and *Po*) and flow at the inlet (*Qi*); b) true model and identification of the estimated resistance (detail of the parameter tracking); c) true model and identification of the estimated inertance (the fist five seconds are displayed). In the closed-ended setup: d) pressure and flow at the graft inlet (*Pi* and *Qi*); e) true model and estimated compliance identification; f) true model and estimated leakage resistance identification are displayed.
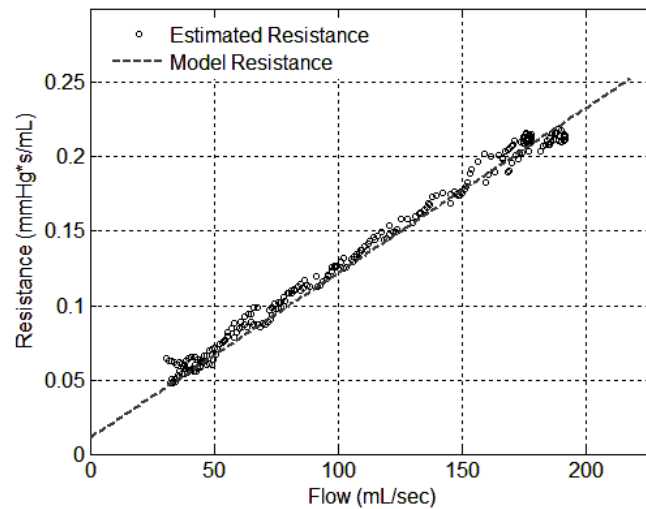
Figure 3.29 – estimated fluid resistance as a function of flow (dots) in one cycle, compared to the model fluid resistance (dashed line).

The same procedure was repeated with the measurements obtained from the actual graft. The parameter values obtained are shown in Table 3.7, together with the percentage ratio between the standard deviation and the mean value.

Table 3.7: outflow graft parameters estimated from real data (Mean±SD).

Open-ended (n=25):	Identified value	SD/Mean*100
α (mmHg*s^2/mL^2)	(1.04±0.028)e-3	2.7
β (mmHg*s/mL)	0.020±0.0033	16.5
L (mmHg*s^2/mL)	(1.20±0.024)e-2	2.0
Closed-ended (n=15):	Identified value	SD/Mean*100
C (mL/mmHg)	(2.98±0.43)e-3	14.6
R_{leak} (mmHg*s/mL)	113.2±12.3	10.9

The % VAF evaluated for the RL model with R constant was 93.8%, those for the RL model with R=f(Q) was 99.1%, those for the model comprising R, L, $Rleak$ and C with R=f(Q) was 99.2.

Discussion

The identification approach proposed here yields reliable estimates and confidence limits for the parameters of the models tested. An important step in this approach is the nonparametric analysis that defines the frequency domain identifiability. This is easily evaluated by the coherency spectrum. Parameters which exhibit their effects in a frequency region where the coherency spectrum has a low value cannot be estimated, neither accurately nor even at all. The nonparametric analysis guides the investigator through model structure definition and eventually leads to model reduction.

For example, in the proposed graft identification, it would have made no sense to use a complex dynamic model (more complex than the lumped RL series, with a flow dependent hydraulic resistance) because signals had no frequency content beyond 20-30 Hz. Therefore the simple RL model economically reproduced the first-order features of the real measurements, as confirmed by the %VAF results. Introduction of the dependence of flow resistance on flow-rate improved the accuracy of the model (%VAF from 93.8% to 99.1%), whereas adding the compliance and the leakage resistance did not meaningfully improve accuracy (%VAF from 99.1% to 99.2%). The combined effects of fluid inertance and graft compliance lead to a resonant frequency of about 25 Hz, where the signal power was already significantly diminished.

The deviation of the phase angle in Figure 3.26 a from the expected first-order form is probably due to the nonlinear nature of the loss attributable to hydraulic resistance. This explanation is supported by the fact that the flow regimen is turbulent and non-stationary, making the fluid resistance flow dependent. Performing the ETFE on model-generated data, with a flow-dependent hydraulic resistance, gave an estimated transfer function with similar phase distortion.

The parametric identification performed on the model-generated data shows that reliable information of the inertance, compliance and leakage resistance parameters can be obtained. They show a small error with respect to the true values with a maximum error of 2.5%. The estimate of hydraulic resistance parameter β is poorly estimated at low flow values with an error of 81.8% of the constant term. The estimate improves at flow rates higher than 30 mL/s, where the slope parameter α that relates flow and hydraulic resistance is identified with an error of only 3.6%.

The identification of parameters from the data generated in the real measurement was evaluated in the light of the model results. The real data identification yielded a high standard deviation in the estimates of compliance, leakage resistance and resistance term β (Table 3.7). This is probably due to the small flows observed in the closed-ended setup (with peaks of only 20 mL/s). These values introduce uncertainty into the calculations and probably also affect the EFTE for the closed-ended setup (Figure 3.26b). Here the cut-off frequency, which is related to the product of compliance and leakage resistance, is not well defined and the coherency spectrum shows a dip. Reference (Ljung, 1998, p. 267) demonstrates a direct relationship between the ETFE and parametric prediction error methods. In fact, the prediction error methods can be seen as methods of fitting the ETFE to the model transfer function with a weighted norm, corresponding to the model signal-to-noise ratio at the frequency in question. The other graft parameters identified (inertance and resistance term α) show small standard deviations (Table 3.7).

In summary, for the proposed example, a simple RL model, with a flow-dependent resistance, is sufficient to represent the graft for signals frequencies up to 20-30 Hz. The compliant and leakage terms could be included into the model but without meaningful improvement. One must ask whether the identified parameters for compliance and leakage have any physical meaning. The fact that both show higher standard deviations (around 10 to 15 % of their mean values) suggests that the values represent just numbers adjusted by the EKF to make, every time, the model prediction fit the measurements. The latter showed poor information content, as evidenced by the ETFE and the coherency spectrum (Figure 3.26b).

4.3 Inflow cannula identification

For the identification of the inflow cannula a similar procedure was used. Because this is a rigid titanium cannula, the only model structure considered was the series between the resistance ($R = \alpha^*|Qi| + \beta$) and the inertance (L) terms (see Figure 3.27a for the electric analog model). Furthermore because the identification of the α term, that makes the resistance proportional to the flow, did not bring significant results, it was discarded. Identification results, which comes from the same open-ended experiment protocol used for the outflow graft, are displayed in Table 3.8.

Table 3.8: inflow cannula parameters estimated from real data (Mean±SD).

Open-ended (n=25):	Identified value	SD/Mean*100
β (mmHg*s/mL)	(0. 15±0. 05)e-2	33.3
L (mmHg*s^2/mL)	(0.99±0.062)e-2	6.2

5 Conclusions

A promising approach for the identification and modeling of cardiac assist devices was successfully applied to the modeling and identification of an axial flow blood pump (MicroMed-DeBakey VAD®). The procedures and advanced mathematical techniques used for identification and validation were presented step by step to illustrate choices, pitfalls, and results from initial problem definition, through model selection and experimental design, on to actual estimates of model parameters. Furthermore methods for the identification and control of components in mock circuits for the experimental design of identification campaign was presented.

*Chapter 4**

In-vivo investigation of VAD-cardiovascular system interaction: left ventricular pressure volume loop analysis during continuous cardiac assist in acute animal trials.

For better understanding of the interaction between left ventricle and axial flow VAD (MicroMed-DeBakey VAD$^{®}$) the effect of different working conditions and support levels on left ventricular pressure volume loop was investigated in acute animal experiments. Measurements of hemodynamic variables were taken at various pump support levels. Each pump condition was studied for different heart rates, central venous pressures and under pharmacologically altered contractility. Pressure volume loop analysis in continuous cardiac assist reveals that the end systolic volume and the diastolic volume are strongly correlated and that end systolic volume varies considerably with preload. Cardiac output becomes slightly dependent on end diastolic volume, which may be due to autoregulatory mechanisms.

1 Introduction

Understanding the interaction between the cardiovascular system and the left ventricular assist device (LVAD) represents an important challenge to the design of better strategies for device control and weaning. When an implanted pump takes over at least partially the function of an impaired left ventricle (LV) and restores normal blood flow, it not only affect the ventricle, but interacts with the whole cardiovascular system and its correlated biological feedback loops. Analysis of this interaction is often conducted by means of computer models that are validated with data from clinical and animal trials, or the literature (Colacino et al., 2007, Schima et al., 2004, Vollkron et al., 2002), or by means of online estimates of cardiac function and vascular parameters (Kikugawa, 2000, Yoshizawa et al., 1997, Yu et al., 1998, Yu et al., 2001). Nonetheless the effect of different left ventricular working conditions and autoregulatory mechanisms on the pressure-volume (PV) loop and LV volumetric dynamics during cardiac assist is not entirely clear.

Aim of the study presented in this chapter was to determine the effect of different working conditions and support levels on the left ventricle.

In section 2 the animal experiments protocol and the tools used to analyze the recorded hemodynamic variables are described. In section 3 results of this analyze are presented and discussed. In section 4 conclusions are presented.

2 Materials and methods

Experimental protocol

A MicroMed-DeBakey VAD® was implanted in seven healthy sheep (102±20 Kg) in acute experiments (Figure 4.1). The sheep were instrumented with ultrasound flow probes to measure pulmonary artery flow (Q_{pulm}), coronary artery flow (Q_{cor}) and pump flow (Q_{pump}); fluid-filled pressure catheters to measure central venous pressure (CVP), pulmonary arterial pressure (PAP), left atrial pressure (LAP), and aortic pressure (AoP); a pressure tip-catheter to measure left ventricular pressure (LVP); and a conductance catheter (CD Leycom, Zoetermeer, The Netherlands) to measure left ventricular volume (LVV).

Data were measured with the graft clamped, which corresponds to a condition of no pump; as well as on minimum, medium, and maximum pump support, obtained by running the pump at different mean pump flows (3.7±0.8, 4.7±1.0 and 5.4±1.3 L/min respectively); and, finally, in pump-off condition, which allowed backflow into the left ventricle. Each pump condition was studied for different heart rates, obtained by pacing the heart over a range of 90 – 130 bpm; different central venous pressures, obtained by infusion of NaCl solution (until the central venous pressure at the

clamped graft increased by 5±3 mmHg from basal conditions); and over a range of pharmacologically altered contractilities, obtained by administration of isoptin or noradrenalin (until the end systolic pressure at the clamped graft decreased by 15±6 mmHg, or increased by 16±12 mmHg, both with respect to basal conditions). In aggregate, these hemodynamic conditions generated, for the seven sheep, 200 sets of steady-state measurements, each set characterized by different pump support level, heart rate, central venous pressure, and pharmacological intervention.

(a)   (b)
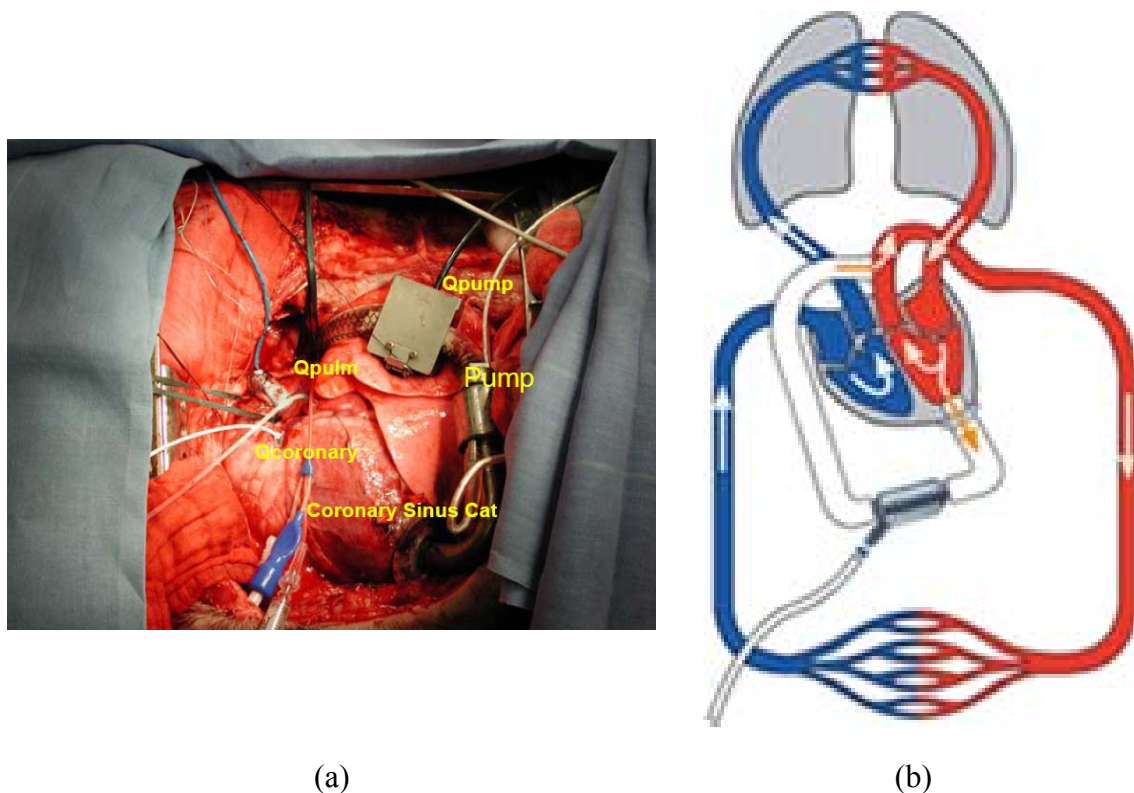
Figure 4.1 – (a) operational situs; (b) axial flow VAD connection schema[7].

Subsets of twenty seconds duration were selected from within the steady-state measurements using a developed graphic-user-interface (GUI), based on the Matlab® 7.1 computing language (The MathWorks, Natick, MA, United States). Each data subset contained from 30 to 40 cardiac cycles, which were averaged to construct a representative steady-state beat. All signals were acquired at a sampling frequency of 100 Hz and a resolution of 16 bits, using a dSpace™ Signal-processor system (dSpace, Paderborn, Germany).

The ventricular volume measurement was corrected by a dimensionless slope factor ($1/\alpha$) and a parallel conductance volume offset (Vc). The equation used to calibrate the conductance measurement was:

---

[7] http://www.berlinheart.de/deutsch/patienten/INCOR/das_system/. Accessed November 28, 2007

$$LVV = \frac{1}{\alpha} \cdot \rho \cdot L^2 \cdot G - Vc \qquad\qquad (4.1)$$

Here ρ represents the blood resistivity, L the inter-electrode distance, G the conductance due to the blood into the left ventricle. Vc is equal to parallel conductance (Gp) multiplied by $(1/\alpha)*\rho*L^2$. The factor $1/\alpha$ was estimated using a regression of stroke volume from the pulmonary artery flow probe against stroke volume from the conductance catheter, while flow was prevented from passing through the LVAD by clamping the graft. The factor $1/\alpha$ was reassessed many times during the experiment, for each clamped-graft protocol step. The average value through the whole experiment was used for the left ventricular volume calibration. The parallel conductance volume (Vc) was estimated as the intercept with the volume axis of a linear regression through end-diastolic PV points obtained from the different experimental protocol steps. The Vc was assumed to be constant throughout the experiments. The blood resistivity ρ was measured for each animal at the beginning of the experiment and after the saline infusion, performed to increase the central venous pressure. It was not possible to asses the parallel conductance Gp.

This Vc estimation assumes a linear EDPVR in the considered ventricular volume range and an arbitrary intercept of the EDVPR with the volume axis at 40 mL. The first assumption was checked by performing a linear regression through the end-diastolic PV points obtained in each of the different experimental protocol steps, and by observation of the distribution of the residuals (Lilliefors test and normal plot). The second assumption was based on the fact that the ESPVR and the EDPVR intercept the volume axis at two different volumes. The difference between these two volumes is called the LV suction volume (Suga et al., 1988). In a few cases of high support, left ventricular pressures dropped below 0 mmHg and the ventricular volume continued to decrease, during systole by 30 mL.

Graphic User Interface

A screenshot of the GUI is shown in Figure 4.2. It comprises two main parts: one for the analysis of the hemodynamic variables in all the sheep (numbers 1, 2 and 3 in Figure 4.2), the other for the examination of the waveforms details in a single sheep and specific working condition (numbers 4 and 5 in Figure 4.2).

To analyze the mean values of the hemodynamic variables it is possible to select the protocol step (see number 1 in Figure 4.2, here "1a" represent the baseline condition) and then the assist levels we want to compare for the specific protocol step, in the displayed case the clamped graft, minimum, and maximum support levels and backflow are compared. For the selected working conditions it is possible to compare the mean value of a hemodynamic variable of interest, in the displayed case the left atrial

pressure (number 2 in Figure 4.2). Results can be plotted either in absolute values or percent variations with respect to the clamped graft condition (number 3 in Figure 4.2). It is possible to display on this plot both individual sheep values or the box plots. A Matlab figure can be outputted.
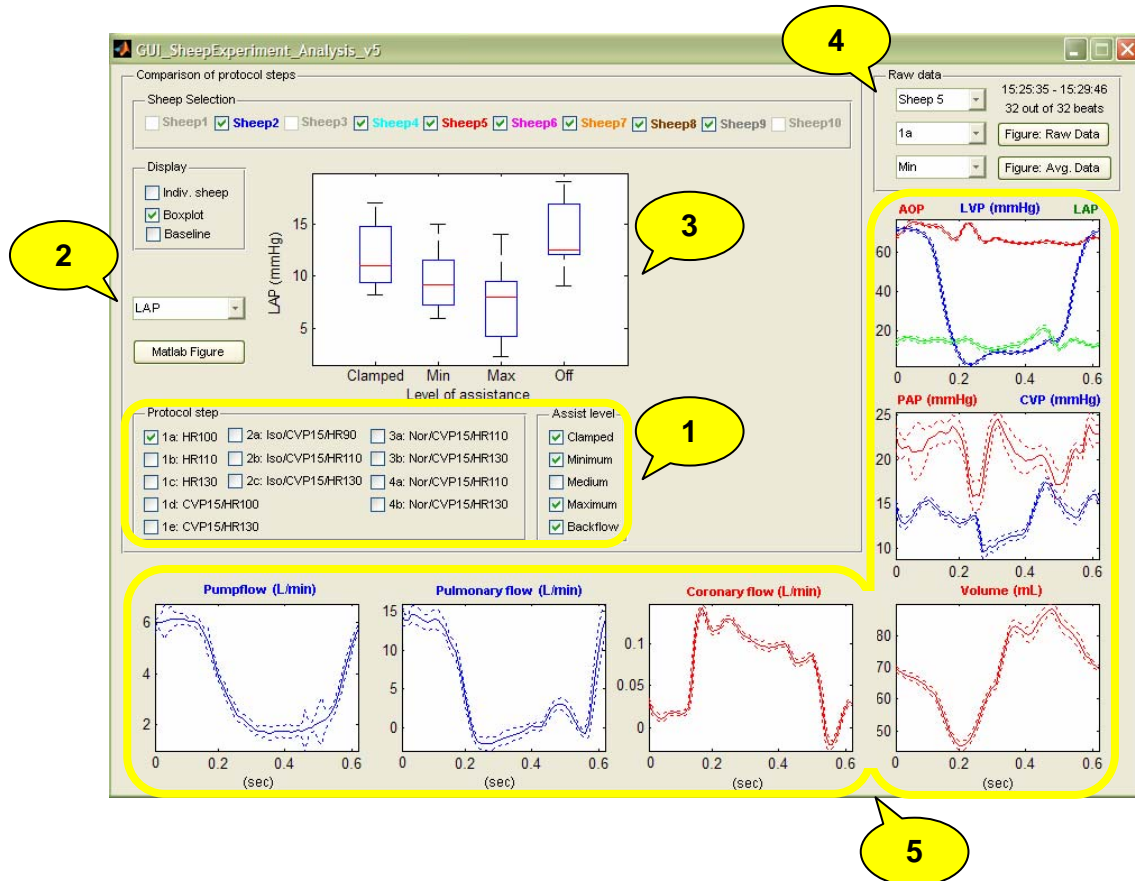
Figure 4.2 – screenshot of the used GUI. See text for numbers description.

To examine the signal waveforms in a single sheep and under particular working conditions, it is possible to select the identification number for the sheep, the protocol step and the support level (number 4 in Figure 4.2), the corresponding signals of the average steady-state beat are then plotted. A beat detection algorithm excludes the arrhythmic beats from the average calculation (in the displayed case none of the 32 beats in the 20 sec window was excluded). Solid lines represent the signal averages, dotted lines are ±1 standard deviation (number 5 in Figure 4.2). Two Matlab figures can be outputted: the 20 sec raw data (Figure 4.3), and the averaged steady-state beat plots (Figure 4.4).

Along with the plots, simple calculations of the mean values of the hemodynamic signals, the elastance curve [E(t)=LVP(t)/LVV(t)], ejection fraction (EF=100*SV/EDV), peak rate of left ventricular pressure rise (dP/dtmax), left ventricle potential energy (PE), external work (EW) and pressure volume area (PVA=EP+EW) are displayed.

Figure 4.3 – twenty seconds raw data used for the average steady-state beat calculation.
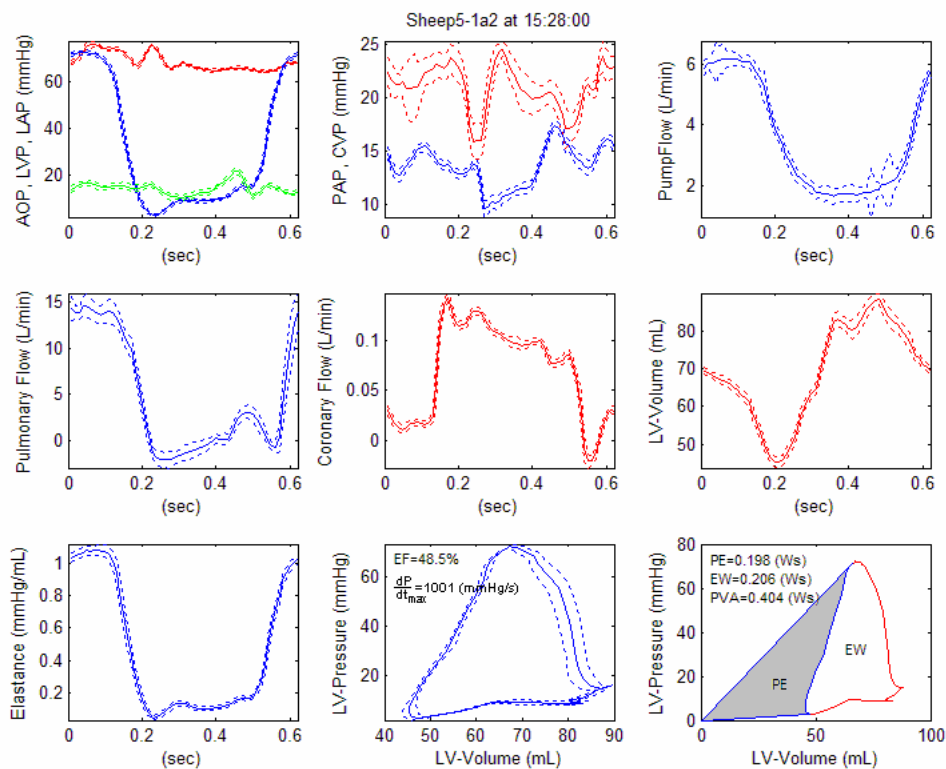
Figure 4.4– average steady-state beat calculation; solid lines represent the signal averages, dotted lines are ±1 standard deviation

Theoretical considerations on the PVloop analysis

The analysis of LV volumetric dynamics and, in general, of the left ventricle interaction with preload and afterload in the PV plane can be simplified by some definitions and assumptions.

The end diastolic volume (EDV) is determined by the end diastolic pressure (EDP) and the end diastolic pressure-volume relationship (EDPVR). The e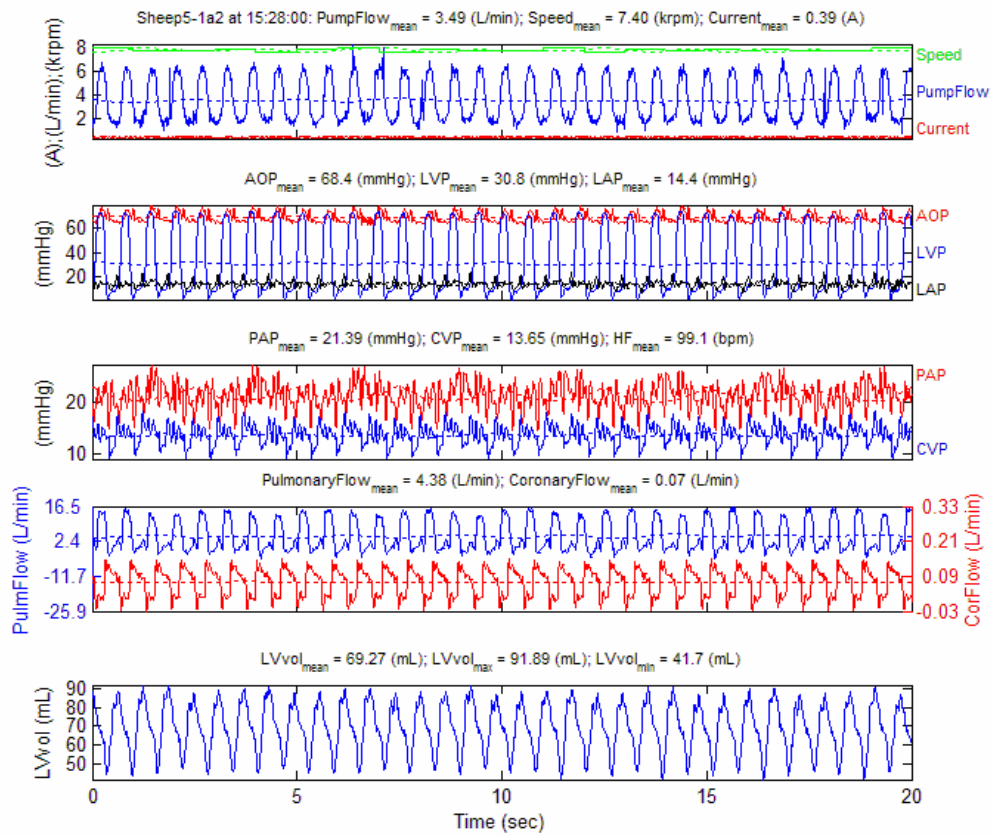nd systolic volume (ESV) is determined by the end systolic pressure (ESP) and the end systolic pressure-volume relationship (ESPVR). The SV is the difference between EDV and ESV (Figure 4.5).
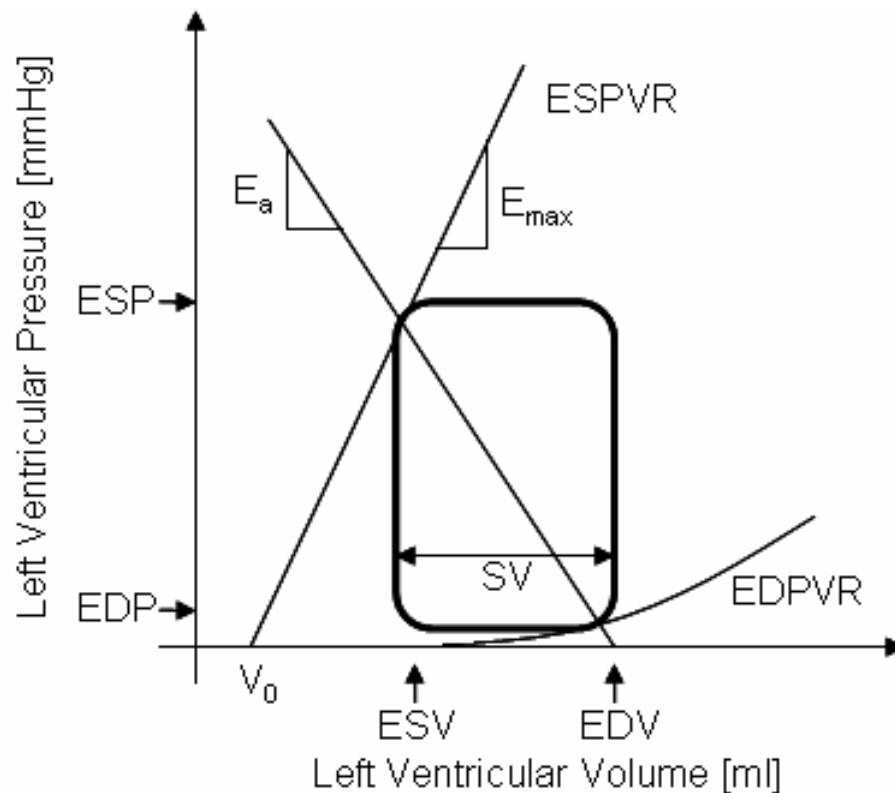
Figure 4.5 – left ventricular pressure volume loop[8]; ESP: end systolic pressure; EDP: end diastolic pressure; ESV: end systolic volume; EDV: end diastolic volume; SV: stroke volume; ESPVR: end systolic pressure volume relationship; EDPVR: end diastolic pressure volume relationship; E_a: effective arterial elastance; E_{max}: maximum elastance; V_0: intercept of the ESPVR with the volume axis.

The slope of the ESPVR, E_{max}, is an index of ventricular contractility, and it is defined by the ratio: $E_{max}=ESP/(EDV-V_0)$. The slope of the ESP – SV relationship is called effective arterial elastance ($E_a=ESP/SV$) and is equal, if ESP is allowed to approximate mean arterial pressure, to the product of heart rate (HR) and systemic vascular resistance (SVR). Then, E_{max} can be seen as a parameter related to myocardial contractility, while E_a can be seen as a parameter related to the vascular resistance (SVR) and HR.

---

[8] Burkhoff D. Mechanical Properties of The Heart and its Interaction with the Vascular System. [Accessed Jul 11, 2006]. Available from: http://www.columbia.edu/itc/hs/medical/heartsim/review.pdf

LV volumetric dynamics can be determined by several mechanisms, divisible into two categories that lead to different LV volumetric dynamics: those which act according to the Frank-Starling mechanism and those which do not. We will call the first category Starling-like and the second, according to (Kerkhof, 1981), alternative-Starling-like.

In Starling-like behavior the SV changes following an EDV change, and the ESV is fixed and independent of the EDV. In alternative-Starling-like behavior the ESV changes following an EDV change, and the SV is fixed and independent of the EDV. Clearly, observable situations involve both behaviors. We can express the combined effect as a linear relationship. To identify Starling-like behavior we have:

$$SV = \alpha + \beta \cdot EDV \qquad (4.2)$$

In contrast, if the ESV is used, instead of the SV, as the dependent variable, we have the alternative-Starling-like behavior:

$$ESV = \alpha' + \beta' \cdot EDV \qquad (4.3)$$

Equations (4.2) and (4.3) represent the Starling curve and the alternative Starling curve respectively. The latter relationship was first documented and termed the "Alternative-Starling-Curve" in (Kerkhof, 1981). In equation (4.2) the slope β can be seen as the degree to which Starling-like mechanisms are used (Kerkhof et al., 2002). The slope and intercept coefficients of equation (4.3) are related to those of equation (4.2) by simple relationships: $\beta' = 1 - \beta$, $\alpha' = -\alpha$. Thus it suffices to identify either curve to obtain both the Starling-like and the alternative-Starling-like behavior.

Statistical analysis performed

To determine the effect of different working conditions and support level on the LV-PV loop, and diastolic and end systolic volumes were equated to the maximum and minimum LV volumes respectively, as observed in each experimental step. LVVs were indexed (LVVI) by body surface area (BSA) calculated using Mitchell's sheep-specific formula (Berman, 2003); comparison of body surface area calculated with other formulas from (Berman, 2003) gave very similar results. Scatter plots of the SVI as a function of the EDVI, as well as scatter plots of the ESVI as a function of EDVI were generated. Linear regressions were calculated for each sheep, for the pooled data, for each pump support level and in the case where the LV did not eject through the aortic valve but only through the apical cannula. Variations of the EDVI, ESVI, SVI and pulmonary artery flow indexed by body surface area (cardiac output index, COI), depending on pump support level with respect to the clamped graft condition, were assessed by t-tests.

To evaluate the hemodynamic response to preload increase, changes in EDV, ESV, SV, CO, SVR, E_{max}, dP/dt_{max}, CVP, LAP, PAP, AoP, within

the seven sheep, were derived in the clamped-graft condition, at HR=100 bpm (n=6) and HR=130 bpm (n=3), before and after infusion of NaCl solution. SVR was calculated as the difference between mean arterial pressure (MAP) and CVP divided by the CO. E_{max} was calculated from the single averaged beat as *max[LVP(t)/(LVV(t)-V_0)]*, where V_0 was considered to be zero in all experiments. The peak rate of rise of ventricular pressure (dP/dt$_{max}$), was calculated as the maximum of the time derivative of the LVP. It should be noted here that the dP/dt$_{max}$ contractility index does not depend on the LV volume measurement.

Linear regression and Pearson correlation were used to quantify linear relations between SVI and EDVI and between ESVI and EDVI. The statistical significance of the difference between regression slopes and intercepts calculated out of different sheep was assessed by analysis of covariance (ANCOVA). Paired t-tests were used to identify significant differences between pre- and post-infusion variables. Statistical significance was considered to be defined by $p<0.05$. All data are reported as the mean±SD. All statistics were performed using the Matlab$^{®}$ Statistics Toolbox 5.1.

3   Results and Discussion

Results

The decrease of ρ after the saline infusion was 10±5% for the seven sheep. For the calibration of the left ventricular volume measurement, *Vc* was however assumed constant throughout the experiment.

In each sheep of the seven sheep, the Lilliefors test failed to reject the hypothesis that the distribution of the residuals, coming from regression of the end-diastolic PV points, was normal. Moreover, a visual inspection of the normal plot of the residuals confirmed their normal distribution. We thus concluded, in the LV volume range considered, that all the end diastolic points fall on the same linear EDPVR, and we set the intercept with the volume axis, the left ventricular suction volume at 40 ml.

Despite alterations in the shape of the PV loop (Figure 4.6) due to different levels of assistance (from a rectangular shape when the graft was clamped to a bell shape at maximum pump support level), the ESVI and the EDVI showed a significant linear correlation, in each sheep (Table 4.1).

Table 4.1: ESVI vs. EDVI relationships for different animals. *α'* and *β'* represent the constant term and the slope of the ESVI-EDVI relationship, respectively; *n* the number of observations and R^2 the squared correlation coefficient

	Sheep #1	Sheep #2	Sheep #3	Sheep #4	Sheep #5	Sheep #6	Sheep #7
n	18	29	23	23	39	41	27
α'	-22.84	18.73	-47.57	-4.26	-16.02	7.52	-10.01
β'	0.895	0.547	1.347	0.631	0.905	0.666	0.745
R^2	0.587	0.702	0.667	0.869	0.871	0.726	0.841
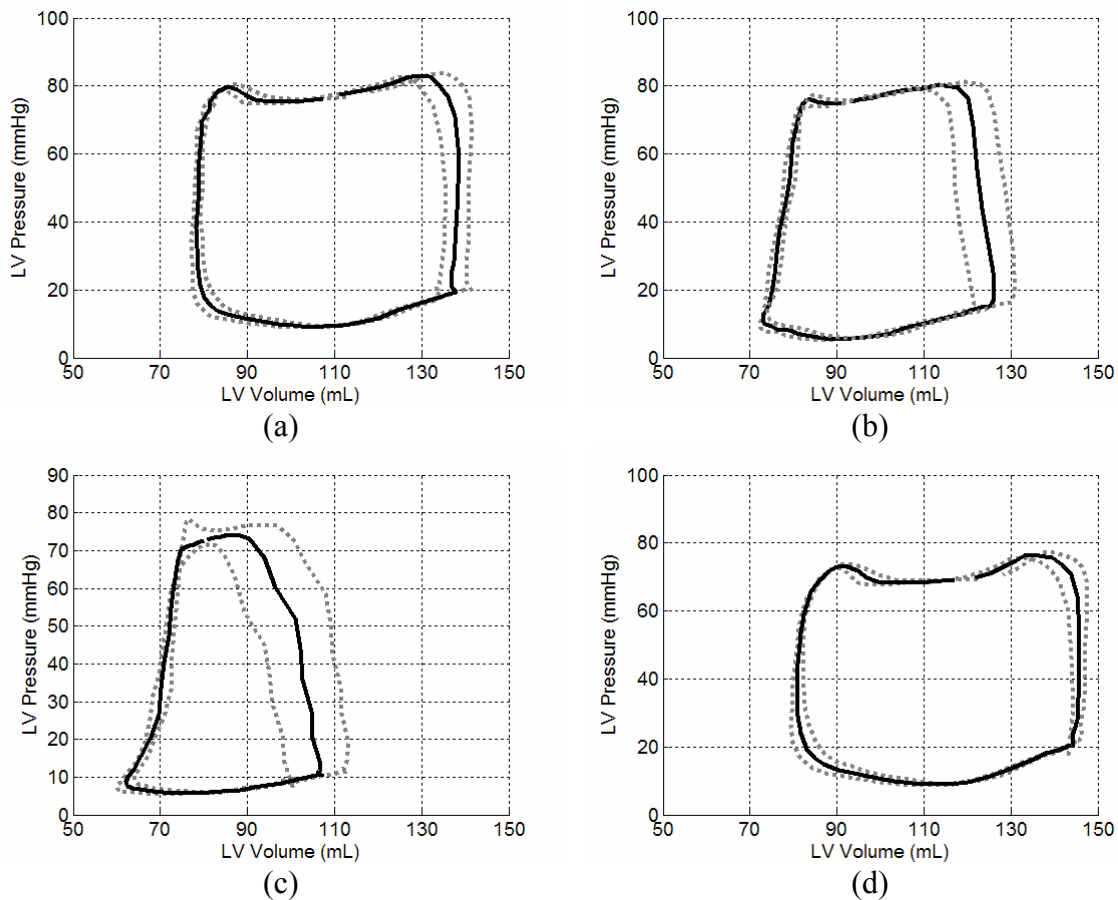
Figure 4.6 – (a) left ventricular pressure volume loops with the graft clamped (like no pump); (b) on minimum pump support; (c) on maximum pump support; (d) in pump off condition (backflow). Solid lines represent the signal averaged PV loops from 30 to 40 steady state beats; dotted lines are ±1 standard deviation.

The average slope was 0.819, whether the average intercept was -10.64. Three sheep (#2, #3, #6) had significantly different slope and intercept of their EDVI-ESVI relationship with respect to that of the other sheep. The difference between regression slopes and intercepts of the remaining four sheep was not significant (p=0.14). The regression for the remaining sheep data, pooled together, was: ESVI=0.734*EDVI-7.94; R^2=0.931, p<0.0001, n=107. If we pool all the sheep together results does not change substantially: ESVI=0.845*EDVI-15.21; R^2=0.924, p<0.0001, n=200 (Figure 4.7a). Therefore in the following analysis all the sheep will be pooled together. EDVI and SVI showed a less strong, but still significant, correlation: SVI=0.155*EDVI+15.21; R^2=0.291, p<0.0001, n=200 (Figure 4.7b).

(a)

(b)
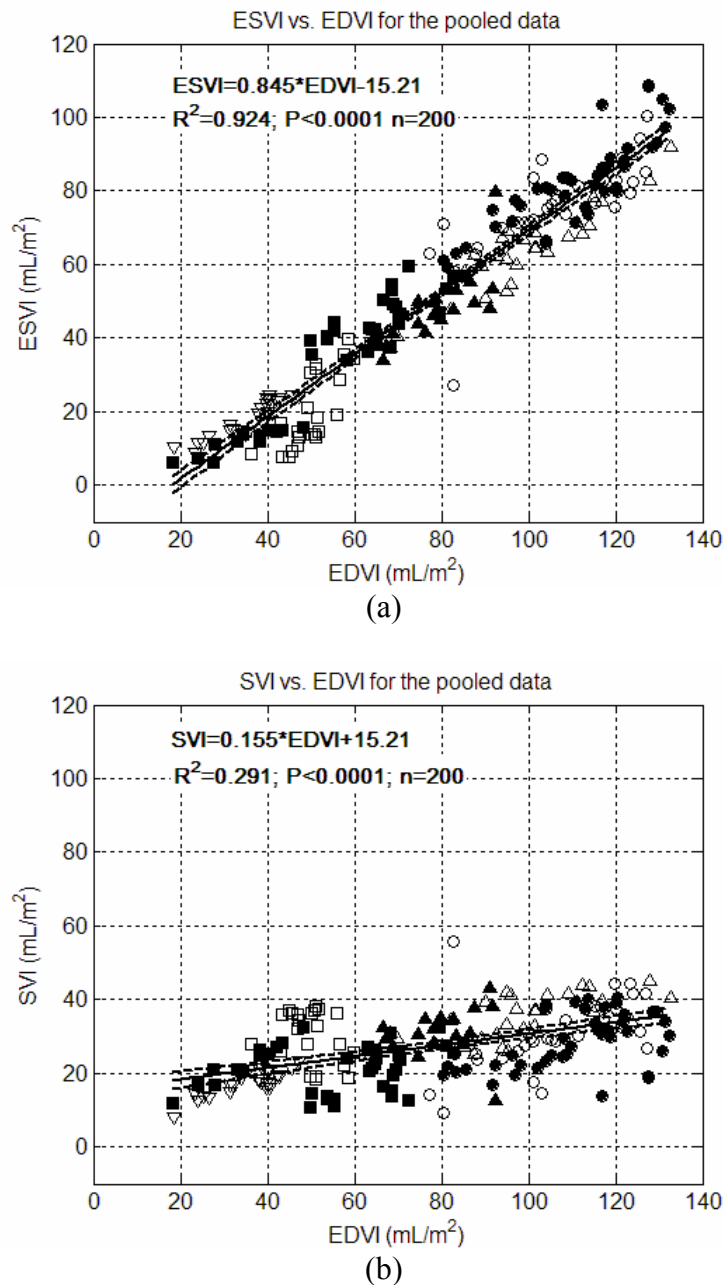
Figure 4.7 – (a) scatter plot of end diastolic volume index (EDVI) vs. end systolic volume index (ESVI) for pooled data; (b) scatter plot of stroke volume index (SVI) vs. end systolic volume index (ESVI) for pooled data. Symbols refer to different sheep. Continuous lines are linear regressions, dashed lines are the 95% confidence intervals for the regression lines.

In 28 out of 200 measurement steps the maximum LVP did not reached the MAP level, thus indicating that the LV did not eject through the aortic valve but only through the apical cannula. The EDVI-ESVI relationship (and therefore the EDVI-SVI relationship) was substantially the same with respect to that obtained when all the measurements were considered together (Figure 4.8).
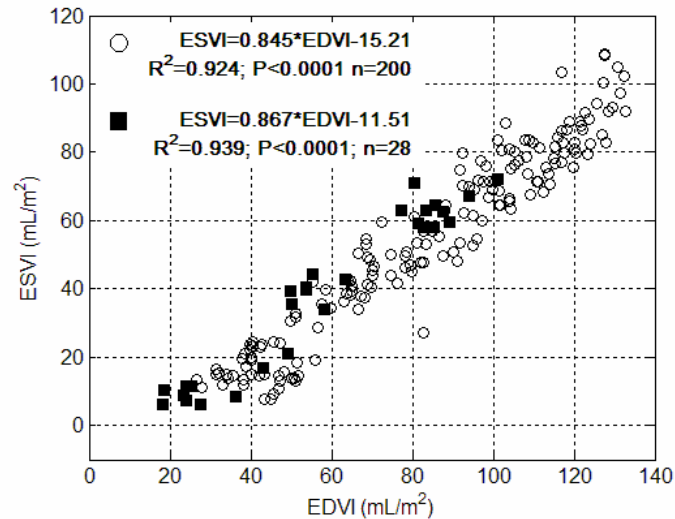
Figure 4.8 – scatter plot of end diastolic volume index (EDVI) vs. end systolic volume index (ESVI) for all the experimental steps (O); the same scatter plot for the experimental steps when maximum left ventricular pressure did not reach the mean arterial pressure, i.e. aortic valve always closed (■).

The EDVI-ESVI relationship was also little affected by the pump support level (Table 4.2), indicating that the ESVI changed in a mandatory fashion with EDVI changes, independent of pump support level. Table 4.2 also shows a significant decrease of SVI and EDVI for the maximum pump support and a significant increase of COI in case of medium pump support level.

In response to a significant increase in EDV due to infusion, in the clamped-graft condition, SVR, E_{max} and dP/dt_{max} decreased significantly; ESV increased significantly and SV and CO increased slightly, but not significantly. CVP, LAP and PAP all increased significantly, whereas AoP decreased, but not significantly (Table 4.3).

Table 4.2: EDVI, ESVI, SVI and COI depending on different pump support levels; statistical significance of variations with respect to the clamped graft condition was assessed for these variables. ESVI vs. EDVI relationship coefficients depending on different pump support levels: α' and β' represent the constant term and the slope of the ESVI-EDVI relationship, respectively; n the number of observations and R^2 the squared correlation coefficient.

	Clamped graft	Min. support	Med. support	Max. support	Backflow
n	43	45	24	45	43
$EDVI$ (mL/m^2)	83.1±33.9	76.5±31.0	87.0±25.3	67.3±27.0*	88.9±33.0
$ESVI$ (mL/m^2)	53.3±28.7	49.5±26.9	58.8±23.8	43.9±22.6	58.8±30.1
SVI (mL/m^2)	29.8±8.7	27.0±8.1	28.2±7.6	23.4±8.5**	30.1±9.0
COI (L/min/m^2)	3.3±1.2	3.5±1.3	4.3±1.1***	3.7±1.3	2.9±1.1
α'	-15.42	-14.86	-19.28	-9.84	-19.15
β'	0.826	0.842	0.897	0.799	0.877
R^2	0.949	0.941	0.909	0.915	0.927

* $p<0.02$; ** $p<0.001$; *** $p<0.002$; with respect to the clamped graft condition

Table 4.3: steady state hemodynamic values for the seven sheep in clamped graft condition, without pharmacological intervention on the left ventricle, before and after increase of preload obtained by infusion; n is the number of paired observations.

	Before infusion	After infusion	Difference	p
n	9	9		
EDV (mL)	142.5±52.9	174.3±50.4	31.8±20.2	0.0015
ESV (mL)	84.2±54.1	112.6±45.2	28.4±22.8	0.0058
SV (mL)	58.2±13.6	61.6±7.5	3.4±13.9	0.4842
CO (L/min)	5.6±1.5	6.1±1.8	0.5±2.4	0.6037
SVR (mmHg*s/mL)	0.63±0.20	0.44±0.11	-0.19±0.15	0.0038
$Emax$ (mmHg/mL)	1.14±0.67	0.70±0.43	-0.44±0.56	0.0453
dP/dt_{max} (mmHg/s)	1354.3±219.1	1067.1±358.6	-287.2±280.9	0.0154
CVP (mmHg)	9.0±2.9	14.4±2.3	5.4±3.0	0.0007
LAP (mmHg)	12.8±1.6	17.2±4.2	4.4±4.5	0.0202
PAP (mmHg)	19.2±2.2	21.8±2.8	2.6±1.6	0.0160
AoP (mmHg)	64.8±8.5	58.1±13.2	-6.7±13.1	0.1637

Discussion

This study demonstrates that despite changes in ventricular preload and afterload, the cardiac output tended to be stable in the acute sheep experiment. The medium pump support level lead, however, to a significant cardiac output index increase, without significant changes in the LV volume. On the contrary when the pump support was maximum SVI and EDVI decreased, but the cardiac output index did not vary significantly. The left ventricular stroke volume and the overall cardiac output are, in the presence of mechanical support, slightly determined by the pump support level. This fact leads to a dominant alternative-Starling behavior. And this, in turn, means that if the target cardiac output, that we judged to be appropriate for the animal, mismatched its actual needed, the autoregulatory mechanism appeared to oppose our LVAD flow driving mode. When we drove the pump at high flow to obtain an elevated cardiac output, the animal reacted with mechanisms that lead to the alternative-Starling characteristics, preserving the overall cardiac output, despite a decrease in EDV and SV.

The continuous cardiac assist in the acute sheep experiment causes the ESVI-EDVI relationship to show a steeper slope and better correlation than the SVI-EDVI relationship. This fact suggests that ESVI tends to follow EDVI, keeping SVI relatively constant, despite changes in the EDVI. The blood flow circulating into the body, normalized by the body surface area, can be seen to be proportional to the SVI at a fixed HR, and only slightly dependent on the EDVI. This almost-fixed flow depends on the level of metabolism in the animals (Guyton et al., 1973, p. 4), which was stable during the acute experiment. For this reason it may not be always appropriate to drive LVADs to force a predetermined systemic flow, especially in the case of a recovering or somewhat healthier left ventricle.

The literature (Beringer and Kerkhof, 1998, Frye and Braunwald, 1960, Kerkhof et al., 2002) suggests better ESV-EDV than SV-EDV correlation in *in-vivo* measurements, both in population and single subject studies, for different animal species, patho-physiological states, and techniques of left ventricular volume measurement. These findings strongly suggest that the alternative-Starling-like autoregulatory mechanisms play an important role in left ventricular volume regulation *in-vivo*, at least for subjects at rest. The same finding was obtained in the present study of left ventricular volume regulation in the presence of an LVAD.

It is known that autoregulatory mechanisms affect both the heart, by chronotropic and inotropic effects, and the vascular system, by vasoconstriction-dilatation and by changes in vascular tone. All of these phenomena can affect LV pumping capabilities (Guyton et al., 1973, pp. 306 to 311Sagawa et al., 1988), and in particular the PV loop. The PV loop is, in fact, continuously determined by the interaction between the ventricle, and its preload and its afterload (Sunagawa et al., 1984), which in turn are determined by autoregulatory mechanisms.

Further evidence of alternative-Starling-like behavior can be found in the hemodynamic response to a preload increase. Increasing the preload in the clamped graft, might have been expected to yield a cardiac output increase, because of the Starling mechanism (in response to a significant left atrial pressure increase). In fact, the cardiac output did not increase significantly, rather, systemic venous resistance and contractile strength of the hearth decreased. These effects maintained, after infusion, the same cardiac output, stroke volume, and aortic pressure, despite significantly higher central venous pressure, left atrial pressure and pulmonary arterial pressure (see Table 4.3). This is what we mean by alternative-Starling behavior. Again the mechanisms that cause the ESV to increase, following an EDV increase, could be attributed to the combined decrease of systemic venous resistance and contractility (E_{max}, dP/dt_{max}), which limits the aortic pressure, and therefore the end-systolic pressure, and pushes the ESV toward a higher value. It seems reasonable that for a highly supported heart, similar actions can occur to countermand the unneeded high flow imposed by the LVAD, and to keep arterial pressure at a constant value.

Certain aspects of the present study should be noted:

The definition of the ESV as the minimum left ventricular volume is not the conventional definition. However in the circumstances of a clamped graft or of minimum to medium support, this volume and the conventional definition do not differ greatly. At maximum support the minimum left ventricular volume, together with the EDV give a better measure of the blood volume that fills the ventricle in one beat (i.e. the stroke volume). If we consider the ESV as the left ventricular volume when the ventricular elastance reaches its maximum and plot the EDVI-ESVI relationship, a

result similar to that previously reported is found: ESVI=0.918*EDVI-7.45; R^2=0.944, p<0.0001, n=200.

The reported values of ventricular volume depend on appropriate calibration of the conductance catheter. Nevertheless, possible inaccuracies in Vc (due to the variation of ρ and Gp throughout the experiment) or of the dimensionless slope factor $1/\alpha$ would affect the ESVI and the EDVI at the same time and would add noise to the LV volume relationships that were seen. These inaccuracies would, however, not be able to strengthen the observed EDVI-ESVI and the SVI-EDVI relationships and therefore have no relevant effect on their slopes.

The decrease of the E_{max} value in Table 4.3 can be reliably assessed if the V_0 value does not change during the experiments. Moreover we considered the E_{max} independent on heart rate for the frequency range used in our experiments (Sagawa et al., 1988, p. 146).

Differences between the clinical setting and these experiments must be borne in mind. Chronic heart disease patients are far different from healthy sheep used in the experiments, where the open-chest setting affects autoregulatory mechanisms, and where part of their reserve has already been used (Guyton et al., 1973, p. 432). Finally the paced heart conditions are not always matched in the clinical situation.

4 Conclusions

The analysis of PV-loops during cardiac assist shows not only the well-known Starling mechanism, but also mechanisms like those reported by others for the unassisted heart as "Alternative-Starling-Mechanism". During cardiac assistance, in acute animal experiments, left ventricular volume analysis demonstrates a strong correlation between ESVI and EDVI attributable to autoregulatory mechanisms. Thus autoregulatory mechanisms should be taken into account in the development of driving strategies for an assist device. For example, one might design a control strategy for the assist device which allows the flow to be completely determined by the organism. The left ventricular assist device would then, according to this concept, be driven to reduce hydraulic afterload impedance for the left ventricle.

*Chapter 5**

Axial flow VAD control strategy to reduce the left ventricle afterload impedance and help perfusion.

The control of a ventricular assist device (VAD) is a complex task where adequate unloading for the heart, perfusion and physiological response to patient's needs are sought. This chapter is concerning with the control of an axial flow VAD in apical connection as a reduced afterload impedance for the left ventricle (LV). A complete mathematical model of the cardiovascular system with implanted a VAD is used to test the control strategy. Simulations quantify the effects of the proposed strategy on a pathological LV. The proposed strategy drives directly neither the VAD speed/flow nor the differential pressure over the VAD, but the amount of the LV afterload impedance reduction. The proposed control strategy makes the VAD a cardiovascular-integrated device, which is able to restore normal patient perfusion and hemodynamics. The cardiac output is determined by the patient, thus assuring a good responsiveness to his needs.

1   Introduction

The control of continuous flow ventricular assist devices (VADs), such as centrifugal or axial blood pumps, represents an important challenge for the use of these devices. The control strategy is important both for their use as bridge to transplantation, and even more for long term use or permanent support. In both cases there is a need to solve complex tasks, such adequate unloading for the heart, adequate perfusion and physiological response to patient's needs. However the interaction with the patient's cardiovascular system and unloading of the heart are quite different compared with the already established pulsatile support systems. In particular continuous flow VADs create ventricle suction when the impeller speed is too high, and thus flow, exceeds the venous return to the left ventricle (Amin et al., 1998, Schima et al., 1990); when the speed is too low there may be a retrograde flow of blood through the rotating impeller during ventricular diastole, from the pressurized aorta into the left ventricle (Nakata et al., 1999); aortic pressure pulsatility is considerably lower than normal (Wieselthaler et al., 2000). In addition, although at present most clinically implanted continuous flow VADs are operated at constant speed and adjusted by the physician until a perceived comfort level of perfusion is achieved, changes in the physiologic patient demand cause a minor adaptation of pump flow (Schima et al., 2006). For such reasons physiologic control algorithms must be developed to automatically adjust the pump flow to the patient needs.

In (Parnis et al., 1997) the pump rotational speed was set as a linear function to the heart rate, which was obtained from the motor current waveform. In (Fu and Xu, 2000) a fuzzy controller was employed to control the VAD flow to track a desired flow rate assumed proportional to heart rate. In (Choi et al., 2001) a fuzzy controller was also used to track a VAD pump flow rate pulsatility. In (Schima et al., 2006) the system attempts to achieve a "desired flow", set by the user or dependent on the patient's own heart rate, while continuously monitoring the pulmonary venous return via the measured pump flow pulsatility and preventing ventricle suction by its detection with a previously trained automatic expert-system (Vollkron et al., 2006). These algorithms have the advantage not to use any implanted biologic sensor, although it should be noted that cardiac output of a healthy subject is not only determined by the heart rate but also by the heart contractility and, even more important, by peripheral circulation (Guyton et al., 1973).

Another approach is used in (Giridharan and Skliar, 2006, Nusser et al., 2005, Waters et al., 1999), where the differential pressure over VAD is controlled: the VAD rotational speed is set to generate a predetermined differential pressure between inlet and outlet VAD sections, roughly speaking between left ventricle and aorta. This is equivalent to set the degree of pressure unloading of the failing left ventricle, given that the

aortic pressure is regulated by native autonomic system. These strategies lead to an adequate adaptation to widely changing cardiac demand and clinical conditions in an autonomous way. However the differential pressure must be measured or alternatively estimated using pump parameters.

Finally, multi-objective control strategies (Gwak et al., 2005) mix both the flow and differential pressure approaches by minimizing appropriate penalty functions.

This study is concerning with the control of an axial flow VAD in apical connection as a reduced afterload impedance for the left ventricle. Neither the flow or the differential pressure are then directly controlled but they are the result of the whole strategy. A similar approach was already successfully applied, on a numerical model study for the control of a pulsatile VAD (Arabia et al., 2005, Colacino et al., 2007). A complete and sophisticated mathematical model of the cardiovascular system with implanted an axial flow VAD is used to test the control strategy. Numerical simulations quantify the effects of the proposed strategy on a pathological left ventricle. Furthermore a cardiac output need increase and a left ventricle recovering scenarios are also simulated in order to study the range of applicability of the proposed control strategy.

2   Materials and methods

Cardiovascular system and VAD models

A numerical model of the cardiovascular system is used for the VAD control design and test. It is modeled as a closed loop hydraulic circuit comprising several subsystems or compartments: left and right ventricles and atria, both modeled according to the variable elastance concept (Sagawa et al., 1988) systemic and pulmonary arterial loads modeled according to (Toy et al., 1985) and venous returns modeled according to (Guyton et al., 1972). Autoregulation feedback loops were also included (Ursino, 1998), they allow the arterial systemic resistance (Ras) and the unstressed volume of the venous systemic compliance (Cvs) regulation. In particular the Ras is the main determinant of the arterial pressure, whether the unstressed volume of the Cvs is manly responsible for the filling pressure of the vascular circuit, that is in turn the main determinant of cardiac output regulation. Each compartment of the model is validated with published literature data. A complete description of the model and its differential equations is reported in chapter 2.

In Figure 5.1 it is shown the complete electric analog of the cardiovascular model used, a schematic axial flow VAD is also included. The axial flow VAD model is derived and validated by an in-vitro identification campaign conducted on a Micromed DeBakey VAD®. A detailed description of the VAD model and how this was identified and

validated is reported in chapter 3. The inlet cannula of the VAD is connected to the left ventricular apex, whether the outflow graft is connected to the aorta.

The cardiovascular model was tuned in its parameters in order to mimic a realistic pathologic scenario where a failing left ventricle is simulated. In particular a systolic left heart failure of the NYHA (New York Heart Association) class III to IV (Zipes et al., 2004, p. 542) was simulated. This is characterized by a patient that has discomfort already during slight physical activity or even at rest. It translates into model parameters which mimic a dilated left ventricle which can develop low maximum isovolumic pressure with respect to the basal physiological value (120 mmHg at ventricular volume of 300 mL, instead of 270 mmHg at 175 mL); increased heart rate (90 bpm instead of 72 bpm), increased left ventricular mass (300 g instead of 175 g); increased filling pressure of the whole vascular circuit (9 mmHg instead of 6.5 mmHg). All this conditions determine a left ventricle with 40% contractility with respect to a physiological one.
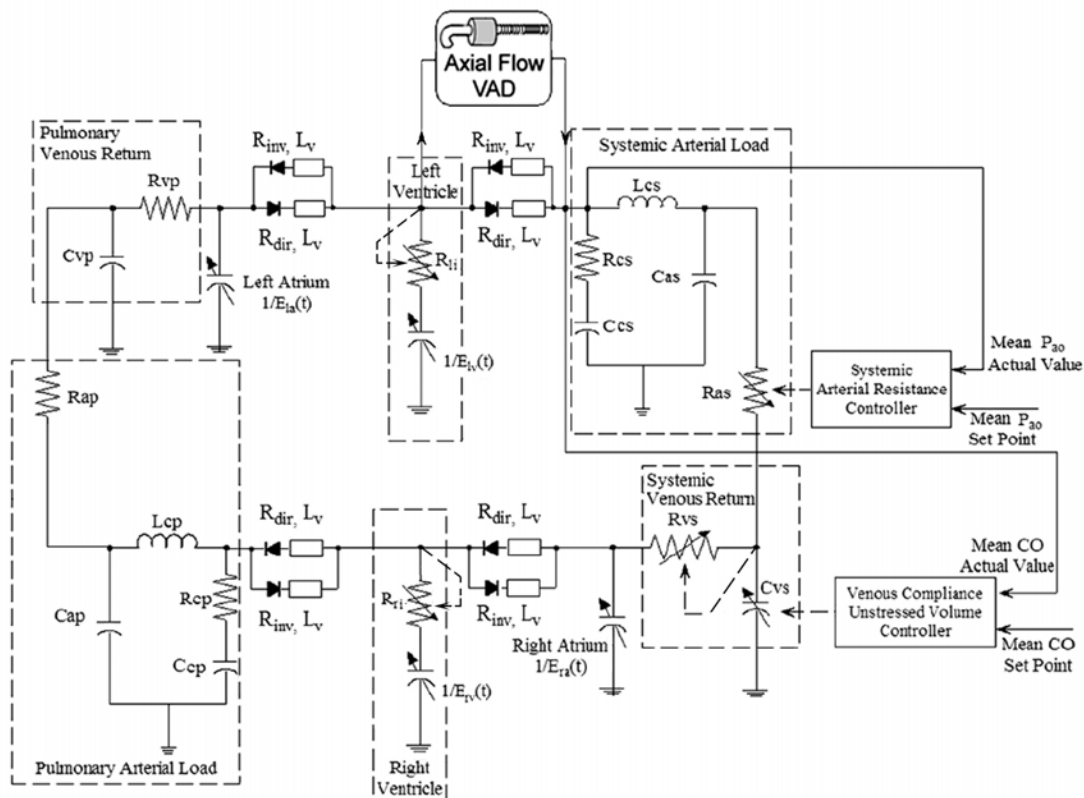

Figure 5.1 – electric analog of the cardiovascular system and its autoregulation feedback loops with schematic axial flow VAD.

VAD control strategy

The aim of the proposed control strategy was to use the VAD unloading action to produce a reduced hydraulic afterload impedance for the pathologic left ventricle. To accomplish this task the proposed strategy,

whose schema is depicted in Figure 5.2, was designed. The strategy rationale is the following: by knowing VAD hydro-dynamical behavior (from previous identification campaign) and by using the measurement of intrinsic pump variables, the VAD flow (*Qvad*) and the VAD rotational speed (*ω*), together with an additional measurement of the aortic pressure (*AoP*), the left ventricular pressure (*LVP*) is estimated. The estimation process is done by using a Extended Kalman Filter (EKF), particularly suited for nonlinear estimations from noise corrupted measurements. The estimated pressure ($L\hat{V}P$) is then used to calculate the reference flow that the VAD should provide in this way: $L\hat{V}P$ is fed into a windkessel mathematical model of the reduced afterload for the left ventricle. Here the calculated flow through the arterial systemic resistance (*Ras**) is the reference flow for the VAD (*Q**). It is clear that the lower is the *Ras** value, the higher will be the unloading action performed by the VAD (i. e. the higher the *Q**). A PI controller allows the flow tracking by regulating the rotational speed (*ω*) of the VAD itself. The mimicked arterial systemic compliance *Cas** is set depending on the value chosen for *Ras** in order to keep the windkessel time constant at a fixed value of 1 sec (Westerhof et al., 1971).
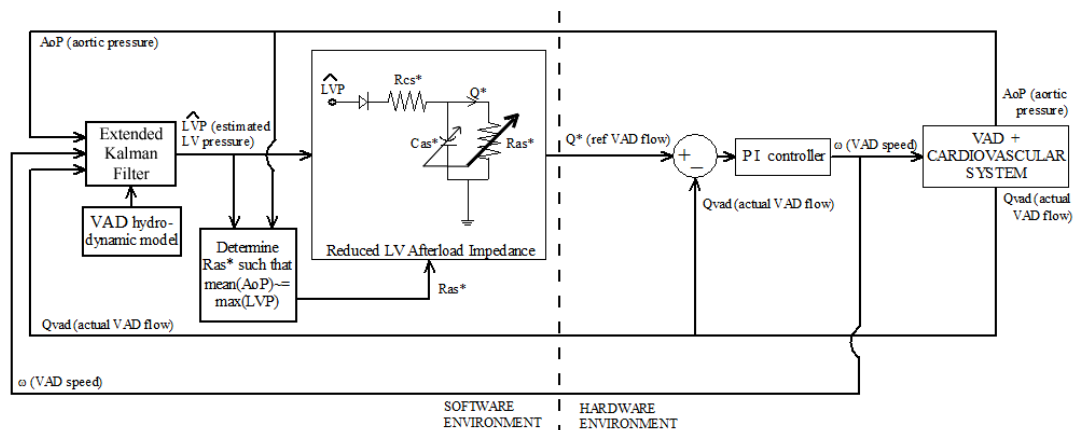
Figure 5.2 - VAD control strategy for ventricular unloading.

The amount of reduction of the afterload impedance (the value of *Ras**) is chosen such that the mean aortic pressure equals circa the maximum left ventricular pressure. In the specific the chosen valued for *Ras** was 0.8 mmHg*sec/mL. Consequently the *Cas** was 1.25 mL/mmHg. The characteristic windkessel resistance *Rcs** was fixed to 0.01 mmHg*sec/mL. The proportional and integral gains for the PI controller were set to 10 and 100 respectively.

The so calculated reference flow for the VAD (*Q**), as a result of the whole control strategy, is the one that the pathologic ventricle would eject toward a reduced hydraulic afterload impedance.

Estimation algorithm

The estimation algorithm used is an Extended Kalman Filter (EKF) (Gelb, 1974, p. 182). It was designed on a simplified model of the VAD, in fact the inflow cannula and outflow graft were not considered for the estimation process. This assumes that the pressure drop across the cannulas is negligible. The state space representation of the VAD was modified and the pressure difference over the pump was considered as an additional state, see equations (5.1). The pressure difference over the pump is actually the state that must be estimated. We than assume that the time variation of this state, actually a input to our system, is partially random in nature (Gelb, 1974, p. 349), this explains the second equation in (5.1).

$$\begin{cases} \dot{x}_1(t) = \dfrac{1}{L} \cdot \left[-\left(a + b \cdot |x_1(t)|\right) \cdot x_1(t) + x_2(t) + \alpha \cdot u_1(t) \right] + w_1(t) \\ \qquad\qquad \dot{x}_2(t) = w_2(t) \\ \qquad\qquad y_1(t) = x_1(t) + v_1(t) \end{cases} \qquad (5.1)$$

Here the first two equations are the state equations, the third is the measurement equation. $x_1(t)$ represents the flow, $x_2(t)$ the pressure difference between VAD inlet and outlet sections, $u_1(t)$ the squared rotational speed of the impeller, L represents a fluid inertance parameter, a and b hydraulic resistance parameters, α a VAD speed related parameter, $y_1(t)$ is the measurement, i.e. the pump flow. The $w_1(t)$, $w_2(t)$ and $v_1(t)$ are process and measurement noise respectively. The process noise vector $[w_1(t),\ w_2(t)]^T$ represents model parameters uncertainty, and it is usually assumed to be a zero mean white Gaussian process with spectral density matrix (Q) which reflects the level of confidence in the estimates of the state variables. This matrix was set to be time-invariant and diagonal, with values equal to [1,1000]. Measurement noise was assumed as a zero mean white Gaussian noise signal with variance related to the accuracy of the VAD flow measurement and set equal to $R=1$ (mL/sec)^2. A detailed description of the EKF theory can be found in chapter 3, paragraph 2.1.

Simulation protocol steps

To test the VAD control algorithm a simulation of 100 sec duration was performed. The simulation was implemented on Matlab®-Simulink® (solver ode23tb). For the first 25 sec the pathologic unassisted ventricle was simulated; at 25th second the VAD was switched on (with Ras*=0.80 mmHg*sec/mL); at 50th second a cardiac output need increase was simulated (25% more with respect to the rest value), representing a situation of slight physical activity; at 75th second the ventricular contractility was increased (form 40% up to 55% contractility with respect to the physiological state), representing a recovery scenario. Simulation protocol steps are summarized in Table 5.1, where at each step was associated a colored number in square brackets.

Table 5.1: simulation protocol steps.

step	**[1]**	**[2]**	**[3]**	**[4]**
description	Unassisted pathologic LV (contractility 40%)	VAD on (Ras*=0.80 mmHg*sec/mL)	CO need increase (25% more w.r.t. rest value)	LV contractility increase (contractility 55%)
time (sec)	0-25	25-50	50-75	75-100

Analysis of the assisted left ventricle pump function was carried out by means of pressure-volume loops. To visualize also the hemodynamic changes for the left ventricle, left ventricular pressure (LVP), left atrial pressure (LAP) and aortic pressure (AoP), together with left ventricular volume (LVV) were continuously acquired and plotted. Mean flows due to the left ventricle through the aortic valve (Q_{LV}) and due to the VAD (Q_{VAD}) itself were calculated along the simulation at each heart cycle. To evaluate the LVP pressure estimation algorithm both the estimated and actual LVP were compared; the PI flow tracking was evaluated plotting together the reference flow (Q^*) and the measured one (Q_{VAD}); the VAD speed ω was also plotted. Before the onset of each new condition, when the previous one has reached the steady state, mean values in the heart cycle of the cardiac output (CO), Q_{LV}, Q_{VAD}, ω, LVV, LAP, AoP and pulmonary arterial pressure (PAP) were calculated. Finally cardiac output curves, depending on atrial pressures, of the unassisted and of the assisted cases were generated.

3 Results

Figure 5.3 shows pressure volume loops in the four studied conditions. The dashed End Systolic Pressure Volume Relationship (ESPVR) represents the increased contractility condition. End Diastolic Pressure Volume Relationship (EDPVR) remains constant in all the cases. The PV loop for the studied cases are denoted by different colors; it is possible to notice that the PV loops for the assisted conditions have a characteristic bell shape (i.e. no isovolumic contraction and relaxation).
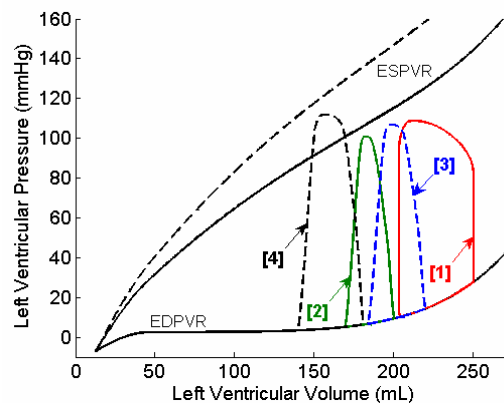

Figure 5.3 – LV pressure volume loops in the four studied conditions, denoted by numbers in square brackets (see Table 5.1).
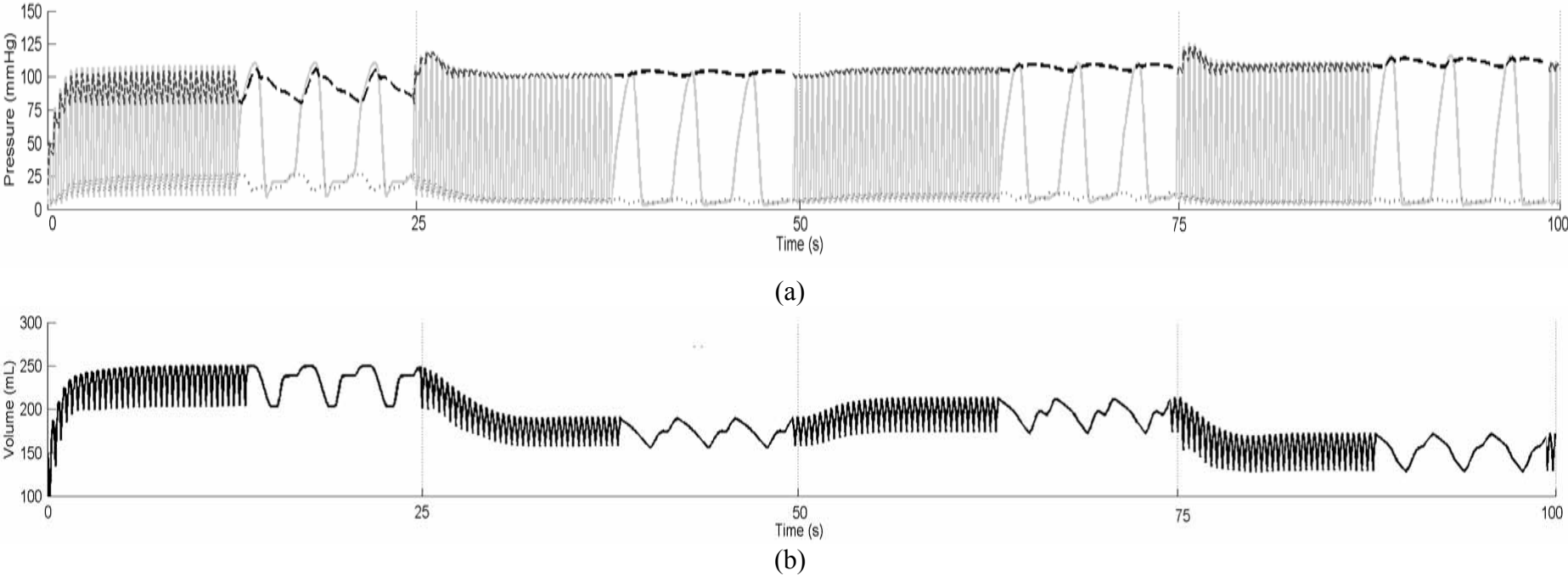
(a)

(b)

Figure 5.4 – (a) left ventricular pressure (solid), aortic pressure (dashed), left atrial pressure (dotted); (b) left ventricular volume.

Figure 5.4 shows the continuously acquired pressures (LVP, LAP and AoP) and LV volume. Each 25 seconds it is possible to notice changes in the signal shapes due to the different simulation protocol steps (see Table 5.1), in particular due to the assistance the LAP decreases as well as the AoP pulse and the LVV.

In Figure 5.5 it is possible to distinguish the VAD and LV flow contribution to the total cardiac output in the four studied conditions. Flow is calculated as the mean in the heart beat of the flow waveform.
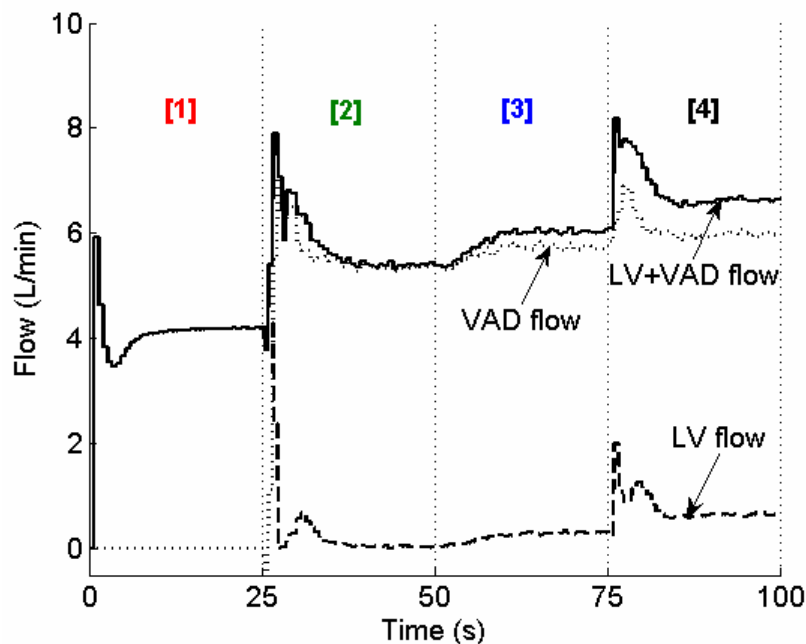

Figure 5.5 – left ventricular (LV) flow through the aortic valve (dashed), VAD flow (dotted), and total LV+VAD flow (solid).

In the upper panel of Figure 5.6 it is plotted the actual left ventricular pressure compared with the one estimated using the extended Kalman filter. The estimated signal is the one that is fed into the mathematical model of the reduced LV afterload. Reference flow for the VAD (dashed curve in middle panel of Figure 5.6) is calculated from the mathematical model of the afterload and tracked by PI control. The speed signal (lower panel of Figure 5.6), result of the PI control, allows the VAD to generate the flow shown as solid line in the middle panel of Figure 5.6.

In Table 5.2 hemodynamics and VAD mean values for each protocol step in the simulation are reported. As the result of the assistance the overall cardiac output and the aortic pressure increase, the left atrial pressure and pulmonary arterial pressure decrease, as well as left ventricular volume. Finally Figure 5.7 shows cardiac output curves and respective venous returns for the unassisted and assisted ventricle (conditions [1] and [2] in Table 5.1). Mean pulmonary and systemic pressures are the intercept of the venous return curves with the x axis. The

y coordinate of the intersection between the cardiac output curve (right or left ventricle) with its respective venous return curve (systemic or pulmonary) represents the cardiac output, whether the x coordinate of this point represents the atrial pressure. The right ventricular cardiac output curve is significantly improved after because of the VAD assistance, the right ventricular one is also improved because of the reduction of the mean pulmonary pressure ($Pmp_{[2]}$) and consequent unloading of the right ventricle.
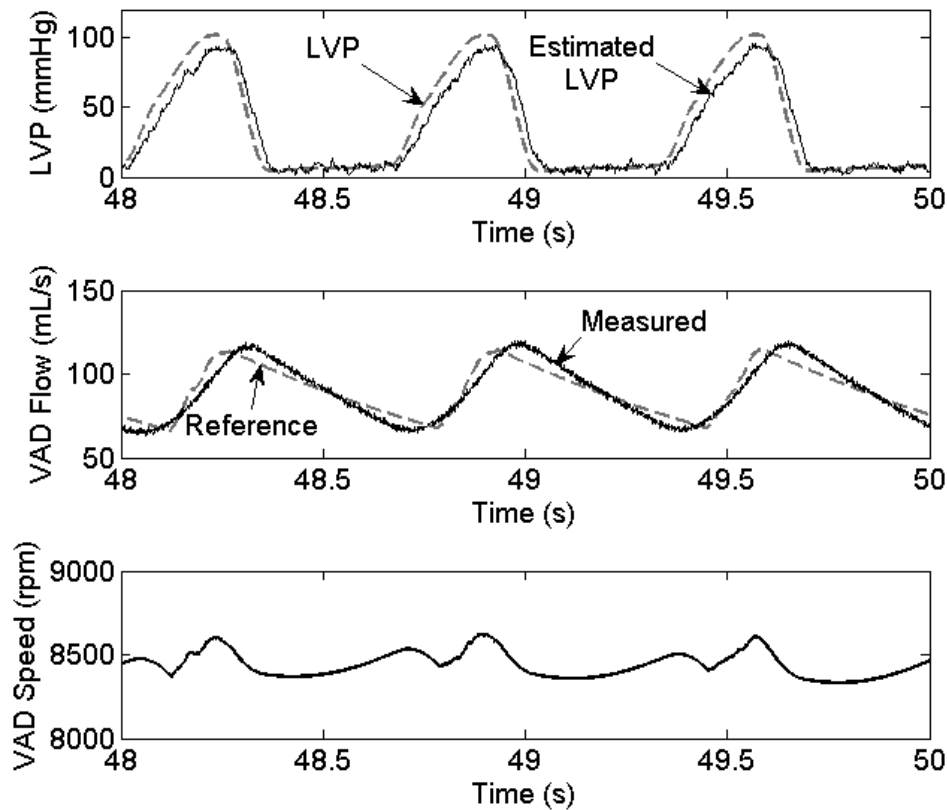
Figure 5.6 – upper panel: actual (dashed) and estimated (solid) left ventricular pressure (LVP); middle panel: reference (dashed) and measured (solid) VAD flow; bottom panel: VAD speed.

Table 5.2: Hemodynamic and VAD mean values in the four studied conditions.

	[1]	[2]	[3]	[4]	Units
CO	4.19	5.41	6.04	6.61	L/min
Q_{LV}	4.19	0.04	0.29	0.65	L/min
Q_{VAD}	-	5.37	5.75	5.96	L/min
ω	-	8471	8392	8717	rpm
LVV	233	186	205	163	mL
LAP	20.8	7.9	11.5	6.0	mmHg
AoP	91.0	100.2	104.1	107.0	mmHg
PAP	29.2	18.7	23.6	19.3	mmHg

CO: cardiac output; Q_{LV}: flow through the aortic valve; Q_{LV}: flow through the VAD; ω: VAD rotational speed; LVV: left ventricular volume; LAP: left atrial pressure; AoP: aortic pressure; PAP: pulmonary arterial pressure.

Figure 5.7 – cardiac output curves and respective venous returns for the unassisted ventricle (red curves), and assisted ventricle (green curves).

4 Discussion

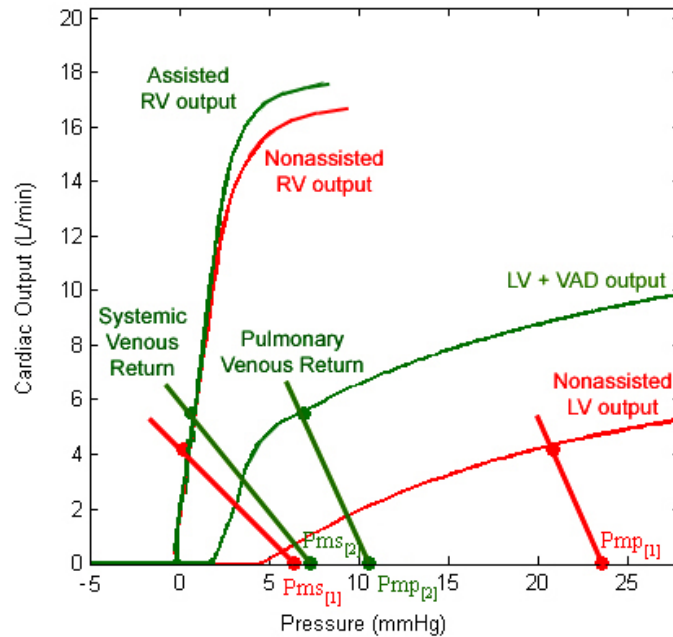Any VAD modifies LV input and output pressures and flow rates. Cardiac mechanics and overall hemodynamics analysis are then particularly useful to understand which LV preload and afterload conditions are necessary to obtain a satisfactory VAD operation mode.

Results show how proper ventricular load impedance control allows improving the heart mechanical operation as well as the cardiac output curve. The left ventricular mechanics improves after assistance because of the shift of the ventricular volumes towards lower values (Figure 5.3, Figure 5.4 and Table 5.2). Better cardiac output curve due to the VAD improve patient perfusion and hemodynamics. In fact, as a result of assistance, a greater cardiac output can be achieved with lower left atrial pressure (Figure 5.7 and Table 5.2). This fact in turn determines an unloading of the pulmonary circulation and of the right heart, being the pulmonary arterial pressure also decreased (Table 5.2). The patient can also easily handle situations where there is a need of cardiac output increase (condition [3] in Table 5.2), due for example to exercise. In fact the improved cardiac output curve permits to the patient increased cardiac output with a still low left atrial pressure (11.5 mmHg) in comparison with the high values in the unassisted situation (condition [1] in Table 5.2, 20.8 mmHg)

The left ventricle can be online monitored by means of the left ventricular pressure estimation (Figure 5.6), whose diastolic value and decrease rate give information on the ventricle during relaxation, whether the systolic peak gives useful indication on the contractile state of the ventricle. An improvement of the contractile strength of the ventricle

(dashed ESPVR in Figure 5.3) can be tracked by the left ventricular pressure estimation, through maximum pressure increase rate and peak pressure. It is clear however that to have complete information on the contractile state of the ventricle the volume signal is also needed. Furthermore it should be noted that being the cannulas excluded from the estimation algorithm, the peak left ventricular pressure will always be underestimated of an amount that corresponds exactly to the pressure drop across the cannulas.

Some other aspects of this study must be considered.

The control strategy is based on the estimation of the left ventricular pressure. In this study this was performed using an Extended Kalman Filter that uses the pump flow, the pump speed and the aortic pressure measurements. An important feature that such estimator must have is that it should have a relative insensitivity to VAD modeling errors, or should be even take into account other effects such as blood haematocrit changes.

Although the pump measurements are usually available, the aortic pressure measurement is not routinely performed. Thus representing a critical point in the whole control strategy. The left ventricular pressure estimation can be, however, performed using other methods. For example we could reconstruct a rough estimation of the left ventricular pressure from the maximum rate of ventricular pressure (dP/dt_{max}). The latter being linearly related to the maximum rate of the pump flow (dQ_{VAD}/dt_{max}) (Naiyanetr et al., 2007).

Conditions when the peripheral resistance varies must be taken into account. To analyze this situation, a simplification can be made ignoring the inertial and the compliant hydraulic loads of the ventricle. The VAD can be represented with the tunable resistance (*Ras**), that is placed in parallel to the peripheral resistance (*Ras*). The *Ras** value should be increased or decreased depending on the peripheral resistance value, such as to have the parallel of the two resistance constant and equal to the load that the ventricle should have. Simply speaking if there is vasodilatation (*Ras* decrease) the VAD contribute to the total cardiac output can be lower (setting *Ras** to a bigger value) because the ventricle can easily eject toward its natural load. The contrary happens if vasoconstriction occurs (*Ras* increase). The VAD contribute should be then bigger, thus setting *Ras** to a lower value.

Being this one a study based on a numerical model of the circulation and VAD, it represents just a first step and a proof-of-concept for the development of a really applicable VAD control strategy. First a in-vitro and than animal study of this control modality are therefore necessary.

5 Conclusion

The proposed control strategy makes the VAD a cardiovascular-integrated device, which is able to restore normal patient perfusion and

hemodynamics. The need to investigate a new control strategy for a VAD originated from the experimental observations of the interaction between cardiovascular system and VAD in the previously presented animal study (chapter 4). Main result is that cardiac output is not always directly and strongly influenced by the VAD, but it is mostly mediated by autoregulatory mechanisms (Moscato et al., 2007b).

Therefore the control strategy drives directly neither the VAD speed nor the VAD flow, but the amount of the pathologic left ventricular afterload impedance reduction. This control modality concept is closer to the one where the pressure head across the pump is imposed. In the presented strategy the VAD mimics a three element Winkdessel arterial load with a single tunable parameter *Ras**, which can be chosen to decide the amount of LV load-reduction. This makes the strategy simple. Finally it is to be noted that the cardiac output remains determined by the patient, assuring good physiological responsiveness to his needs.

The presented strategy can be also useful for retraining and weaning of an assisted pathologic ventricle. This can be accomplished by properly stepwise increasing ventricular afterload impedance (*Ras**), after a first phase of complete unloading has been completed (Entwistle, 2004, Hetzer et al., 1999, Mueller and Wallukat, 2007).

Conclusions

Aim of this work was to investigate the interaction between an axial flow VAD and the assisted cardiovascular system, by means both of mathematical modeling and an acute animal study. This interaction is a crucial aspect in the development of mechanical circulatory support intended for long-term use.

A numerical model of the whole cardiovascular system was implemented and validated using recent published literature data. This model was completed with a hydrodynamic numerical model of an axial flow VAD (MicroMed-DeBakey VAD®). Advanced signal processing techniques were used for the VAD characterization. To built the necessary experimental setup for VAD identification, sophisticated mathematical methods for identification and control of components in a mock circuit were used.

The interaction of the VAD and the cardiovascular system during in-vivo experiments was investigated: statistical methods were applied to analyze left ventricular pressure volume loop during MicroMed-DeBakey VAD® assistance in an acute animal study. Results form this study showed that autoregulatory mechanisms play an important role in cardiac output regulation. This result brings new and original insight in the interaction between the cardiovascular system and an axial flow VAD.

Therefore a new VAD control strategy, which accounts for these phenomena, was designed and tested on a numerical basis, using the previously derived cardiovascular and VAD models. The main point in this strategy were that neither pressure head or flow across the VAD are controlled, but the LV afterload impedance seen by the failing ventricle ejecting through the VAD. The pump is controlled as to represent a hydraulic afterload impedance for the ejecting ventricle. That makes the device a cardiovascular system-integrated component.

The interaction between the so controlled VAD and the assisted cardiovascular system was evaluated on the mathematical model and it showed that a more physiological VAD control, like to one proposed in this work, restores normal patient perfusion and hemodynamics and, probably more important, can help ventricular recovery.

There is, of course, need of further studies and investigations. Especially regarding the VAD control strategy: it must be first tested on mock-loops (in-vitro) and than animal trials must be performed to validate it. Unfortunately available test benches for cardiac assist devices do not allow to investigate the interaction of devices with the heart and circulation. It is therefore important, for the whole cardiac assist development, to provide R&D departments and Universities with such innovative test benches. This would lead even to better animal trials, designed for an already advanced step in the development of mechanical cardiac assist devices.

References

Ackermann JE. 1972. Der Entwurf Linearer Regelungssysteme in Zustandstraum. Regelungstechnik und Prozessdatenverarbeitung 7:297-300.

Allen G, Murray K, Olsen D. 1997. The importance of pulsatile and nonpulsatile flow in the design of blood pumps. Artif Organs 21(8):922-928.

Amin DV, Antaki JF, Litwak P, Thomas D, Wu ZJ, Watach M. 1998. Induction of ventricular collapse by an axial flow blood pump. ASAIO J 44(5):M685-690.

Arabia M, Akutsu T. 1984. A New Test Circulatory System for Research in Cadiovascular Engineering. Ann Biomed Eng 12(1):29-48.

Arabia M, Cavallari G, Paleani-Vettori PG. 1966. Considerations on the use of models in bio-engineering. Riv Med Aeronaut Spaz 29(3):442-458.

Arabia M, Colacino FM, Moscato F, Piedimonte F. 2005. Left Ventricle Load Impedance Control By Apical VAD Can Help Heart Recovery And Patient Perfusion. Int J Artif Organs 28(9):900.

Arts T, Bovendeerd PH, Prinzen FW, Reneman RS. 1991. Relation between left ventricular cavity pressure and volume and systolic fiber stress and strain in the wall. Biophys J 59(1):93-102.

Avanzolini G, Barbini P, Cappello A, Cevenini G, Pohl V, Sikora T. 1980. Tracking time-varying properties of the systemic vascular bed. IEEE Trans Biomed Eng 36(3):373-381.

Ayre PJ, Lovell NH, Woodard JC. 2003. Non-invasive flow estimation in an implantable rotary blood pump: a study considering non-pulsatile and pulsatile flows. Physiol Meas 24(1):179-189.

Beranek LL. 1996. Acoustics. Acoustical Society of America. 491 p.

Beringer JY, Kerkhof PLM. 1998. A Unifying Representation of Ventricular Volumetric Indexes. IEEE Trans Biomed Eng 45(3):365-371.

Berman A. 2003. Effects of body surface area estimates on predicted energy requirements and heat stress. J Dairy Sci 86(11):3605-3610.

Bertram CD. 2005. Measurement for implantable rotary blood pumps. Physiol Meas 26(4):R99-117.

Beyar R, Hausknecht MJ, Halperin HR, Yin FC, Weisfeldt ML. 1987. Interaction between cardiac chambers and thoracic pressure in intact circulation. Am J Physiol 253(5):H1240-1252.

Buckley NM, Ogden E, Linton DSJ. 1955. The effects of work load ad heart rate on filling of the isolated right ventricle of the dog heart. Circ Res 3(5):434-446.

Burkhoff D, Sugiura S, Yue DT, Sagawa K. 1987. Contractility-dependent curvininearity of end-systolic pressure-volume relations. Am J Physiol 252(6 Pt 2):H1218-1227.

Campbell KB, Ringo J, Wakao Y, klavano PA, Alexander JE. 1982a. Internal capacitance and resistance allow prediction of right ventricle outflow. Am J Physiol 243(1):H99-112.

Campbell KB, Zeglen M, Kagehiro T, Rigas H. 1982b. A pulsatile cardiovascular computer model for teaching heart-blood vessel interaction. Physiologist 25(3):155-162.

Chen J, DeRose J, Slater J, Spanier T, Dewey T, Catanese K, Flannery M, Oz M. 1999. Improved survival rates support left ventricular assist device implantation early after myocardial infarction. J Am Coll Cardiol 33(7):1903-1908.

Choi S. 1998. Modeling and control of left ventricular assist system [Doctoral thesis]: University of Pittsburgh.

Choi S, Antaki JF, Boston JR, Thomas D. 2001. A Sensorless Approach to Control of A Turbodynamic Left Ventricular Assist System. IEEE Trans on Contr Sys Tech 9(3):473-482.

Colacino FM, Moscato F, Piedimonte F, Arabia M, Danieli GA. 2007. Left Ventricle Load Impedance Control by Apical VAD Can Help Heart Recovery and Patient Perfusion: A Numerical Study. ASAIO J 53(3):263-277.

Copeland J, Smith R, Arabia F, Nolan P, Banchy M. 2000. The CardioWest™ temporary Total Artificial Heart as a bridge to transplantation. Semin Thorac Cardiovasc Surg 12(3):238-242.

Darovic GO. 1995. Hemodynamic Monitoring: Invasive and Noninvasive Clinical Application. 2nd ed. Philadelphia: W. B. Saunders Company.

Delgado DH, Rao V, Ross HJ, Verma S, Smedira NG. 2002. Mechanical Circulatory Assistance: State of Art. Circulation 106(16):2046-2050.

Entwistle JW. 2004. Short and long-term mechanical ventricular assistance towards myocardial recovery. Surg Clin North Am 84(1):201-221.

Fetics B, Nevo E, Chen CH, Kaas DA. 1999. Parametric model derivation of transfer function for noninvasive estimation of aortic pressure by radial tonometry. IEEE Trans Biomed Eng 46(6):695-706.

Frank O. 1899. Die grundform des arteriellen pulses. Erste abhandung. Mathematische analyse. Ztsch Biol 37(483-526).

Franklin GF, Powell JD, Workman M. 1998. Digital Control of Dynamic Systems. 3rd ed. Menlo Park: Addison Wesley Longman. 742 p.

Frye RL, Braunwald E. 1960. Studies on Starling's law of the heart. I. The circulatory response to acute hypervolemia and its modification by ganglionic blockade. J Clin Invest 39(7):1043-1050.

Fu M, Xu L. 2000. Computer Simulation of Sensorless Fuzzy Control of A Rotary Blood Pump to Assure Normal Physiology. ASAIO J 46(3):273-278.

Gelb A. 1974. Applied Optimal Estimation. Cambridge, MA: The M.I.T. Press. p. 374 p.

Giridharan GA, Skliar M. 2006. Physiological control of blood pumps using intrinsic pump parameters: a computer simulation study. Artif Organs 30(4):301-307.

Giridharan GA, Skliar M, Olsen DB, Pantalos GM. 2002. Modeling and Control of a Brushless DC Axial Flow Ventricular Assist Device. ASAIO J 48(3):272-289.

Goldstein DJ. 2003 Sep. Worldwide Experience With the MicroMed DeBakey Ventricular Assist Device® as a Bridge to Transplantation. Circulation 108(Suppl 1):II272-277.

Grodins FS. 1959. Integrative cardiovascular physiology: A mathematical systhesis of cardiac and blood vessel hemodynamics. Q Rev Biol 34(2):93-116.

Guyton AC, Coleman TG, Granger HJ. 1972. Circulation: overall regulation. Annu Rev Physiol 34:13-46.

Guyton AC, Hall JE. 2000. Textbook of Medical Physiology. 10th ed: Saunders. 1064 p.

Guyton AC, Jones CE, Coleman TG. 1963. Circulatory Physiology: Cardiac Output and its Regulation. W.B. Saunders Company. 468 p.

Guyton AC, Jones CE, Coleman TG. 1973. Circulatory Physiology: Cardiac Output and its Regulation. 2nd ed: W.B. Saunders Company. 556 p.

Guyton AC, Lindsey AW, Kaufmann BN. 1955. Effect of Mean Circulatory Filling Pressure and Other Peripheral Circulatory Factors on Cardiac Output. Am J Physiol 180(3):463-468.

Gwak KW, Ricci M, Snyder S, Paden BE, Boston JR, Simaan MA, Antaki JF. 2005. In vitro evaluation of multiobjective hemodynamic control of a heart-assist pump. ASAIO J 51(4):329-335.

Helman D, Morales D, Edwards N, Mancini D, Chen J, Rose E, Oz M. 1999. Left ventricular assist device bridge-to-transplant network improves survival after failed cardiotomy. Ann Thorac Surg 68(4):1187-1194.

Hetzer R, Mueller J, Weng Y, Wallukat G, Spiegelsberger S, Loebe M. 1999. Cardiac recovery in dilated cardiomyopathy by unloading with a left ventricular assist device. Ann Thorac Surg 68(2):742-749.

Hill AV. 1922. The mechanism of muscular contraction. Physiol Rev 2(2):310-341.

Hunt H, Baker D, Chin M, Cinquegrani M, Feldmanmd A, Francis G, Ganiats T, Goldstein S, Gregoratos G, Jessup M, Noble R, Packer M, Silver M, Stevenson L, Gibbons R, Antman E, Alpert J, Faxon D, Fuster V, Jacobs A, Hiratzka L, Russell R, Smith SJ. 2001. ACC/AHA Guidelines for the Evaluation and Management of Chronic Heart

Failure in the Adult: Executive Summary. Circulation 104(24):2996-3007.

Karnopp D. 1985. Computer simulation of stick-slip friction in mechanical dynamic systems. ASME J Dyn Sys Meas Control 107(1):100-103.

Kerkhof PLM. 1981. End-systolic volume and the evaluation of cardiac pump function: studien in animals and man [Ph.D. Thesis]: Leiden University.

Kerkhof PLM, Li JK-J, Kresh JY. 2002. An Analytical Expression for the Regulation of Ventricular Volume in the Normal and Diseased Heart. Cardiovasc Eng 2(2):37-48.

Kikugawa D. 2000. Evaluation of cardiac function during left ventricular assist by a centrifugal blood pump. Artif Organs 24(8):632-635.

Kippel W. 2006. Tutorial: Loudspreaker Nonlinearities-Causes, Parameters, Symptoms. J Audio Eng Soc 54(10):907-939.

Klotz S, Hay I, Dickstein ML, Yi GH, Wang J, Maurer MS, Kaas DA, Burkhoff D. 2006. Single-beat estimation of end-diastolic pressure-volume relationship: a novel method with potential for noninvasive application. Am J Physiol Heart Circ Physiol 291(1):H403-412.

Lagarias JC, Reeds JA, Wright MH, Wright PE. 1998. Convergence Properties of the Nelder-Mead Simplex Method in Low Dimensions. SIAM Journal of Optimization 9(1):112-147.

Levick JR. 1995. An Introduction to Cardiovascular Physiology. 2nd ed. Oxford: Butterworth-Heinemann.

Liang F, Taniguchi H, Liu H. 2007. A multi-scale computational method applied to the quantitative evaluation of the left ventricular function. Comput Biol Med 37(5):700-715.

Lietz K, Long JW, Kfoury AG, Slaughter MS, Silver MA, Milano CA, Rogers JG, Naka Y, Mancini D, Miller LW. 2007. Outcomes of Left Ventricular Assist Device Implantation as Destination Therapy in the Post-REMATCH Era: Implications for Patient Selection. Circulation 116(5):497-505.

Ljung L. 1998. System Identification: Theory for the User. 2nd ed: Prentice Hall PTR. 609 p.

Marble AE, Mark Mc. Intyre C, Hastings-James R, Hor CW. 1981. A Comparison of Digital Algorithms Used in Computing the Derivative of Left Ventricular Pressure. IEEE Trans Biomed Eng 28(7):524-529.

Marmarelis VZ. 2004. Nonlinear Dynamic Modeling of Physiological Systems. Akay M, editor. John Wiley & Sons, Inc. 541 p.

Maughan L, Shoukas A, Sagawa K, Weisfeldt M. 1979. Istantaneous pressure-volume relationship of the canine rigth ventricle. Circ Res 44(3):309-315.

Maughan WL, Sunagawa K, Sagawa K. 1987. Ventricular systolic interdependence: volume elastance model in isolated canine hearts. Am J Physiol 253(6 Pt 2):H1381-1390.

Mihaylov D, Verkerke G, G R. 2000. Mechanical cirulatory support system: A Review. Technol Healt Care 8(5):251-266.

Milnor WR. 1989. Hemodynamics. 2nd ed: Williams & Wilkins. 419 p.

Milnor WR. 1990. Cardiovascular Physiology. New York, Oxford: Oxford University Press. 501 p.

Moscato F, Colacino FM, Vollkron M, Schima H, Arabia M, Danieli GA. 2007a. Axial Flow Control Strategy To Reduce The Left Ventricle Afterload Impedance And Help Perfusion. Int J Artif Organs 30(8):734.

Moscato F, Vollkron M, Bergmeister H, Wieselthaler G, Leonard E, Schima H. 2007b. Left ventricular pressure-volume loop analysis during continuous cardiac assist in acute animal trials. Artif Organs 31(5):369-376.

Moscato F, Vollkron M, Huber L, Danieli GA, Schima H. 2006. Cardiovascular Linear Modeling And Identification From Noisy Measurements: A Systematic Approach. Int J Artif Organs 29(5):526.

Mueller J, Wallukat G. 2007. Patients who Have Dilated Cardiomyopathy Must Have a Trial of Bridge to recovery (Pro). Heart Fail Clin 3(3):299-315.

Mueller J, Wallukat G, Weng Y, Dandel M, Ellinghaus P, Huetter J, Hetzer R. 2002. Predictive factors for weaning from a cardiac assist device. An analysis of clinical, gene expression, and protein data. J Heart Lung Transplant 20(2):202.

Naiyanetr P, Vollkron M, Zimpfer D, Sandner S, Wieselthaler G, Schima H. 2007. Assessment of cardiac function for MicroMed-DeBakey VAD recipients. Int J Artif Organs 30(8):735.

Nakata K, Ohtsuka G, Yoshizawa M, Takano T, Glueck J, Fujisawa A, Makinouchi K, Nosé Y. 1999. A new control method that estimates the backflow in a centrifugal pump. Artif Organs 23(6):538-541.

Neubacher A. 1999. Regelung eines Herzsimulators zur Evaluierung von herzunterstützenden Systemen [Master Thesis]. Vienna: Technischen Universität Wien.

Nichols WW, Conti CR, Walker WE, Milnor WR. 1977. Input impedance of the systemic circulation in man. Circ Res 40(5):451-458.

Nikolic S, Yellin EL, Tamura K, Vetter H, Tamura T, Meister JS, Frater RW. 1988. Passive properties of canine left ventricle: diastolic stiffness and restoring forces. Circ Res 62(6):1210-1222.

Normal J, Cooley D, Igo S, Hibbs C, Johnson M, Bennett J, Fuqua J, Trono R, Edmonds C. 1977. Prognostic indices for survival during postcardiotomy intra-aortic balloon pumping. Methods of scoring and classification, with implications for left ventricular assist device utilization. J Thorac Cardiovasc Surg 74(5):709-720.

Nusser P, Muller J, Deus F, Gottel P, Hoffmann J, Graichen K, Arndt A, Merkel T; US2005019167, assignee. 2005. Method and controlling an

assist pump for fluid delivery systems with pulsatile pressure. United States.

O'Rourke MF, Taylor MG. 1967. Input impedance of the systemic circulation. Circ Res 20(4):365-380.

Parnis SM, Conger JL, Fuqua JMJ, Jarvik RK, Inman RW, Tamez D, Macris MP, Moore S, Jacobs G, Sweeney MJ, Frazier OH. 1997. Progress in The Development of A Transcutaneously Powered Axial Flow Blood Pump. ASAIO J 43(5):M576-580.

Pintelton R, Guillarme P, Rolain Y, Schoukens J, Van hamme H. 1994. Parametric Identification of Transfer Functions in the Frequency Domain-A Survey. IEEE Trans Automat Contr 39(11):2245-2260.

Rose EA, Gelijns AC, Moskowitz AJ, Heitjan DF, Stevenson LW, Dembitsky W, Long JW, Ascheim DD, Tierney AR, Levitan RG, Watson JT, Ronan NS, Shapiro PA, Lazar RM, Miller LW, Gupta L, Frazier OH, Desvigne-Nickens P, Oz MC, Poirier VL, Meier P. 2001. Long-Term Use of a Left Ventricular Assist Device for End-Stage Heart Failure. N Eng J Med 345(20):1435-1443.

Sagawa K, Lie RK, Schaefer J. 1990. Translation of Otto Frank's paper "Die Grundform des Arteriellen Pulses" Zeitschrift für Biologie 37: 483-526 (1899). J Mol Cell Cardiol 22(3):253-277.

Sagawa K, Maughan L, Suga H, Sunagawa K. 1988. Cardiac Contraction and the Pressure-Volume Relationship. New York, Oxford: Oxford University Press. 480 p.

Sagawa K, Suga H, Shoukas AA, Bakalar KM. 1977. End-systolic pressure/volume ratio: a new index of contractility. Am J Cardiol 40(5):748-753.

Santamore WR, Burkhoff D. 1991. Hemodynamic consequences of ventricular interaction as assessed by model analysis. Am J Physiol 260((1 Pt 2)):H146-157.

Sarnoff SJ, Braunwald E, Welch GJ, Case R, Stainsby W, Macruz R. 1958. Hemodynamic determinants of oxigen consumption of the heart with special reference to tension-time index. Am J Physiol 192(1):148-156.

Sarnoff SJ, Mitchell JH, Gilmore JP, Remensnyder JP. 1960. Homeometric Autoregulation in the Heart. Circ Res 8(5):1077-1091.

Schima H, Honigschnabel J, Trubel W, Thoma H. 1990. Computer simulation of the circulatory system during support with a rotary blood pump. ASAIO Trans 36(3):M252-254.

Schima H, Trubel W, Moritz A, Wieselthaler G, Stöhr HG, Thoma H, Losert U, Wolner E. 1992. Noninvasive Monitoring of Rotary Blood Pumps: Necessity, Possibilities, and Limitations. Artif Organs 16(2):195-202.

Schima H, Vollkron M, Boehm H, Rothy W, Haisjackl M, Wieselthaler G. 2004. Weaning of rotary blood pump recipients after myocardial

recovery: a computer study of changes in cardiac energetics. J Thorac Cardiovasc Surg 127(6):1743-1750.

Schima H, Vollkron M, Jantsch U, Crevenna R, Roethy W, Benkowski R, Morello G, Quittan M, Hiesmayr M, Wieselthaler G. 2006. First clinical experience with an automatic control system for rotary blood pumps during ergometry and right-heart catheterization. J Heart Lung Transplant 25(2):167-173.

Senzaki H, Chen CH, Kaas DA. 1996. Single-beat estimation of end-systolic pressure-volume relation in humans. A new method with the potential for noninvasive application. Circulation 94(10):2497-2506.

Shim EB, Leem CH, Abe Y, Noma A. 2006. A new multi-scale simulation model of the circulation: from cells to system. Philos Transact A Math Phys Eng Sci 364(1843):1483-1500.

Song X, Throckmorton AL, Untariou A, Patel S, Allaire PE, Wood HG, Olsen DB. 2003. Axial Flow Blood Pumps. ASAIO J 49(4):355-364.

Stepanoff AJ. 1957. Centrifugal and Axial Flow Pumps - Theory, design and application. 2nd ed. New York, London, Sydney: John Wiley & Sons, Inc. 461 p.

Stevenson LW, Kormos RL, Barr ML, Costanzo MR, Desvigne-Nickens P, Feldman AM, Friedman L, Hill JD, Konstam MA, McCarthy PM, Michler RE, Oz MC, Rosengard BR, Sapirstein W, Shanker R, Smith CR, Starling RC, Taylor DO, Wichman A. 2001. Mechanical Cardiac Support 2000: Current Applications and Future Trial Design. Circulation 103(2):337-342.

Suga H. 1969. Time course of the left ventricular pressure-volume relationship under various end-diastolic volumes. Jpn Heart J 10(6):509-515.

Suga H. 1990. Ventricular Energetics. Physiol Rev 70(2):247-277.

Suga H, Sagawa K, Demer L. 1980. Determinants of instantaneous pressure in canine left ventricle: time and volume specification. Circ Res 46(2):256-263.

Suga H, Sagawa K, Shoukas A. 1973. Load indipendence of the istantanueous pressure-volume ratio of the canine left entricle and effects of epinephrine and heart rate on the ratio. Circ Res 32(3):314-322.

Suga H, Yasumura Y, Nozawa T, Futaki S, Tanaka N. 1988. Pressure-volume relation around zero transmural pressure in excised cross-circulated dog left ventricle. Circ Res 63(2):361-372.

Sun Y, Beshara M, Lucariello RJ, Chiaramida SA. 1997. A comprehensive model for right-left heart interaction under the influence of pericardium and baroreflex. Am J Physiol 272(3 Pt 2):H1499-1515.

Sun Y, Siöberg BJ, Ask P, Loyd D, Wranne B. 1995. Mathematical model that characterizes transmitral and pulmonary venous flow velocity patterns. Am J Physiol Heart Circ Physiol 268(1):H476-H489.

Sunagawa K, Sagawa K. 1982. Models of ventricular contraction based on time-varying elastance. Crit Rev Biomed Eng 7(3):193-228.

Sunagawa K, Sagawa K, Maughan L. 1984. Ventricular interaction with the loading system. Ann Biomed Eng 12(2):163-189.

Tanaka A, Yoshizawa M, Abe K, Takeda H, Yambe T, Nitta S. 2003. In Vivo Test of Pressure Head and Flow Rate Estimation in Continuous-Flow Artificial Heart. Artif Organs 27(1):99-103.

Taylor MG. 1959. An experimental determination of the propagation of fluid oscillation in a tube with visco-elastic wall; together woth an analysis of the characteristics required in an electric analogue. Phys Med Biol 4:63-82.

Toy SM, Melbin J, Noordergraaf A. 1985. Reduced models of arterial systems. IEEE Trans Biomed Eng 32(2):174-176.

Ursino M. 1998. Interaction between carotid baroregulation and the pulsating heart: a mathematical model. Am J Physiol 275(5 Pt 2):H1733-1747.

Ursino M, Fiorenzi A, Belardinelli E. 1996. The role of pressure pulsatility in the carotid baroreflex control: a computer simulation study. Comput Biol Med 26(4):297-314.

Ursino M, Magosso E. 2002. Role of short-term cardiovascular regulation in heart period variability: a modeling study. Am J Physiol Heart Circ Physiol 284(4):H1479-1493.

Vandenberghe S. 2004. Modeling the Interaction between Cardiac Assist Devices and the Left Ventricle [Doctoral Thesis]: Ghent University.

Vollkron M. 2004. Development of an Automatic Speed Adaption System for Continuous Working Left Ventricular Assist Devices [Doctoral Thesis]. Vienna: Technische Universitaet Wien.

Vollkron M, Schima H, Huber L, Benkowski R, Morello G, Wieselthaler G. 2006. Advanced suction detection for an axial flow pump. Artif Organs 30(9):665-670.

Vollkron M, Schima H, Huber L, Wieselthaler G. 2002. Interaction of the cardiovascular system with an implanted rotary assist device: simulation study with a refined computer model. Artif Organs 26(4):349-359.

Wakisaka Y, Okuzono Y, Taenaka Y, Chikanari K, Masuzawa T, Nakatani T, Tatsumi E, Nishimura T, Takewa Y, Ohne T, Takano H. 1997. Noninvasive pump flow estimation of a centrifugal blood pump. Artif Organs 21(7):651-654.

Waters T, Allaire P, Tao G, Adams M, Bearson G, Wei N, Hilton E, Baloh M, Olsen D, Khanwilkar P. 1999. Motor feedback physiological control for a continuous flow ventricular assist device. Artif Organs 23(6):480-486.

Welch P. 1967. The use of fast Fourier transform for the estimation of power spectra: A method based on time averaging over short, modified periodograms. IEEE Trans Audio Electroac 15(2):70-73.

Westerhof N, Elzinga G, Sipkema P. 1971. An artificial arterial system for pumping hearts. J Appl Physiol 31(5):776-781.

Westwick DT, Kearney RE. 2003. Identification of Nonlinear Physiological Systems. Akay M, editor. IEEE Press Wiley-Interscience. 261 p.

Wieselthaler G, Schima H, Hiesmayr M, Pacher R, Laufer G, Noon GP, DeBakey M, Wolner E. 2000. First clinical experience with the DeBakey VAD continuous-axial-flow pump for bridge to transplantation. Circulation 101(4):356-359.

Womerseley JR. 1958. Oscillatory flow in arteries: The reflection of the puls wave at junction and rigid inserts in the arterial system. Phys Med Biol 2:313-323.

Wu Y, Allaire P, Tao G, Olsen D. Modeling, Estimation and Control of Cardiovascular Systems with A Left Ventricular Assist Device; 2005 June 8-10; American Control Conference; Portland, OR, USA.

Yellin E. 1995. The momentum of mass, the momentum of ideas, and diastolic function. Ingels N, Daughters G, Baan J, Covell J, Reneman R, Yin F, editors. Amsterdam: IOS Press.

Yoshizawa M, Abe K, Takeda H, Yambe T, Nitta S. 1997. Classical but effective techniques for estimating cardiovascular dynamics. IEEE Eng in Med Biol Mag 16(5):106-112.

Yu Y-C, Boston JR, Simaan MA, Antaki JF. 1998. Estimation of Systemic Vascular Bed Parameters for Artificial Heart Control. IEEE Trans Automat Contr 43(6):765-778.

Yu Y-C, Boston JR, Simaan MA, Antaki JF. 2001. Minimally invasive estimation of systemic vascular parameters. Ann Biomed Eng 29(7):595-606.

Zipes DP, Libby P, Bonow RO, Braunwald E. 2004. Braunwald's Heart Disease: A Textbook of Cardiovascular Medicine. 7th ed. Philadelphia: Elsevier Saunders. 2183 p.